

PHOTONIC CRYSTAL INTERACTIONS WITH ELECTROLUMINESCENCE  
FROM ZINC SULFIDE THIN FILMS DOPED WITH ERBIUM TRIFLUORIDE

By

EVAN STANLEY LAW

A DISSERTATION PRESENTED TO THE GRADUATE SCHOOL  
OF THE UNIVERSITY OF FLORIDA IN PARTIAL FULFILLMENT  
OF THE REQUIREMENTS FOR THE DEGREE OF  
DOCTOR OF PHILOSOPHY

UNIVERSITY OF FLORIDA

2009

© 2009 Evan Stanley Law

To my family

## ACKNOWLEDGMENTS

I most gratefully owe everything to Jesus Christ, my Lord and Savior, my greatest thought by day or by night. I thank him for creating this beautiful world in which I live and study; for he is faithful, his promises are true and his words are beautiful. “Believe in the Lord Jesus, and you will be saved” – Acts 16:31.

I am very thankful to my Mom and Dad who served me so lovingly and graciously in providing for my every opportunity necessary in order for me to grow into the person I am today. Their love and support continually provides me with encouragement, confidence and great joy.

I acknowledge Dr. Paul Holloway in great thanks for allowing me to learn from him and study under him during my time at the University of Florida. His dedication to his work and students goes far beyond the ordinary and I can not express enough my appreciation to him for all he has done to help me achieve my goals. I am also grateful to Dr. Mark Davidson for his continual help with equipment malfunctions and his guidance in my research.

The conversations and encouragement I received from all of my fellow group members proved invaluable in helping me to overcome research difficulties and to ease the pressures of the graduate student life. I am especially thankful to Ricardo Torres, Jason Rowland, Narada Bradman and David DeVito for their help and friendship. I can not forget to give very special thanks to Ludie Harmon, who takes care of every detail, and Chuck Rowland, who so cheerfully helped me to fix every mechanical problem I encountered.

I am most thankful for Chi Alpha Christian Fellowship at UF and am especially grateful to Steve and Charlene Michaels whose love, support and constant dedication to Chi Alpha served to provide me with such a wonderful place to spend countless Friday nights in worship of the God I love and fellowship among the people I love. I am truly blessed and honored to be able to call so many from this group my friend. With no diminishment to those who go unnamed, I

recognize those whom have especially impacted my life in such wonderful ways; Conroy Smith, Chris Kolnicky, Sebastian Pazmino, Dustin Lang, Patrick Maness, Josh Lower, Jason Pearson, Gail Castaneda, Heather Scharfetter, Debora Dumaine, Jennifer Nguyen, Sarah Myhre and Mercy Londoño.

# TABLE OF CONTENTS

	<u>page</u>
ACKNOWLEDGMENTS.....	4
LIST OF FIGURES .....	9
ABSTRACT.....	12
CHAPTER	
1 INTRODUCTION.....	14
2 LITERATURE REVIEW .....	16
2.1 Electroluminescence.....	16
2.1.1 History.....	16
2.1.2 ACTFEL Device Structure .....	19
2.1.3 ACTFEL Device Physics and Optical Characteristics.....	21
2.2 ACTFEL Material Requirements.....	25
2.2.1 Substrate Materials.....	25
2.2.2 Insulating Materials.....	26
2.2.3 Transparent Conductors .....	29
2.2.4 Phosphor Materials.....	29
2.3 Photonic Crystals .....	34
2.3.1 Maxwell’s Equations in Periodic Media [86].....	35
2.3.2 Photonic Band Gap Modeling .....	39
2.3.3 Off-Axis Propagation .....	41
2.3.4 Simultaneous Inhibition and Redistribution of Light Emission.....	42
2.4 Light Scattering.....	44
2.4.1 Light Reflection.....	44
2.4.2 Rayleigh and Mie Scattering .....	45
2.5 Lithography .....	45
2.5.1 Optical Lithography .....	46
2.5.2 Electron Beam Lithography with a Scanning Electron Microscope.....	47
2.5.3 Electron Beam Lithography.....	49
2.5.4 Nanometer Pattern Generation System.....	51
2.5.5 Etching .....	52
2.6 ACTFELD and Photonic Crystal Characterization.....	54
2.6.1 Optical Characterization .....	54
2.6.2 Electrical Characterization.....	56
3 EXPERIMENTAL .....	60
3.1 Introduction .....	60
3.2 ACTFEL Device Fabrication .....	60
3.2.1 Substrate Materials and Preparation.....	60
3.2.2 Thin Film Deposition by RF Magnetron Sputtering .....	61

3.2.3	Post-Deposition Annealing.....	62
3.2.4	Thin Film Deposition by Electron Beam Evaporation.....	64
3.3	Photonic Crystal Fabrication.....	65
3.3.1	Electron Beam Lithography.....	65
3.3.2	Plasma Sputter Etch .....	67
3.4	Device Characterization .....	68
3.4.1	Structural Characterization .....	68
3.4.2	Compositional Characterization .....	69
3.4.3	Optical Characterization .....	70
4	EFFECTS OF PHOTONIC CRYSTAL STRUCTURE IN ACTFEL DEVICES ON LIGHT SCATTERING AND ANGULAR EMISSIONS .....	73
4.1	Introduction .....	73
4.2	Experimental Procedure .....	75
4.2.1	Substrate.....	75
4.2.2	Phosphor Layer Deposition .....	76
4.2.3	Electron Beam Lithography.....	77
4.2.4	Argon Sputter .....	78
4.2.5	BaTa <sub>2</sub> O <sub>6</sub> Deposition .....	78
4.2.6	Top Opaque Electrode .....	79
4.3	Physical Structure Analysis.....	79
4.4	Theoretical Analysis .....	83
4.5	Optical Analysis.....	85
5	EFFECTS OF PHOTONIC CRYSTAL STRUCTURE IN ACTFELDS ON INFRARED EMISSION .....	89
5.1	Introduction .....	89
5.2	Experimental Procedure .....	89
5.3	Physical Structure Analysis.....	89
5.4	Theoretical Analysis .....	91
5.5	Optical Analysis.....	94
5.6	Discussion .....	97
6	CONCLUSIONS .....	99
6.1	ACTFEL Photonic Crystal Fabrication .....	99
6.2	Photonic Crystal Properties .....	100
6.3	Future Work .....	101
	LIST OF REFERENCES .....	103
	BIOGRAPHICAL SKETCH .....	113

## LIST OF TABLES

<u>Table</u>		<u>page</u>
2-1	History of the development of high-field EL in ZnS [2] .....	18
2-2	Requirements for dielectric layers [2, 52-57].....	27
2-3	Insulators used for ACTFEL devices and their properties [2] .....	28
2-4	Properties of some II-VI ACTFEL host materials [2] .....	30

## LIST OF FIGURES

<u>Figure</u>	<u>page</u>
2-1 Full stack, Half stack and Inverted structure schematics.....	21
2-2 Basic ACTFEL device operational processes [2] .....	22
2-3 Ray tracing diagram of ACTFEL structure .....	23
2-4 Transmission spectrum of Corning 7059 glass [50] .....	26
2-5 Partial energy level diagrams for neodymium, erbium and thulium [79, 80] .....	32
2-6 ZnS:ErF <sub>3</sub> ACTFEL device EL response spectrum.....	34
2-7 Photonic band diagram for a square lattice of high dielectric rods in a low dielectric matrix [87] .....	37
2-8 Photonic band diagram for interconnected veins of high dielectric material in a low dielectric matrix [87].....	38
2-9 Photonic band diagram calculated by MPB. ....	40
2-10 Photonic band gap map for honeycomb structure.....	41
2-11 Cross-sectional schematic of LED structures illustrating confining and extracting modes of light propagation [95]. ....	43
2-12 Diffuse versus specular reflection [98] .....	44
2-13 Electron beam interaction volume showing signals (see text) generated [103]. ....	48
2-14 Simulated electron trajectories in PMMA for an electron beam of 25keV acceleration voltage and a spot size of 100 nm [106] .....	50
2-15 Etch rates of materials with respect to RF power in an ECRRIE plasma etch system [113].....	54
2-16 Typical brightness versus voltage data for an ACTFEL device.....	55
2-17 Trapezoidal voltage waveform diagram used for ACTFEL device operation [46]. ....	56
2-18 Schematic of a Sawyer-Tower bridge circuit [116]. ....	56
2-19 Typical Q-V plot for ACTFEL devices driven above the threshold voltage.....	58
3-1 Schematic of RF magnetron sputter deposition system used to sputter deposit ZnS:ErF <sub>3</sub> thin EL films. ....	63

3-2	Schematic of thermal annealing furnace utilizing lamps as heating elements. ....	63
3-3	Electron beam evaporation system schematic.....	64
3-4	Photonic crystal device fabrication flow chart.....	66
3-5	Film thickness versus spin coating speed for PMMA [107] .....	67
3-6	Veeco Probe tapping tip model RTESP image and schematic [120].....	69
3-7	Optical Bench schematic .....	71
4-1	Energy levels and transitions for erbium in ZnS:ErF <sub>3</sub> ACTFELDs and typical emission spectrum [79, 80, 126]. ....	74
4-2	Process flow overview for ZnS:ErF <sub>3</sub> photonic crystal ACTFEL device fabrication.....	76
4-3	AFM analysis of a PC device .....	80
4-4	Image produced by ImageJ® from the AFM data for spatial analysis. ....	81
4-5	EDS spot scan of ZnS:ErF <sub>3</sub> layer. ....	81
4-6	EDS line scan analysis of patterned ZnS:ErF <sub>3</sub> layer.....	82
4-7	Photonic band gap map for honeycomb structure with dielectric mismatch of 11.4.....	84
4-9	Ocean Optics reflectance measurement setup. ....	85
4-10	Diffuse reflectance spectra for the three device types (PC, RND, NOPC). ....	86
4-11	Optical Bench setup for angle resolved emission. ....	87
4-12	Normalized angle resolved emissions data for PC, RND and NOPC devices with the red lines corresponding to 550 nm emission and the blue lines to 1550 nm emission. ....	88
5-1	AFM images and line profiles for PC and RND devices.....	90
5-2	Photonic band gap map for honeycomb structure with dielectric mismatch of 20.....	92
5-3	Mie calculated scattering for YSZ scattering spheres in a ZnS:ErF <sub>3</sub> matrix for 550 nm and 1550 nm wavelength light [129]. ....	93
5-4	EL measurement on the optical bench.....	95
5-5	Brightness versus time at various voltages plots.....	95
5-6	Percent change in luminance for RND and PC devices normalized to the NOPC device. ....	96

5-7	Ratio of IR/VIS for devices at 3 voltages.....	96
5-8	Brightness versus voltage curves for the three types of devices in this study, and for an “ideal” ACTFEL device.....	98

Abstract of Dissertation Presented to the Graduate School  
of the University of Florida in Partial Fulfillment of the  
Requirements for the Degree of Doctor of Philosophy

PHOTONIC CRYSTAL INTERACTIONS WITH ELECTROLUMINESCENCE  
FROM ZINC SULFIDE THIN FILMS DOPED WITH ERBIUM TRIFLUORIDE

By

Evan Stanley Law

August 2009

Chair: Paul H. Holloway

Major: Materials Science and Engineering

Photonic crystal (PC) interactions with the near-infrared emission at a wavelength of 1550 nm from zinc sulfide (ZnS) doped with erbium trifluoride ( $\text{ErF}_3$ ) have been studied in alternating current thin film electroluminescent (ACTFEL) devices. An objective of this study was to determine if propagation of light parallel to the surface would be frustrated by the PC and result in the increase of light intensity emitted perpendicularly to the surface. The thin film phosphor light emitting layer was deposited by radio frequency (RF) planar magnetron sputtering of a 1.5 mol%  $\text{ErF}_3$ -doped ZnS target and an undoped ZnS target onto the substrate stack consisting of an insulating  $\text{Al}_2\text{O}_3$ - $\text{TiO}_2$  (ATO) layer on a transparent conducting indium-tin oxide (ITO) layer on glass. A honeycomb structured PC was fabricated into the ZnS: $\text{ErF}_3$  layer by electron beam lithography on a polymer masking layer and the pattern was transferred into the ZnS: $\text{ErF}_3$  layer by argon sputtering. An insulating thin film layer of yttria-stabilized-zirconia (YSZ) or barium tantalate ( $\text{BaTa}_2\text{O}_6$ ) was deposited into the honeycomb structure of holes, creating the photonic crystal structure with a dielectric mismatch between the ZnS: $\text{ErF}_3$  layer of 20 or 11, for the YSZ and  $\text{BaTa}_2\text{O}_6$  respectively. Aluminum was then deposited as the top electrode in order to complete the ACTFEL device. The photonic band gaps were modeled for

input parameters including dielectric mismatch and honeycomb structure to determine the parameters of hole diameter and lattice spacing needed to achieve a photonic band gap for light at 1550 nm. For the structures used in this study, the lattice constant and hole diameter typically were on the order of 1000 nm and 350 nm respectively. The BaTa<sub>2</sub>O<sub>6</sub> structured PC affected the angularly resolved emission characteristics of the 1550 nm light by an ~18% increase in the light emitted at ~15 degrees off normal to the face of the device when compared to control devices. The angularly resolved emission of this device at 550 nm light was unchanged from the control devices. The YSZ structured PC ACTFEL device showed a two fold increase in 1550 nm light intensity versus a device without a PC structure as compared to the emission of 550 nm light which should not be effected by the PC structure. Analyses of the light scattering and reflection caused by the structure of the PC do not prove sufficient to explain the increase in 1550 nm emission of the PC device. Therefore, the increase in light intensity at 1550 nm is attributed to the PC effect of frustration of parallel light propagation to the surface resulting in the increase of light emitted perpendicularly to the surface.

## CHAPTER 1 INTRODUCTION

There has been significant recent research and development of alternating current thin film electroluminescent (ACTFEL) devices due to this technology's ability to compete in the lucrative displays market. This interest in ACTFEL displays comes from features such as high contrast, wide viewing angle, fast response time, low power, long operating life, crisp images and the capability for very high resolution; which have all led to commercially available visible light emitting ACTFEL displays [1]. In addition, it has been demonstrated that ACTFEL devices containing appropriate phosphors exhibit excellent near-infrared emission. There exist numerous applications requiring near-infrared emitters including telecommunications, phototherapy, chemical detection, friend-foe identification, and other night-vision technologies.

A major limitation in the emission efficiency of ACTFEL devices is due to light produced in the phosphor thin film layer being reflected at the surrounding interfaces such as the dielectric/transparent conducting oxide and transparent conducting oxide/glass substrate interface. Only approximately 10% of the total light generated is able to outcouple, i.e. transfer from the phosphor layer to air, from the device [2]. Techniques that have been used to improve the optical outcoupling include resonant cavities [3], high-reflectivity heterostructures [4], surface texturing [5], reshaping the light escape cone [6], coupling to surface plasmon modes [7] and photonic crystal slab structures [8]. Photonic crystal (PC) structures have proven capable of inhibiting propagation of light in particular directions and at wavelengths that are determined by the geometry, spacing and dielectric constant contrast of the PC. The main purpose of this research is to increase near-infrared light emission of ACTFEL devices by incorporating a photonic crystal structure into the device which inhibits light propagation modes which undergo

total internal reflection and the transferring of this energy to light modes of propagation which outcouple from the device.

A relevant literature survey of ACTFEL devices, their structure, operating physics and material composition as well as an overview of photonic crystal physics is presented in Chapter 2. Chapter 3 presents details of the fabrication techniques used to create ACTFEL devices containing the photonic crystal structure and the characterization methods used to analyze these devices. Chapter 4 details the experimental procedure and the angle resolved light emission data for one type of photonic crystal ACTFEL devices. The results of near-infrared enhancement of another type of photonic crystal ACTFEL device are presented in chapter 5. Finally, conclusions and future work are presented in chapter 6.

## CHAPTER 2 LITERATURE REVIEW

### 2.1 Electroluminescence

A phosphor is a material that when excited by a source of energy emits photons. The exciting energy may be photonic, electronic, ionic or thermal in nature. Photon emissions over a short time period, those that decay within a few nanoseconds, are known as fluorescence [9]. Luminescence over a much longer duration, as long as several hours, is called phosphorescence [10]. Photoluminescent devices contain phosphors that are excited by higher energy photon sources, usually ultraviolet lamps and lasers, typically producing a lower energy emission [11]. Cathodoluminescent phosphors produce photons when struck by energetic electrons [12]. One of the most common cathodoluminescent systems is a standard cathode ray tube in a television. Electroluminescent devices produce emission when an electric field is applied across the phosphor [13]. Electroluminescence (EL) is the phenomenon in which electrical energy is converted to luminous energy without thermal energy generation [14]. Electroluminescence is the source of light emission which is most important to this work.

#### 2.1.1 History

Electroluminescent observations were first reported in 1929 by Guden and Pohl, who demonstrated the effect on the photoluminescent decay of a ZnS:Cu phosphor [15]. Destriau's reported observation of light emission from a suspension of ZnS:Cu in oil in 1936 is often cited as the first observation of electroluminescence [16]. It was not until the 1950s that electroluminescence received attention, when GTE Sylvania obtained a patent for an EL powder lamp [17]. Research was then directed into the use of powder EL phosphors in hopes of a brighter and longer-lasting light source. This research faded when it was determined that the minimum acceptable lifetime of 500 hours for a commercial application would not be achieved

with these phosphors. Up until the late 1960s lifetimes, defined as the time it takes for the luminance of the device to drop by one half, were in the range of hundreds to a thousand hours [18].

A second era of EL development started in the late 1960s in correspondence with a renewed interest in display technologies. The first DC powder EL device made by coating powder EL phosphors with copper ions was reported in 1968 by Vecht [19]. Also, an alternating current (AC) Zinc Sulfide thin-film doped with rare-earth fluorides EL device was reported around the same time by Kahng [20]. New process technologies in electronics and materials science allowed for the development of these devices. Kahng proposed that his device was driven by Lumocens, luminescence from molecular centers, through a mechanism of impact ionization of luminescent centers by “hot” electrons resulting in electroluminescence (EL).

One of the first major milestones towards thin-film electroluminescent display technology was the introduction of the insulating layer/phosphor/insulating layer sandwich structure proposed by Russ and Kennedy in 1967 [21]. In 1974, Inoguchi et al. were able to resolve the problems of previous research into EL devices by reporting a triple-layered, thin-film EL (TFEL) device, consisting of a  $\text{ZnS:Mn}^{2+}$  EL layer sandwiched by a pair of insulating layers, which showed high luminance and an unusually long lifetime [22]. Mito et al. followed these findings by showing that these EL panels could be used as a TV imaging system [23]. The  $\text{ZnS:Mn}$  phosphor layer emitted a yellow light leading to the early TFEL displays being monochrome. Sharp introduced a monochrome television display in 1978 [24]. Alternating current thin-film electroluminescent devices (ACTFELDs) have experienced a higher level of interest due to the preceding research and the high probability of these devices being used in information displays. Uede et al. and Takeda et al. produced  $\text{ZnS:Mn}$  EL displays in 1981 [25,

26]. By the mid-1980s ZnS:Mn thin-film displays were also being introduced by Planar Systems and Finlux [27].

The color limitation of the ZnS:Mn phosphor aided by competition and further research resulted in a drive for multicolored displays. First, filtering was used to produce red and green light in order to achieve a multicolor display. Research was also driven in the direction of finding additional dopants that would emit light of different color. Different rare earth ions were found to emit red, green and blue light when doped into ZnS [28, 29]. By the mid-1980s multicolor displays were introduced by Coover et al. (Planar Systems) [30]. By 1994, Planar Systems had introduced a prototype full color ACTFEL display [31]. Table 2-1 summarizes some of the major accomplishments of EL research using ZnS.

Table 2-1 History of the development of high-field EL in ZnS [2]

1936	Discovery of High field electroluminescence (Destriau)
1950	Development of transparent conducting films ( $\text{SnO}_2$ ); development of AC powder EL devices
1950-1960	Basic studies on AC powder EL devices (Problems: Low luminance and short lifetime)
1960	ZnS:Mn thin-film EL structure (Vlasenko and Popkov)
1964-1970	Electroluminescent thin film research (Reported in 1972) (Soxman and Ketchpel)
1967	Double insulating layer type AC thin-film EL device structure (Russ and Kennedy)
1968	High luminance thin-film EL devices with luminescence from molecular centers (Kahng)
1974	High luminance and long lifetime AC thin-film EL display (Inoguchi et al.)
1974	Application of AC thin-film EL display to TV imaging system (Mito et al.)
1974	Memory effects in ZnS:Mn AC thin-film EL display (Yamauchi et al.)
1981	Practical AC thin-film display unit (Uede et al.)
1983	Start of volume production of AC thin-film EL displays (Takeda et al.)
1988	Prototype full-color thin-film EL display demonstrated by Barrow and coworkers.
1990s	Alternating-current powder EL devices developed for specialty lighting.
1993	First commercial multicolor (red/green/yellow) ZnS:Mn AC thin-film EL display introduced by Cramer et al.
1994	First commercial full-color AC thin-film EL display panel

As a result of research into the use of ZnS doped with rare earth ions for ACTFELDs, their infrared emissions properties were found. These emissions were treated negatively due to the fact that they reduced the efficiency of the visible emissions. Neodymium and erbium doped in ZnS were found to emit in both the visible and infrared wavelengths of light. ZnS doped with thulium has a strong near-infrared (NIR) emission which weakened the blue emission, thereby limiting its use in display devices [32]. ZnS doped with erbium produces a green emission and a strong NIR emission at the wavelength of 1.55  $\mu\text{m}$  which is of great interest in the telecommunications industry due to low attenuation of this wavelength in optical fibers [33, 34].

### **2.1.2 ACTFEL Device Structure**

Russ and Kennedy's first proposed double insulating layer sandwich structure has been adapted into what is now used as the most common device structure. This structure is the standard metal-insulator-semiconductor-insulator-metal (MISIM) or "full stack" structure [35] as shown in figure 2-1 (a). A transparent glass substrate such as Corning 7059 glass is typically used due to its benefits: high availability at low cost and the ability to produce many sizes. These benefits, however, are overshadowed by the importance of the fact that it does not contain alkali metals which have been found to diffuse into the semiconductor phosphor layer over time and cause device degradation [2]. However, this glass may not be used for some EL structures which require high temperature anneals above the 844°C [36] softening point of Corning 7059 glass. In these cases, glass-ceramic must be used, which can cost 10 times as much as Corning 7059 glass. A transparent electrode is deposited on top of the glass followed by a transparent insulator, phosphor layer, a second transparent insulator layer, and finally a reflecting opaque electrode. Emitted light from the phosphor layer ultimately transmits out of the glass layer for this device structure. The double insulating layers also prove beneficial in that they can protect the phosphor layer from moisture leading to better stability [18]. Aluminum is typically used for

the reflecting opaque electrode due to its high level of reflectivity and its ability to “self-heal”. Self-healing is necessary to prevent electrical shorts that develop in the ACTFEL device that could lead to catastrophic breakdown. Aluminum has the ability to limit the failure to a localized region due to rapid fusing of the aluminum by large current flow from the short circuit [37]. Aluminum is also relatively easy to deposit by thermal evaporation by resistive heating of a tungsten crucible or by electron beam evaporation.

By a slight modification to the full stack “normal” structure the result is the so-called “inverted” structure as shown in figure 2-1 (c). This structure is beneficial due to the fact that it allows for the substrate to be opaque. This enables the use of ceramic substrates which can withstand higher annealing temperatures as required to optimize certain phosphor microstructures for enhanced performance. In the inverted structure the top insulator and electrode must be transparent [2, 38]. Active matrix and thick film dielectric hybrid EL devices utilize this structure [39, 40]. One disadvantage to the inverted structure is the loss of the ability to use aluminum as the top electrode thus losing the beneficial self-healing quality of the aluminum. Other advantages of the inverted structure include the ability to use silicon as a substrate which allows for easy incorporation of devices into existing silicon-based semiconductor devices. Organic filters used for full and multicolor displays can more easily be used after the high temperature anneals of the phosphor layer since the organic layers can be deposited last which is not the case with the normal device structure.

It is possible to remove one of the insulating layers of the full stack structure and be left with a “half stack” structure, as shown in figure 2-1 (b). Device performance in terms of brightness may be affected beneficially or detrimentally [41]. Device stability is compromised in

the half stack structure, but due to the benefit of faster processing time this structure is sometimes utilized for research purposes.

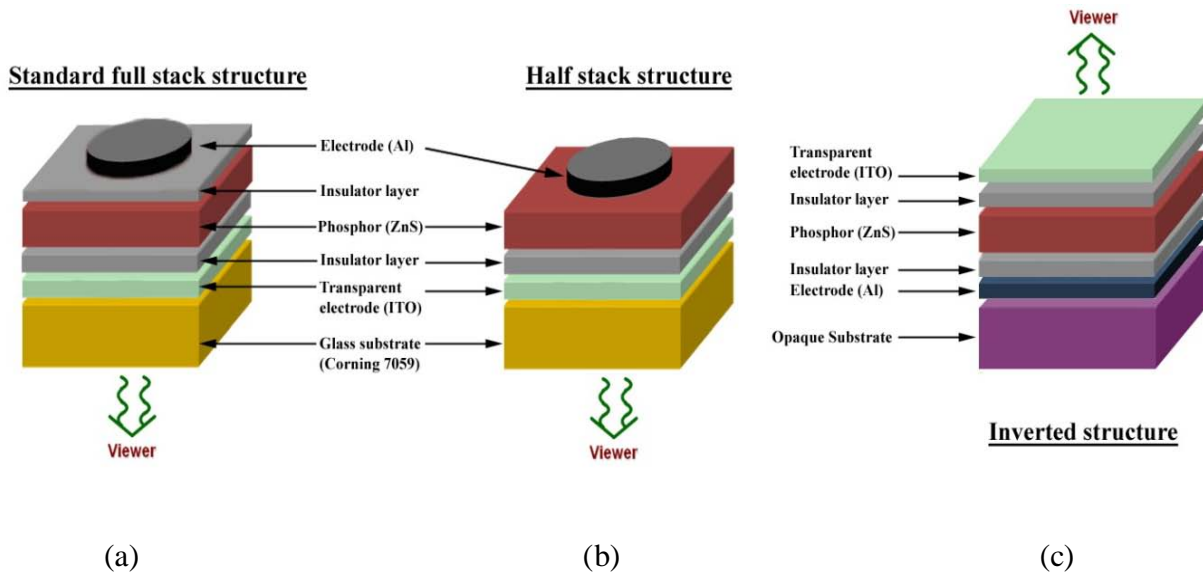


Figure 2-1 Full stack, Half stack and Inverted structure schematics

### 2.1.3 ACTFEL Device Physics and Optical Characteristics

In ACTFEL device operation there are six basic processes involved in EL as illustrated in figure 2-2 and summarized as follows.

1. Electron injection by high-field-assisted tunneling from states at the phosphor insulating layer interface at voltages above threshold voltages.
2. Acceleration and increased kinetic energy of injected electrons to the level necessary for excitation in the phosphor layer.
3. High-energy electrons called hot electrons directly excite luminescent centers through impact-excitation. When excited electrons in the luminescent centers undergo a radiative transition to the ground state, photons are emitted.
4. Hot electrons travel through the phosphor layer and are trapped at the phosphor/insulator interface causing polarization.
5. When the AC polarity is reversed, these processes occur in the reverse direction.
6. Photons generated from the luminescent centers of the ACTFELD escape to outside of the device and can be observed [2, 42].

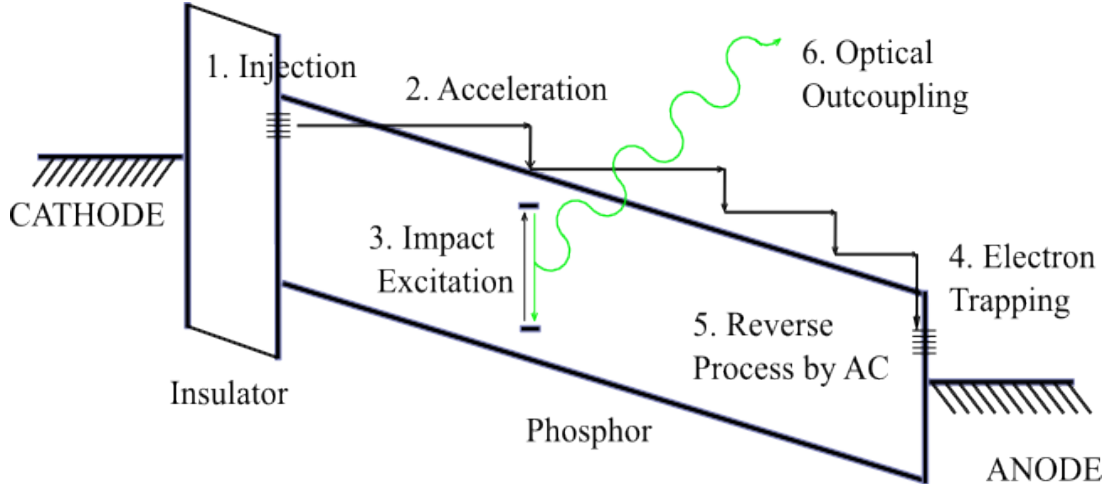


Figure 2-2 Basic ACTFEL device operational processes [2]

The primary concern of this research is process number 6. Understanding any process that affects outcoupling is necessary in determining how to increase outcoupling.

The efficiency of a device will give information about the light outcoupling. The internal radiative efficiency,  $\eta_q$ , is a measure of the radiative transitions with respect to non-radiative transitions for the electroluminescence process and is given in equation 2.1,

$$\eta_q = (1/t_r)/(1/t_r + 1/t_{nr}) = 1/(1 + t_r/t_{nr}) \quad (2.1)$$

where  $t_r$  and  $t_{nr}$  are the radiative and non-radiative lifetimes. The external quantum efficiency is the overall efficiency of a device, taking absorption and reflection of emitted photons into account. Light is absorbed according to  $\exp(-\alpha d)$ , where  $d$  is the distance the light has traveled and  $\alpha$  is the absorption coefficient which is dependent on the wavelength of the light. Light hitting an interface at an angle greater than the critical angle ( $\theta_c$ ) will experience total internal reflection that will lower the external quantum efficiency. The external quantum efficiency,  $\eta_{ext}$ , can be reduced to the function given in equation 2.2.

$$\eta_{ext} = \eta_q (1-R) (1 - \cos \theta_c) \exp(-\alpha d) \quad (2.2)$$

In this equation  $R$  is the reflection coefficient at the interface given by equation 2.3.

$$R = (n_2 - n_1)^2 / (n_2 + n_1)^2 \quad (2.3)$$

The internal quantum efficiency can be very high in electroluminescent devices; unfortunately the external quantum efficiency is usually very low in these same devices [43]. The optical outcoupling efficiency, defined as the fraction of light that leaves the device with respect to total light generated or internal divided by external quantum efficiency, is given by equation 2.4.

$$\eta_{\text{opt}} = \int_0^{\arcsin(2/n_1)} \sin \theta d\theta \quad (2.4)$$

The optical outcoupling efficiency is only about 10% when only taking into account the simplified system consisting of the ZnS ( $n = 2.39$  at 550nm [44]) layer and air ( $n = 1$ ) [2, 45, 46, 47]. When the ACTFEL device structure is idealized with perfectly smooth interfaces, ray tracing according to Snell's law ( $n_1 \sin \theta_1 = n_2 \sin \theta_2$ ) can be performed for light traveling from the phosphor layer to the air, as seen in figure 2-3.

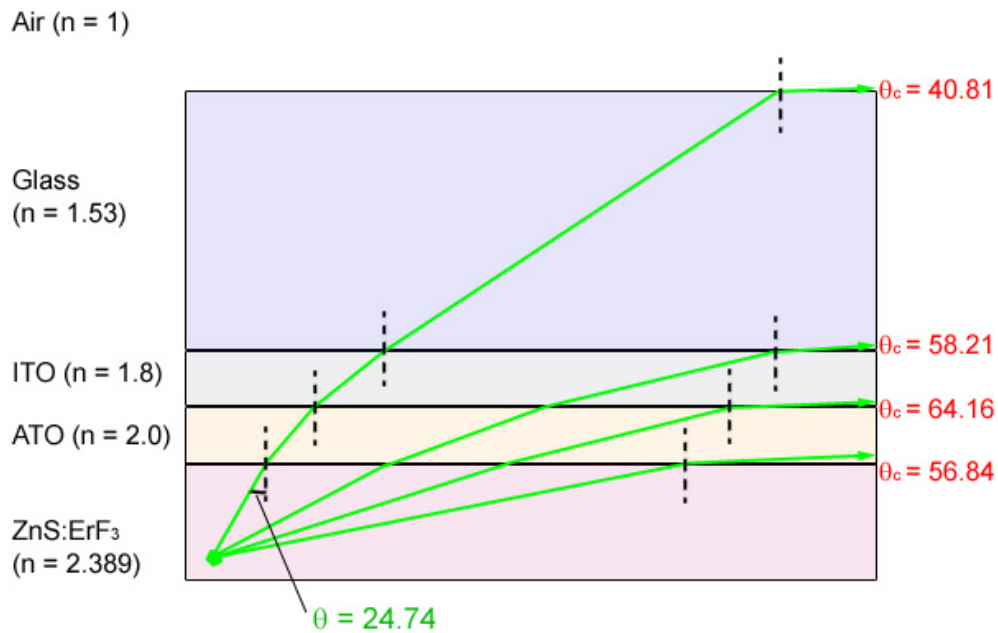


Figure 2-3 Ray tracing diagram of ACTFEL structure

From figure 2-3 it is clear that the majority of the light produced in the phosphor layer will undergo total internal reflection at some interface in the device. For light emitted from the ZnS:ErF<sub>3</sub> layer to escape into air it must intersect with the ATO layer at angles between normal

and about  $25^\circ$  to normal. Light striking the interface between these angles will be able to escape because even after being refracted through the ATO, ITO and glass layers the light will not have been sufficiently bent to surpass the critical angle between glass and air and will be able to transfer across that interface. The case in which surfaces are not completely smooth leads to scattering which is discussed in section 2.4.

The optical response of an electroluminescent device to an applied electrical driving force is the key consideration in performance. Performance is evaluated by luminance versus voltage (L-V) measurements that are made by applying an AC voltage to the device while measuring the luminance output through a spectrometer. The L-V data can be used to determine threshold voltage ( $V_{th}$ ), the luminance at  $V_{th} + 40$  V ( $L_{40}$ ), and the luminous efficiency. The threshold voltage is often determined by the voltage value at the intersection of a line drawn in conjunction with the rising region of the brightness versus voltage curve and the voltage axis. The dielectric properties of the insulator and phosphor layers affect  $V_{th}$  and can be used to control  $V_{th}$  by varying the layer thicknesses. An increased phosphor layer thickness leads to an increased  $V_{th}$  and vice versa. At above  $V_{th}$  levels the brightness usually increases linearly with voltage due to the proportionally increasing phosphor electric field until the phosphor brightness saturates or dielectric breakdown occurs in the phosphor layer. Therefore most ACTFEL devices are driven above threshold, e.g. at 40 V above [2]. The  $L_{40}$  value is used when comparing devices and it is important to be aware of the fact that  $L_{40}$  increases with phosphor thickness (because more luminescent centers can be excited) and with AC frequency (because electrons make more passes across the phosphor layer, increasing luminescent excitations).

EL spectral data are used to determine CIE coordinates, which are a measure of the color of the light emitted from a device. The luminous efficiency ( $\text{lum W}^{-1}$ ) is a vital parameter

obtained from the L-V data. Assuming a perfectly diffuse emitting surface, dividing the luminance ( $\text{cd m}^{-2}$ ) by the power density ( $\text{W m}^{-2}$ ) and multiplying by  $\pi$  gives the luminous efficiency. ACTFELD luminous efficiency is typically reported for devices driven at 60Hz at  $V_{\text{th}} + 40\text{V}$ . The luminance  $L_{40}$  value can be determined from the L-V curve and the power at  $V_{\text{th}} + 40\text{V}$  can be obtained from a charge versus voltage plot in order to determine luminous efficiency. Optical data obtained comparing photonic crystal patterned devices to non-patterned devices will be critical to this research.

## **2.2 ACTFEL Material Requirements**

### **2.2.1 Substrate Materials**

Requirements for the ACTFELD's substrate include a high transmission coefficient for the wavelength of interest, a coefficient of thermal expansion close to that of the deposited films for annealing steps, a low alkali metal content to prevent degradation by diffusion of metal ions into the phosphor layer, low cost and availability. Corning 7059 barium borosilicate glass is the most frequently used substrate for visible ACTFELDs as well as for LCD substrate [48].

Anneals as high as  $650^{\circ}\text{C}$  may be achieved with this glass without significant warping due to its softening point of  $598^{\circ}\text{C}$  [49]. Small samples may even withstand anneals as high as  $850^{\circ}\text{C}$  for short time periods. Corning 7059 glass has high transmission over the visible spectrum of light as shown by its transmission spectrum in figure 2-4.

For device applications which require higher temperature anneals in order to obtain the proper materials microstructure for the properties desired or for applications requiring higher transmission in the mid-infrared spectrum, a different substrate is necessary. Silicon is typically the substrate chosen for this type of application. Silicon, with high doping density, can even be used as the bottom electrode of the inverted device structure. Silicon substrates can be annealed up to  $1400^{\circ}\text{C}$ , allowing for much higher-temperature processing of the deposited films. Silicon

can be a good choice for IR-emitting devices for either the standard or inverted structures because it has a high transmission coefficient in the NIR as well as up into the mid-infrared region [51].

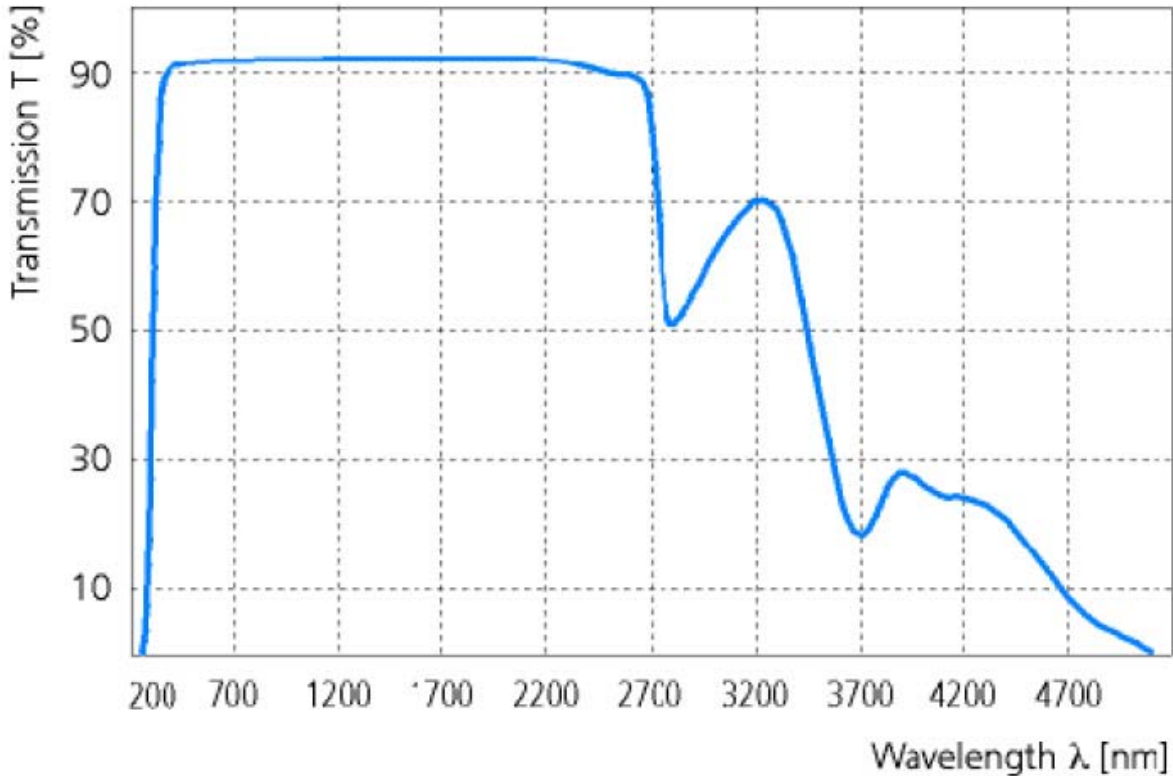


Figure 2-4 Transmission spectrum of Corning 7059 glass [50]

### 2.2.2 Insulating Materials

The insulating layers have a vital role to play in the electric function of ACTFEL devices. The phosphor layer is situated in direct contact with either one or two insulating layers, which can be either the same or different material. The insulator-phosphor interface functions as the source for charge carriers for luminescence. The primary function of the insulator layer is to prevent the destruction of the phosphor layer at high electric fields which may result in runaway avalanche breakdown. Typically, electric fields must be greater than 2 MV/cm for this breakdown to occur. Table 2-2 outlines the requirements for dielectric layers. For high

efficiency it is desirable for most of the applied voltage to drop across the phosphor layer and not across the insulating layers. The capacitances of the phosphor and insulating layers determine the proportion of the voltage drop across each.

Table 2-2 Requirements for dielectric layers [2, 52-57]

---

1.	High dielectric constant.
2.	High breakdown electric field strength.
3.	Must provide interface states at the phosphor-insulator interface, from which electrons can tunnel into the phosphor conduction band.
4.	A limited number of defects and pinholes. Defects and pinholes act as sites for local field enhancement and premature dielectric breakdown.
5.	Good mechanical adhesion to both phosphor and conductive layers.
6.	Good thermal and chemical stability over the processing temperature range (i.e. up to 650°C)
7.	Transparency for the chosen emission wavelengths.

---

The capacitance (C) of a layer is equal to the permittivity of free space ( $\epsilon_0$ ) times the relative permittivity ( $\epsilon_r$ ) divided by the layer thickness (t), as shown in equation 2.5 [58].

$$C = (\epsilon_0 \epsilon_r) / t \quad (2.5)$$

High insulator layer capacitance compared to the phosphor layer capacitance results in a large voltage drop across the phosphor, as shown by the correlation of capacitance to voltage (V) of equation 2.6, where Q is the charge.

$$C = Q / V \quad (2.6)$$

Achieving a large voltage drop across the phosphor layer can be accomplished by either a high relative dielectric constant of the insulating layer versus the phosphor layer and/or by keeping the insulator layer very thin. However, insulators with thicknesses less than 50 nm have been reported to exhibit detrimental charge leakage [59]. The insulating layers also require high dielectric breakdown strength to ensure stability and to prevent electric breakdown.

Unfortunately most insulators with high dielectric constants have low dielectric breakdown strengths. There are two modes of breakdown for EL devices: propagating and self healing.

Propagating breakdown leads to a large area of electrical breakdown while self-healing

breakdown remains localized. It is important for insulator layers to exhibit the self-healing breakdown mode, but high-dielectric thin films tend to exhibit propagating breakdown. By coupling dielectric thin films, the breakdown mode can be converted into the self-healing mode [60]. A figure of merit was developed by Howard to rate insulators for ACTFEL applications [56]. This is the product of the dielectric constant and the electrical breakdown field and is a measure of the maximum trapped charge density ( $\mu\text{C}/\text{cm}^2$ ) at the insulator-phosphor interface. Table 2-3 shows a comparison of important properties for different insulators, where  $E_{bd}$  is the electric breakdown field, SHB is self healing breakdown and PB is propagating breakdown.

Table 2-3 Insulators used for ACTFEL devices and their properties [2]

Insulator	Deposition Method*	$\epsilon_r$	$E_{BD}$ (MV/cm)	$\epsilon_o\epsilon_r E_{BD}$ ( $\mu\text{C}/\text{cm}^2$ )	Breakdown Mode**
SiO <sub>2</sub>	Sputtering	4	6	2	SHB
SiOxNy	Sputtering	6	7	4	SHB
SiOxNy	PVCD	6	7	4	SHB
Si3N4	Sputtering	8	8 to 9	4 to 6	SHB
Al2O3	Sputtering	8	5	3.5	SHB
Al2O3	ALE	8	8	6	SHB
SiAlON	Sputtering	8	8 to 9	4 to 6	SHB
Y2O3	Sputtering	12	3 to 5	3 to 5	SHB
Y2O3	EBE	12	3 to 5	3 to 5	SHB
BaTiO3	Sputtering	14	3.3	4	SHB
SmO3	EBE	15	2 to 4	3 to 5	SHB
HfO2	Sputtering	16	0.17 to 4	0.3 to 6	SHB
Ta2O5-TiO2	ALE	20	7	12	SHB
BaTa2O6	Sputtering	22	3.5	7	SHB
Ta2O5	Sputtering	23-25	1.5 to 3	3 to 7	SHB
PbNb2O6	Sputtering	41	1.5	5	SHB
TiO2	ALE	60	0.2	1	PB
Sr(Zr,Ti)O3	Sputtering	100	3	26	PB
SrTiO3	Sputtering	140	1.5 to 2	19 to 25	PB
PbTiO3	Sputtering	150	0.5	7	PB
BaTiO3****	Press/sinter	5000	?	?	?
Westaim proprietary***	Press/sinter	1700	?	?	?

### 2.2.3 Transparent Conductors

The requirements for transparent conducting layers for EL devices are high conductivity and transmittance. High conductivity is especially desired for display uniformity and to decrease the power consumption due to Joule heating [18]. One of the first materials used was SnO<sub>2</sub> having a resistivity of 10<sup>-3</sup> Ω-cm. Although this material has excellent stability, it is currently not used due to difficulty of patterning by chemical etching. The most widely used material at this time is indium-tin oxide (ITO). This is an alloy typically consisting of 90 wt% In<sub>2</sub>O<sub>3</sub> with 5-10 wt% SnO<sub>2</sub>. ITO is optically transparent (>90%) over the visible region and part of the NIR, and can be deposited by any number of deposition techniques, including pulsed-laser deposition, electron beam evaporation, DC magnetron sputtering, RF magnetron sputtering, plasma ion-assisted deposition, chemical vapor deposition and atomic layer deposition [2, 61-70]. An advantage of sputter deposition of ITO is the very smooth surface which can be obtained by this method. The ITO layer used for ACTFEL devices is typically 200 nm thick with a resistivity of 10<sup>-4</sup> Ω-cm. The conductivity of ITO can be attributed to thermal ionization of shallow donors which arise from substitution of Sn<sup>+4</sup> on In<sup>+3</sup> lattice sites, as well as oxygen vacancies [71]. The conductivity of ITO may be affected by temperature; thus, care must be taken during the fabrication process. ITO lacks transparency for wavelengths greater than around 1.6 to 2 μm limiting its usefulness for NIR-emitting ACTFELDs [71]. At longer wavelengths a silicon substrate doped for conductivity as used in the inverted stack structure may become necessary [47].

### 2.2.4 Phosphor Materials

Phosphor systems consist of a host material and a luminescent center. The host must possess certain properties in order to achieve high-field electroluminescence. In order for light that is generated in the phosphor not to be absorbed the host material should have a sufficiently

large band gap. For near-infrared emission the host band gap must be at least 1.6 eV and for visible emission the band gap must be at least 3.1 eV. The host material must also be non-conducting below the luminescence threshold, so that at sub-threshold levels the host will act as a capacitor. It should also have a high enough dielectric breakdown strength to allow electrons to reach appropriate energies to be able to excite luminescent centers. The breakdown field of the host must be at least 1 MV/cm. The host material should be able to maintain good crystallinity even with doping levels on the order of 1 atomic percent. Finally, the host must have a substitutional lattice position of appropriate symmetry to incorporate the luminescent center.

Satisfying these requirements has typically been achieved by using sulfur-based compounds. Among the possible choices are sulfides (e.g. ZnS, SrS and CaS) and thiogallates (e.g. CaGa<sub>2</sub>S<sub>4</sub>, SrGa<sub>2</sub>S<sub>4</sub> and BaGa<sub>2</sub>S<sub>4</sub>) [14, 27, 72, 73]. Table 2-4 lists the physical and electrical properties of the sulfide II-VI host materials.

Table 2-4 Properties of some II-VI ACTFEL host materials [2]

Property	IIb-VIb compound	IIa-VIb compound	
Compound	ZnS	CaS	SrS
Melting Pt. (°C)	180-1900	2400	>2000
Band Gap (eV)	3.6	4.4	4.3
Transition Type	Direct	Indirect	Indirect
Crystal Structure*	ZB,W	Rock salt	Rock salt
Lattice constant (Å)	5.409	5.697	6.019
Dielectric const.	8.3	9.3	9.4
Ionicity	0.623	>0.785	>0.785

\*ZB = zinc blende; W = wurtzite; Orth. = orthorhombic

ZnS has dielectric breakdown strength of about 1.5 MV/cm, making it sufficient to act as a capacitor at low fields and a conductor at high fields [74]. It also has a band gap of 3.6 eV making it transparent from 400 nm to 10 μm [75]. These properties allow ZnS to serve as an appropriate host material choice for visible and near-infrared electroluminescent devices.

Luminescent centers which are incorporated into the host material are the source of light emission and determine the emission wavelengths of the phosphor. There are three main aspects to consider regarding luminescent centers: radiative kinetics, cross-section for excitation and radiative transition energy. Radiative kinetics refers to the event of a luminescent center being excited by an electron impact excitation causing the luminescent center to undergo a de-excitation resulting in either a radiative photon emission or a non-radiative phonon which produces heat and lattice vibrations. The radiative efficiency as a function of temperature is shown in equation 2.7 where  $W_r$  and  $W_{nr}$  are the radiative and non-radiative recombination rates [76].

$$\eta(T) = \frac{I}{I(0)} = \frac{W_r}{W_r + W_{nr}} \quad (2.7)$$

The probability that a high-energy electron will excite a luminescent center is related to the cross-section for excitation. The cross-section for excitation is approximately proportional to the geometric cross-section of the ionized luminescent center when substituted in the host matrix [77]. The radiative transition energy determines the emitted photon energy and therefore its wavelength. In most ACTFEL devices the radiative mechanism of light emission is from an atomic transition of the luminescent center resulting in emitted wavelength dependence on luminescent material; however, the photon energy can be affected by the host material [78].

Considering when radiative relaxation occurs in the luminescent centers, in which a localized transition occurs between different electronic states of the isolated luminescent center (dopant), the emission that results depends on the excited state energy and the lower state energy to which the electron relaxes. Understanding emissions from this type of electronic transition requires the use of quantum mechanical selection rules. The parity selection rule forbids transitions between energy levels of the same parity and the spin selection rule forbids transitions

between configurations with different spin states [77]. Common luminescent centers for ZnS are transition metal ions, which include  $\text{Ti}^{4+}$ ,  $\text{Cr}^{2+}$ ,  $\text{Mn}^{2+}$ ,  $\text{Cu}^+$  and  $\text{Ag}^+$ . All of these have a  $d^n$  valence configuration where emissions from d orbital transitions are strongly influenced by the local crystal field of the host material [2]. Rare earth and lanthanide ions such as  $\text{Nd}^{3+}$ ,  $\text{Eu}^{3+}$ ,  $\text{Eu}^{2+}$ ,  $\text{Tb}^{3+}$ ,  $\text{Er}^{3+}$  and  $\text{Tm}^{3+}$ , are also used as luminescent centers in ZnS phosphors [2]. Lanthanide ions have electron configurations such that the  $5s$ ,  $5p$  and  $6s$  orbitals are filled, but the  $4f$  orbital is not filled. Transitions in the  $4f$  orbital are shielded from the crystal field of the host material by the  $5s$ ,  $5p$  and  $6s$  electrons. Figure 2-5 shows partial energy level diagrams for  $\text{Tm}^{3+}$  with blue emissions,  $\text{Er}^{3+}$  with green emissions and  $\text{Nd}^{3+}$  with orange and near-infrared emissions.

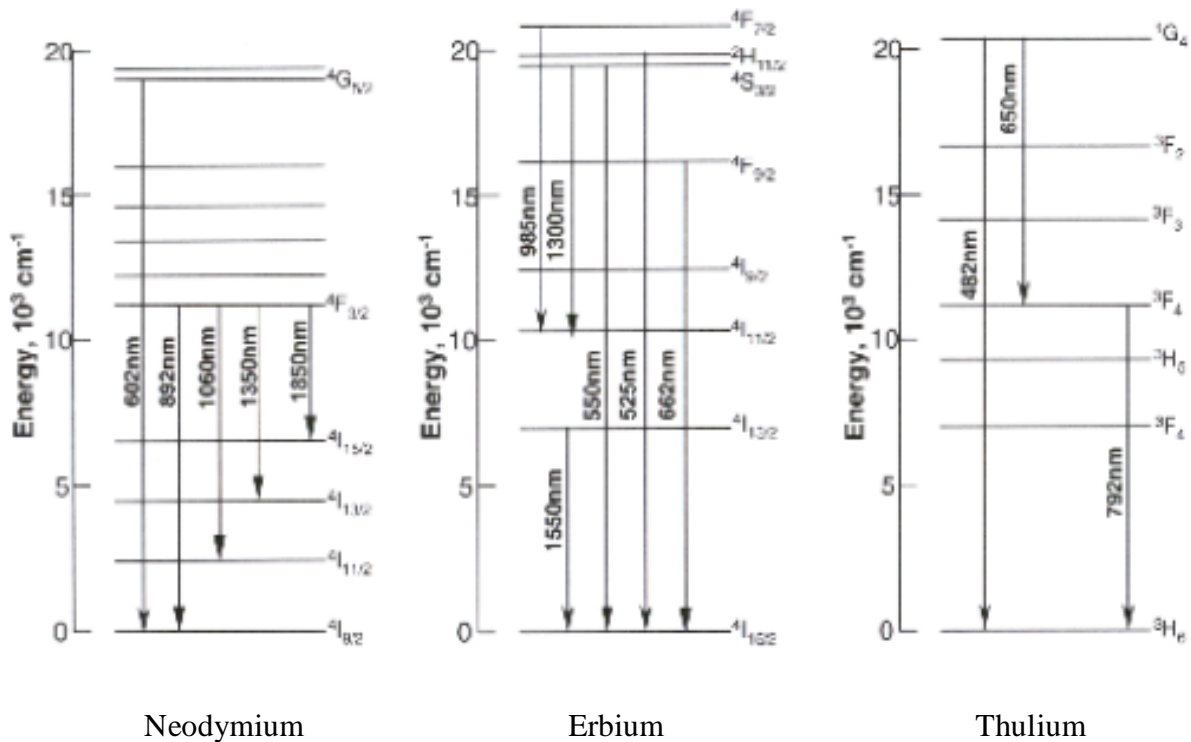


Figure 2-5 Partial energy level diagrams for neodymium, erbium and thulium [79, 80]

These ions have multiple emission lines and even emit in the infrared leading to their use in applications beyond information displays.

Luminescent centers normally sit on substitutional cation sites in the host lattice; therefore, the charge difference between the dopant ion and displaced host ion must be compensated to maintain charge neutrality. Interstitially doped halide ions such as  $F^-$  and  $Cl^-$  are the most common type of charge compensators. Oberacker and Schock have studied the effects of choice of halide on SrS:Ce ACTFEL emissions and they showed no appreciable influence on blue EL when samples were codoped with LiCl, but when doped with LiF there was a distinct red shift resulting in green emission [81]. Post-deposition annealing has been shown to affect the concentration of fluorine [47], with F concentration in ZnS:TbF<sub>3</sub> decreased by annealing temperatures over 300°C [82, 83]. The Tb concentration was unaffected by annealing and the ratio of fluorine-to-terbium (F/Tb) decreased from 3/1 in the as-deposited condition to 1/1 in films annealed at 550°C. This corresponded to a four-fold increase in green emission [82].

Erbium is one of the rare earth ions most known for infrared emissions. Erbium contains an energy transition equivalent to a 1550 nm wavelength of light as shown in figure 2-5. This 1550 nm near-infrared (NIR) emission is used in fiber optic cables due to the low attenuation of 1550 nm light traveling through typical fiber optic cables as mentioned previously [34]. A typical EL response spectrum obtained from a ZnS:ErF<sub>3</sub> ACTFEL device is shown in figure 2-6. The major peaks are located about the wavelengths of 525, 550, 662, 985 and 1550 nanometers. The ratio of visible-to-infrared emission intensities has been reported to depend on both the host material and the erbium concentration [84]. Kale et al. have shown that annealing of ZnS:ErF<sub>3</sub> films results in enhancement of the infrared luminescence from ACTFEL devices [51]. Increased infrared and decreased visible emissions have been reported for annealing temperatures up to 425°C for 1 hour in a nitrogen atmosphere. This was attributed to defect

removal from the film upon annealing, allowing acceleration of ballistic electrons to higher energies.

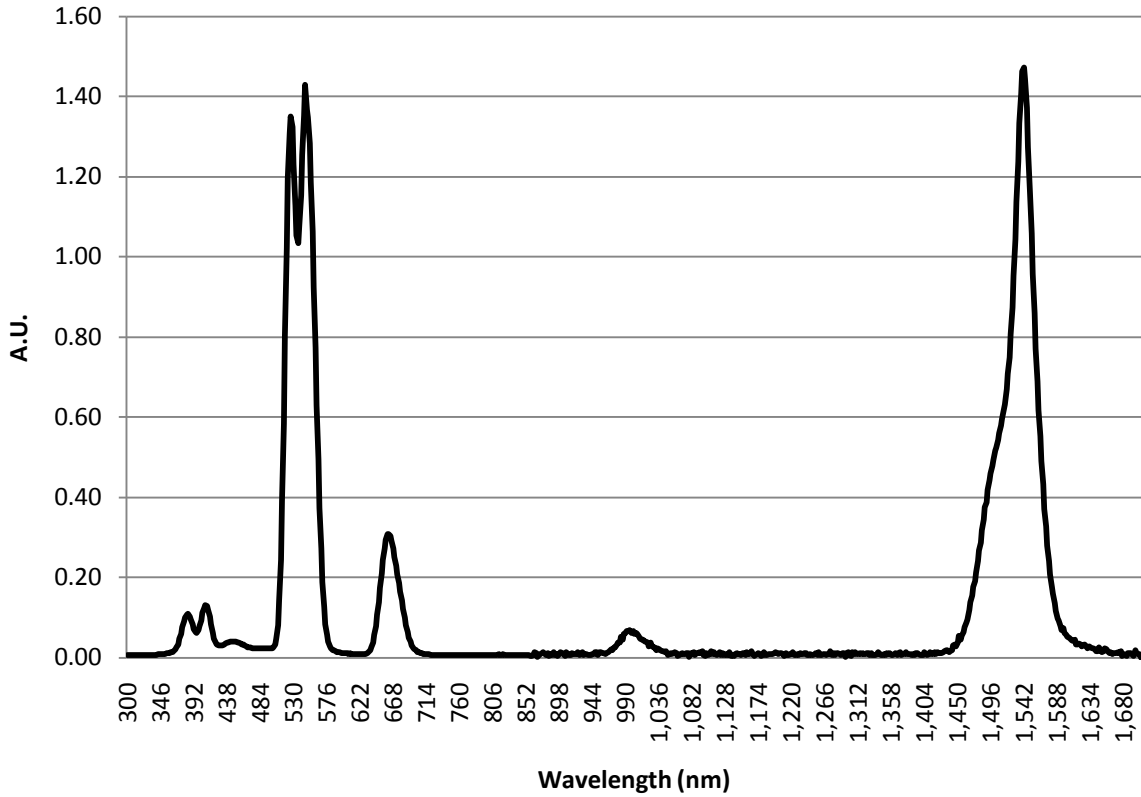


Figure 2-6 ZnS:ErF<sub>3</sub> ACTFEL device EL response spectrum

### 2.3 Photonic Crystals

Photonic crystals (PCs) are structures consisting of two or more electromagnetic materials of differing dielectric constant constructed with a periodicity of proper scale to create a photonic band gap. This optical band gap is comparable to a semiconductor’s electronic band gap arising from the interaction of the electron wavefunction with a crystalline periodic atomic lattice. Photonic crystals that are periodic in one, two and three dimensions are termed 1-D, 2-D and 3-D. Lord Rayleigh was the first to investigate electromagnetic wave propagation in a periodic medium; for example, he researched the effects of gratings with a size less than the wavelength of light and suggested the recesses acted as resonators [85]. In 1987 Yablonovitch

and John introduced the idea of a full directional photonic band gap in two and three dimensions leading to the term “photonic crystal” [86].

### 2.3.1 Maxwell’s Equations in Periodic Media [86]

In order to model electromagnetic waves in interactions with electromagnetic media, Maxwell’s equations are used, just as Schrödinger’s equation is used for electron interactions with atomic crystal lattices. By combining the third and fourth Maxwell’s equations at a fixed frequency  $\omega$ , equation 2.8 with only the magnetic field  $\vec{H}$  is obtained.

$$\vec{\nabla} \times \frac{1}{\epsilon} \vec{\nabla} \times \vec{H} = \left(\frac{\omega}{c}\right)^2 \vec{H} \quad (2.8)$$

In equation 2.8,  $\epsilon$  is the dielectric function  $\epsilon(x,y,z)$  and  $c$  is the speed of light. This eigenfunction has eigenvalue  $\left(\frac{\omega}{c}\right)^2$  and eigen-operator  $\left(\vec{\nabla} \times \frac{1}{\epsilon} \vec{\nabla} \times\right)$  which acts the same to the left and right. It is also useful to write the generalized eigenfunction using the electric field  $\vec{E}$  as shown in equation 2.9.

$$\vec{\nabla} \times \vec{\nabla} \times \vec{E} = (\omega/c)^2 \epsilon \vec{E} \quad (2.9)$$

Electric fields in higher  $\epsilon$  will have lower  $\omega$ . A photonic crystal is a periodic array of dielectric media represented by the periodic dielectric function  $\epsilon(\vec{x}) = \epsilon(\vec{x} + \mathbf{R}_i)$  where  $\mathbf{R}_i$  are lattice vectors for an array periodic in all three dimensions. Solutions to the equation with magnetic field only are of the form  $\vec{H}(\vec{x}) = e^{i\vec{k}\cdot\vec{x}} \vec{H}_{n,\vec{k}}(\vec{x})$  with eigenvalues  $\omega_n(\vec{k})$ , where  $\vec{H}_{n,\vec{k}}$  is a periodic envelope function satisfying equation 2.10.

$$(\vec{\nabla} + i\vec{k}) \times \frac{1}{\epsilon} (\vec{\nabla} + i\vec{k}) \times \vec{H}_{n,\vec{k}} = \left(\frac{\omega_n(\vec{k})}{c}\right)^2 \vec{H}_{n,\vec{k}} \quad (2.10)$$

This function results in a different eigen value function for each wavevector  $\vec{k}$  of the primitive cell in the lattice. If the structure is periodic in all directions there will be discrete eigenvalues  $\omega_n(\vec{k})$  that are continuous functions of  $\vec{k}$  that form bands when plotted in a dispersion diagram.

Also,  $k$  can be complex corresponding to evanescent modes that exponentially decay from the boundaries of a finite crystal. Since the eigensolutions are periodic functions of  $k$ , it is possible to consider only the inequivalent wave vectors closest to the  $k = 0$  origin, which is called the first Brillouin zone. Further simplification may be achieved if the crystal contains symmetry elements that create redundancies leading to an irreducible Brillouin zone that is the smallest region within the first Brillouin zone for which the eigensolutions are not related by symmetry.

The situation in which there is no solution to Maxwell's equations over a range of  $\omega$  for all  $k$  is called a complete photonic band gap. Any periodic dielectric variation in one dimension leads to a band gap although it will be a small gap for a small variation. For periodic dielectric structures in 2 and 3 dimensions, there will exist 1-D band gaps in each symmetry direction of the structure, but these band gaps will not necessarily create a complete band gap in the 2 or 3-D structure because the 1-D band gaps will not necessarily overlap in frequency or lie between the same bands. In order for them to overlap the band gaps must be large, leading to a minimum  $\epsilon$  contrast. Since the 1-D band gap is inversely proportional to the period of the dielectric medium, for 2 and 3-D structures it is beneficial for the lattice constant to be invariant over different crystallographic directions. Thus a crystal of high symmetry is beneficial leading to trigonal lattices in 2-D and face centered cubic lattices in 3-D.

Electromagnetic fields can be divided into two polarizations by symmetry: transverse magnetic (TM), where there is no magnetic field in the direction of propagation; and transverse electric (TE), where there is no electric field in the direction of propagation. It is possible for there to exist TM only or TE only band gaps simultaneously but not overlapping. A full band gap occurs when the TM and TE band gaps overlap. Consider a 2-D lattice of high dielectric rods placed in a square lattice in air as shown in figure 2-7. This structure has a complete band

gap for TM modes as seen in figure 2-7 for the blue TM mode lines, but not for TE modes of red lines. A mode lowers its frequency by concentrating its displacement energy in high-dielectric regions due to the continuity constraint on the displacement vector at the interfaces.

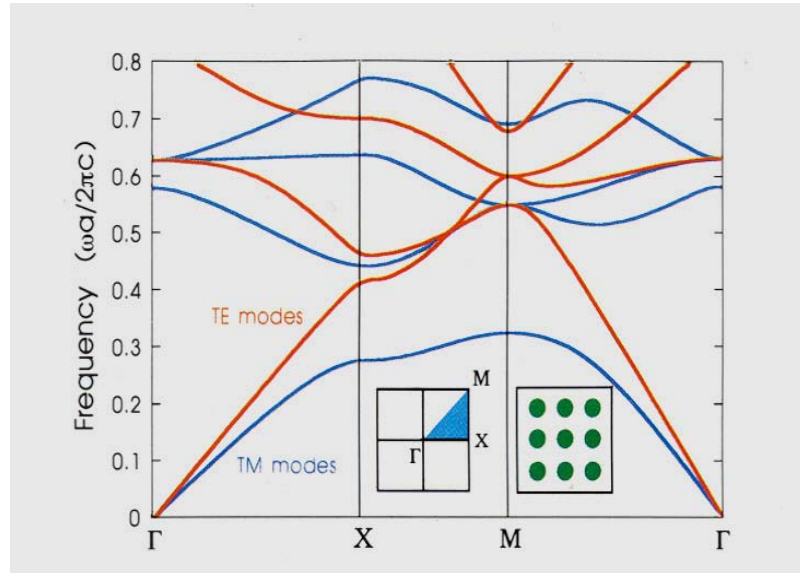


Figure 2-7 Photonic band diagram for a square lattice of high dielectric rods in a low dielectric matrix [87]

This leads to the splitting of bands because the next band may lie in the low-dielectric regions that are typically regions comprised of air, referred to as air bands, having a higher frequency. This leads to defining a fill factor, which is the fraction of total electrical energy located inside the high-dielectric regions of a structure. The lowest TM mode band in the rod structure can be localized within the rods, leading to a band of high fill factor next to a higher frequency band located in the air region of low fill factor. This large difference in fill factor is indicative of the existence of a band gap. The TE modes must travel through the air regions to connecting rods; thus, the TE mode bands will all have low fill factors for all bands, resulting in no band gap. For a square lattice of dielectric veins, as shown in figure 2-8, the TE modes have a band gap, but there is no TM mode band gap. The continuous transverse high dielectric region allows for the lowest TE band to travel in the high dielectric region leading to a large fill factor.

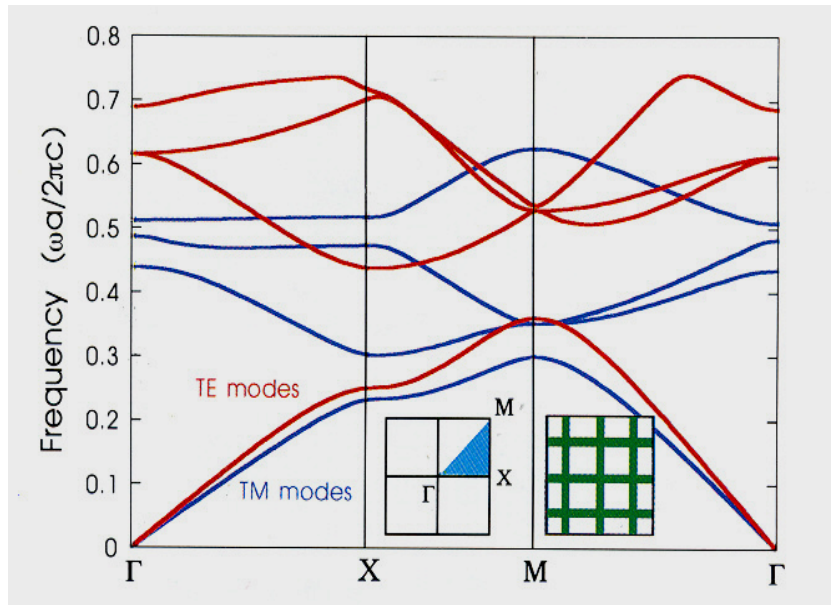


Figure 2-8 Photonic band diagram for interconnected veins of high dielectric material in a low dielectric matrix [87]

The next TE band, which must be orthogonal to the previous band, is forced to pass through the air region leading to a low fill factor. Thus there will be a large fill factor contrast and a TE band gap. For the TM modes the lowest band is able to exist in the high-dielectric regions of the veins at the intersection of the veins, leading to a high fill factor. The next TM mode is able to exist in the high-dielectric horizontal veins connecting the structure also leading to a high fill factor; thus there will be no fill factor contrast and no band gap. For a structure to have a complete band gap, where the band gap for TM and TE modes overlap, it will have to have connectivity of veins for a TE mode gap along with isolated columns for a TM mode gap. This can be achieved through a triangular or honeycomb lattice of low-dielectric material rods contained in a high-dielectric material. This structure provides TE and TM band gaps through interconnected veins between rods for TE band gaps and semi-isolated columns at the intersection of any three rods or at the centers of the honeycomb for TM band gaps [87].

### 2.3.2 Photonic Band Gap Modeling

Due to the high complexity of two- and three- dimensional photonic crystals, theoretical analysis is done by a computational technique. A frequency-domain computational technique can be used to determine the band diagrams of a structure leading to device design and interpretation of measurements. The MIT Photonic-Bands (MPB) package, developed by Steven G. Johnson along with the Joannopoulos Ab Initio Physics group at MIT, is a free program for computing the band structures and electromagnetic modes of periodic dielectric structures [88]. The MPB program uses frequency-domain for direct computation of the eigenstates and eigenvalues of Maxwell's equations using a planewave basis [86].

In order to model a ZnS:ErF<sub>3</sub> half stack device of photonic crystal structure several parameters need to be considered. The main parameters necessary for modeling are the structure parameters of lattice constant (a), column radius (r) and lattice configuration and the dielectric constants of the media. Since high symmetry leads to greater band gaps, a hexagonal honeycomb symmetry is chosen due to its high level of symmetry. The rule of thumb that wavelength divided by refractive index equals lattice constant can also be used as a first-hand estimation. Therefore, to achieve a photonic band gap for 1550 nm wavelength light emitted from ZnS:ErF<sub>3</sub> with refractive index of 2.33, values of 660 nm and 264 nm for lattice spacing and column radius respectively will be used. Calculating the exact band gap for this system using MPB based on the dielectric constant mismatch of the materials used and using a hexagonal array pattern of holes has been done. Figure 2-9 shows the MPB-calculated band diagram using a honeycomb array of cylinders of high dielectric constant in a matrix of low-dielectric material with a dielectric mismatch of 11.4, determined for a wavelength of 1550 nanometers with cylinders of radius equal to 0.14 times the lattice spacing of the pattern (i.e.  $r/a = 0.14$ ).

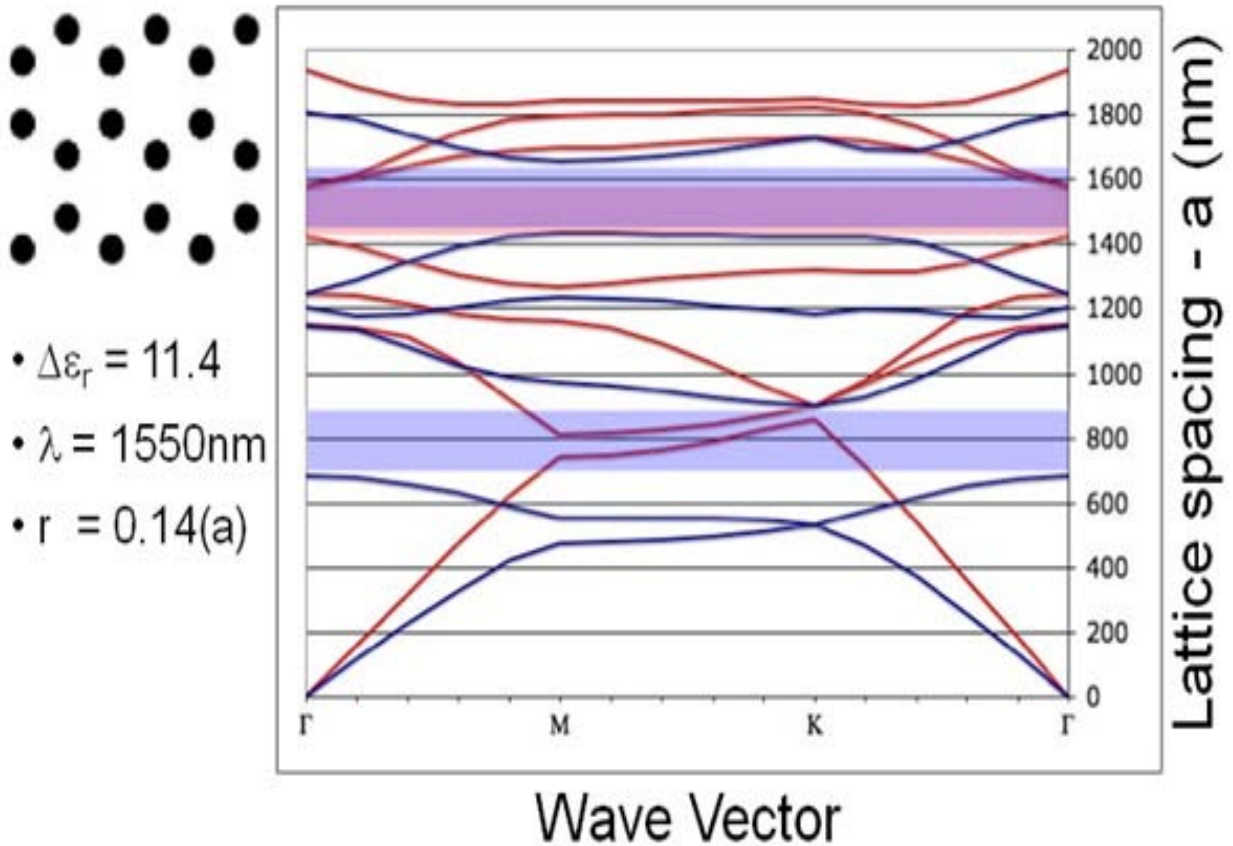


Figure 2-9 Photonic band diagram calculated by MPB.

The MPB program separates light into its components of transverse electric (TE) and transverse magnetic (TM) modes of propagation. In figure 2-9 the blue lines correspond to TM modes and the red lines are TE propagation modes. Band gaps of only one mode are seen in the blue shaded region centered about 800 nanometer lattice spacing which is a TM-only band gap. In figure 2-9 around a lattice spacing of 1500 nanometers, a TE gap (shaded red) overlaps a TM gap (shaded blue) and in this instance there is a complete band gap for all modes of light across all wave vectors. Mark Allen has developed an add-on application to MPB that enables the calculation of band gaps dependent upon the radius of the cylinders with respect to the lattice spacing [89].

Figure 2-10 demonstrates a photonic crystal band gap map using the same honeycomb geometry, wavelength and dielectric mismatch as that for the band diagram shown in figure 2-9.

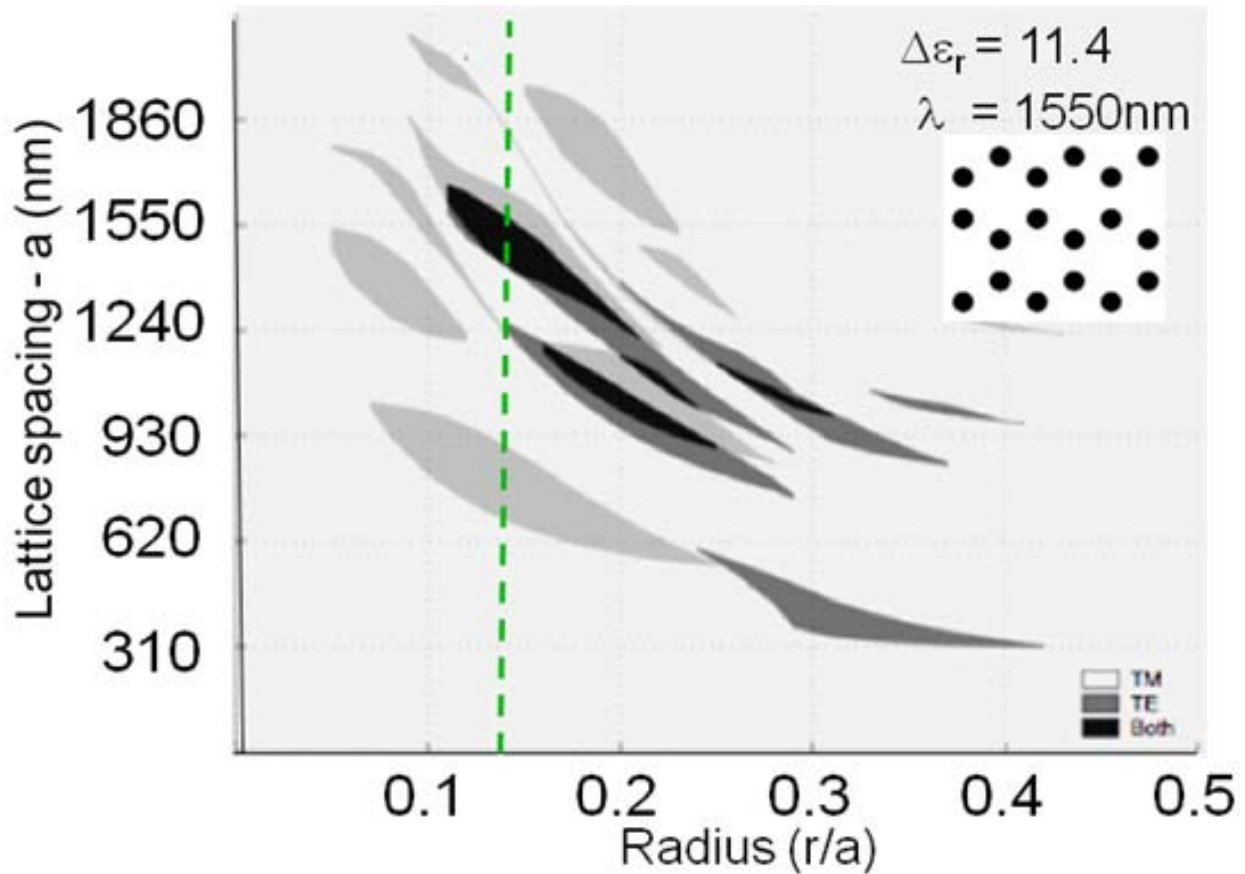


Figure 2-10 Photonic band gap map for honeycomb structure

The green dotted line, at  $r/a = 0.14$ , in figure 2-10 corresponds to the band diagram of figure 2-9.

Gap maps are useful to determine the location of the largest photonic band gap dependent upon the dimensions of lattice spacing and radius of the structure of interest with respect to wavelength and dielectric contrast. In figure 2-10 the light gray shaded regions correspond to TM band gaps and dark gray corresponds to TE band gaps. The black regions are overlapping TE and TM regions which correspond to complete band gaps over all wave vectors and light propagation modes.

### 2.3.3 Off-Axis Propagation

The band gap that is achieved in on-axis propagation tends to decrease as light propagates in increasingly off-axis directions [90]. The reason the dispersion curve of the lowest band for

TE and TM diverges from the origin is that when the electromagnetic field is polarized perpendicularly to the dielectric medium the displacement vector must be continuous, imposing a uniform distribution of this vector and leading to a higher electromagnetic energy contained in the structure. In the case of short-wavelength radiation in the off-axis orientation independent of polarization the electromagnetic energy tends to concentrate within the high-dielectric regions, which tend to act as planar waveguides. The periodic coupling in on-axis propagation due to the periodic dielectric medium disappears as off-axis propagation waves become evanescent in the low dielectric regions. Therefore with no coupling in on-axis propagation, the photonic band gap tends to disappear as propagation tilts more and more off-axis. This is not deleterious since the elimination of light propagation modes directed out of the plane would be undesirable.

#### **2.3.4 Simultaneous Inhibition and Redistribution of Light Emission**

Inhibition of propagating modes of light by a photonic crystal structure with a photonic band gap has been reported [91, 92]. Redistribution of the inhibited light into different modes of light propagation has been less studied. Fujita et al. have reported on light redistribution [93]. Fujita proposed that since the overall spontaneous emission rate is expected to decrease as a result of the photonic band gap effect, the emission rate for directions in which the photonic band gap does not appear will increase by a redistribution of the energy. In other words, in devices with large refractive index contrast to air where light is confined to slab propagation, an incorporated photonic crystal will reduce the in-slab emission rate while simultaneously enhancing the vertical out-of-slab emission rate. Fujita reports that for a single quantum-well device inserted into the middle of a photonic crystal slab, the spontaneous emission rate was reduced by a factor of 5 with emission efficiency normal to the slab face increased by a factor of about 4, with the difference attributed to non-radiative relaxation losses [93]. To summarize Fujita's report: the overall rate of spontaneous emission comprises the rate of emission in the

slab, which is suppressed by the photonic crystal, and the rate of vertical emissions which remains unchanged, but due to the demonstration of longer emissions lifetimes for photonic crystal devices the efficiency of the vertical emissions is increased. Therefore, the claim for simultaneous inhibition and redistribution of spontaneous emission is made.

A theory offered by Liu et al. is based on the conservation of density of states; a photonic crystal causes the depletion of states resulting in the enhancement of other states [94]. Noda and Fujita reported on the use of a photonic crystal structure to inhibit confined modes of light propagation in light emitting diodes (LEDs) in order to increase light-extraction efficiency [95].

Figure 2-11 shows three LED device structures which lead to increased extraction efficiency.

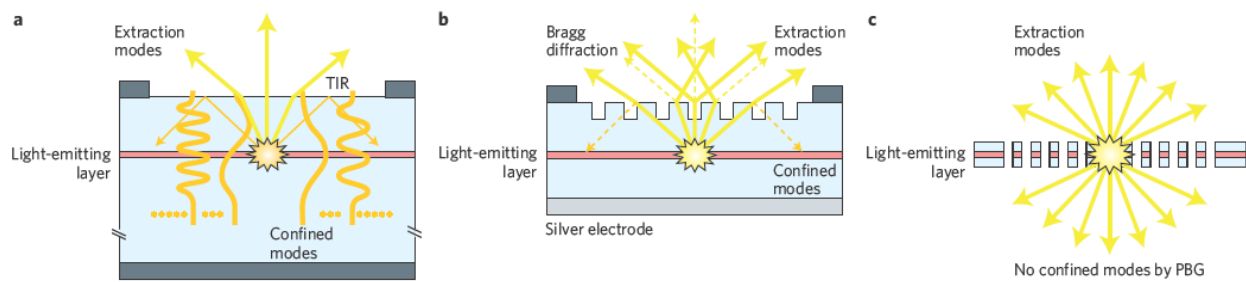


Figure 2-11 Cross-sectional schematic of LED structures illustrating confining and extracting modes of light propagation [95].

In Figure 2-11, the left most device is a planar-surface LED with outcoupling limited by total internal reflection or confined modes of light propagation. The middle device has a photonic crystal structure to control light at the surface which reduces the confined modes. The right most device consists of the photonic crystal structure incorporated into the light-emitting layer inhibiting confined modes and maximizing outcoupling modes. The analysis of simultaneous inhibition and redistribution of light emission from the photonic crystal structure reinforces the conclusion that photonic crystals can be used to increase the light-extraction efficiency of light emitting devices.

## 2.4 Light Scattering

One key concern to the investigation of light emissions from ACTFEL devices is the issue of light scattering. Generally, any kind of macroscopic and/or microscopic fluctuations of spatial and/or temporal properties of a given medium will cause the scattering of an incident light beam [96]. Scattering such as from rough surfaces can significantly decrease light guiding leading to increased optical outcoupling; however, scattered light makes displays diffusely reflective which reduces contrast and rough surfaces may adversely affect electrical properties and device stability [97]. Two main forms of light scattering are Rayleigh and Mie scattering. Rayleigh scattering refers to scattering from particles of significantly less size than the wavelength of the scattered light, while Mie scattering is more general and can be used for all particle sizes.

### 2.4.1 Light Reflection

Simplistically, light reflection off a surface can be characterized as either diffuse or specular reflection. Figure 2-12 schematically illustrates diffuse versus specular reflection.

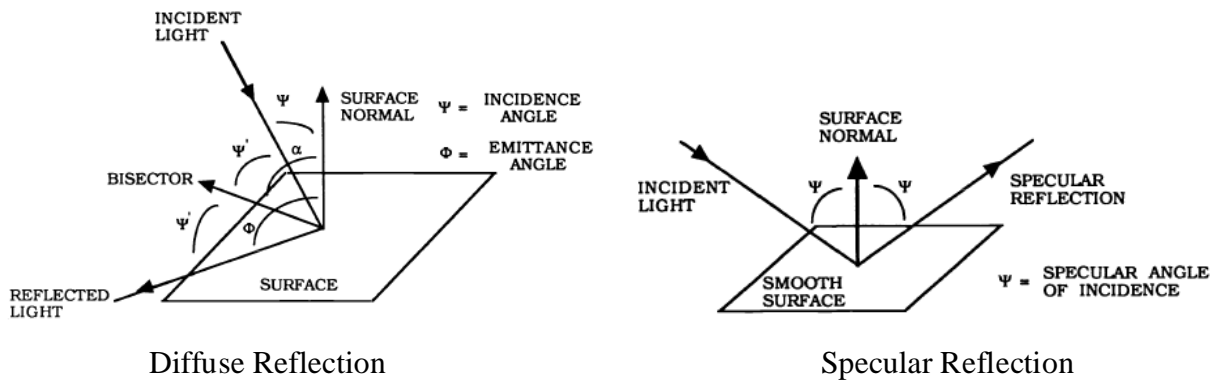


Figure 2-12 Diffuse versus specular reflection [98]

Specular reflection occurs on smooth surfaces where the angle of incidence of incoming light is equal to the exit angle of the reflected light. Diffuse reflection occurs when the surface is rough

and reflected light leaves the surface at various angles compared with the incident angle. The radiance distribution for diffuse reflection follows Lambert's law, shown in equation 2.11 [98].

$$I = I_0 \rho \cos \theta d\Omega \quad (2.11)$$

In equation 2.11,  $I_0$  is the incident radiance,  $\rho$  is a scaling factor having a range from 0 to 1,  $\theta$  is the incidence angle and  $d\Omega$  is the solid angle.

### 2.4.2 Rayleigh and Mie Scattering

Lord Rayleigh was one of the first pioneers in the study of light scattering [99]. He theoretically investigated the scattering caused by a dielectric sphere of a size much smaller than the light wavelength and derived a famous formula showing the fourth-power inverse proportionality between the scattering intensity and the light wavelength [96]. Light scattering behaviors can be roughly classified into regimes determined by the wavelength dependence with respect to the scattering cross section. The scattering cross section ( $\delta$ ) is equivalent to the wavelength of light in the surrounding medium ( $\lambda$ ) divided by the diameter of the scattering center ( $d$ ), as shown in equation 2.12 [99].

$$\delta = \lambda/d \quad (2.12)$$

Rayleigh scattering is the scattering regime under the condition  $\delta > 10$ . When the condition of  $10^{-2} < \delta < 10$  occurs, the scattering regime which is entered is termed Mie Scattering, characterized by a wavelength-dependent power factor varying within a range of roughly -4 to 2 proportionally to the scattered intensity,  $I^n$  where  $-4 < n < 2$  [96].

## 2.5 Lithography

The term lithography when speaking of electronic materials processing is typically used to mean the exposure and development of a pattern in a radiation-sensitive film called a resist which is followed by a transfer technique to reproduce the pattern in the underlying material. This section will provide a background for understanding this process.

### 2.5.1 Optical Lithography

The process of lithography begins with a resist which is sensitive to the radiation that will be used to expose the resist. The resist is usually a polymer thin film which is spun-coated onto the substrate. Polymethylmethacrylate (PMMA) is widely used as the polymer of choice for the resist layer. PMMA is typically a positive resist, meaning that areas of the PMMA which have been exposed to radiation are removed by developing with a solvent [100]. There also exist negative resists such that only the areas of the resist which have been exposed to radiation remain after developing with a solvent which removes the resist that remained unexposed. Positive resists typically have a greater resolution than negative resists.

Optical Lithography utilizes resists which are sensitive to light. The resist is exposed to light through a mask containing the desired pattern. The resolution limit for optical lithography is in part determined by the wavelength of the light used for exposure, with shorter wavelengths leading to smaller structures. In most optical lithography systems the optics are sufficiently well made that the resolution is limited by the ability to collect and reimage the light. This limit is referred to as Rayleigh's criterion, as expressed in equation 2.13 [101],

$$W_{\min} = k \lambda / \text{NA} \quad (2.13)$$

where  $k$  is a constant which depends on the sensitivity of the resist and is usually on the order of 0.75;  $\lambda$  is the wavelength of the light; and NA is the numerical aperture which pertains to the amount of light which can be collected from that which is lost due to diffraction of the light coming through the mask (NA typically ranges from 0.16-0.5). As an example, in a system with an NA of 0.4, a  $k$  value of 0.75 and a wavelength of 436 nanometers, one can image lines as small as 800 nanometers [101]. With the combination of deep UV excimer sources and phase-shifted masks, resolutions may be extended to below 250 nanometers.

### 2.5.2 Electron Beam Lithography with a Scanning Electron Microscope

Scanning electron microscopes (SEMs) [102] were developed to escape the limitations of light microscopes, which were limited to magnifications of just 500-1000X due to the nature of light. SEMs have a better resolution and depth of field than optical microscopes and can provide compositional analysis of the specimen. Disadvantages of the SEM include that the specimen must be under a vacuum and that the specimen must be conductive which may require coatings which may introduce artifacts. The basic operation of an SEM involves the production of electrons which are accelerated towards the specimen while being confined and focused by apertures and electromagnetic lenses. Once the beam impinges on the surface of the specimen, electron interactions occur with the sample resulting in electrons that can be detected to reveal topographic and compositional information about the sample [102].

One of the methods used to generate the electrons for the electron beam of the SEM is thermionic emission from a tungsten filament. At high enough temperatures induced by resistive heating of the filament, electrons in the tungsten attain energies higher than the work function of the tungsten, enabling those electrons to escape from the tungsten. Voltage is used to accelerate those electrons down the column of the SEM. The tungsten wire filament is about 100 microns in diameter and is bent into a “v” shape resulting in a tip with an emission area of about 100 by 150  $\mu\text{m}$ . The process of field emission is another method used to generate electrons. In field emission the cathode has the form of a rod with a very sharp tip, with a tip radius less than or equal to 100 nanometers. When this cathode is held at a negative potential with respect to the anode the electric field at the tip of the cathode becomes extremely large. This electric field is large enough to cause electrons to tunnel through the energy barrier and leave the cathode without the need for thermal energy. This allows for a cathode current density of between 1000 and  $10^6 \text{ A/cm}^2$ , which leads to an effective brightness many hundreds of times larger than that of

a thermionic source operating at the same voltage [102]. The SEM used in this research for electron beam lithography is a field emission SEM.

Electron beam interactions with the specimen surface are of primary importance. When electrons impinge on the surface of a material they interact with that material in a region known as the electron interaction volume. Figure 2-13 shows simulated electron trajectories into a material showing an interaction volume as well as the type of signal generated in the material [103].

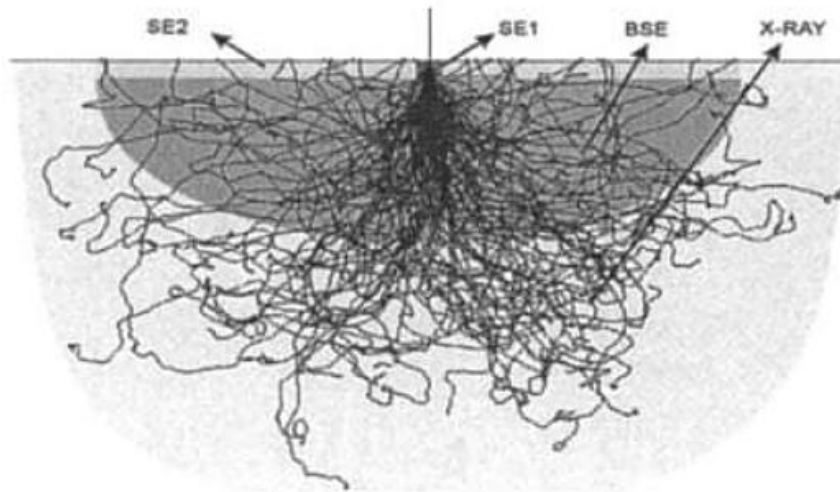


Figure 2-13 Electron beam interaction volume showing signals (see text) generated [103].

In figure 2-13 there are four signals identified: SE1, SE2, BSE and X-Ray which represent secondary electrons 1 and 2, backscattered electrons and fluorescent X-Rays. Secondary electrons are produced by inelastic scattering events between the primary beam electrons and electrons in outer orbitals of the atoms of the specimen, which are thus ejected. The very low energies of these ejected electrons, below 50 eV, means that these electrons can only escape from a sample within a few nanometers of the surface resulting in the fact that secondary electrons provide the primary signal for surface imaging. Backscattered electrons arise from the inelastic scattering of the primary electron beam resulting in higher energy electrons emitted

from the sample to depths on the order of less than a micron. Backscattered electrons are highly dependent upon the atomic number of the atoms with which the primary beam interacts; thus, they are primarily used for elemental contrast of the specimen. X-rays which are characteristic of the atoms in which they were produced are created by the relaxation of outer shell electrons into empty inner shell quantum states created by interaction of the atom with the primary electron beam. These X-rays are used for elemental analysis of the specimen. Secondary electrons are formed from the backscattered electrons away from the primary electron beam impingement spot. The size of the interaction volume is increased with increasing beam energy.

### **2.5.3 Electron Beam Lithography**

Electron beam lithography enables the direct writing of patterns into the resist layer without the need for a mask. Electron beam lithography uses an electron beam as the radiation used to expose the resist. Electron beams can be controlled such that resolutions on the order of tens of nanometers can be achieved. The electron beam spot size is typically  $\frac{1}{2}$  to  $\frac{1}{5}$  of the minimum feature size to improve edge resolution [101].

The resolution of electron beam lithography even by the mid-1970s demonstrated the capability to write lines and spaces less than 10 nanometers in width, well below the best resolutions of any optical systems of the day [104]. The cost of electron beam lithography systems around the mid 1990s is about \$5M which is much higher than that for optical systems, although excimer stepper systems for optical lithography can reach as much as \$3M [101]. Another major concern for electron beam lithographic systems is throughput. Electron beam lithography is approximately one order of magnitude slower than optical lithography [105]. Therefore, due to the higher resolution of electron beam lithography, it is very useful for mask making for optical systems as well as for prototype production and research concerns when throughput is not a major issue.

The most commonly used resist layer is PMMA which requires an electron beam dose ranging from 50 to 500  $\mu\text{C}/\text{cm}^2$  for exposure. Figure 2-14 shows simulated electron trajectories for an electron beam with accelerating voltage of 25keV with a 100 nanometer spot size impinging on a 500 nanometer thick PMMA film sitting on a Si wafer [106].

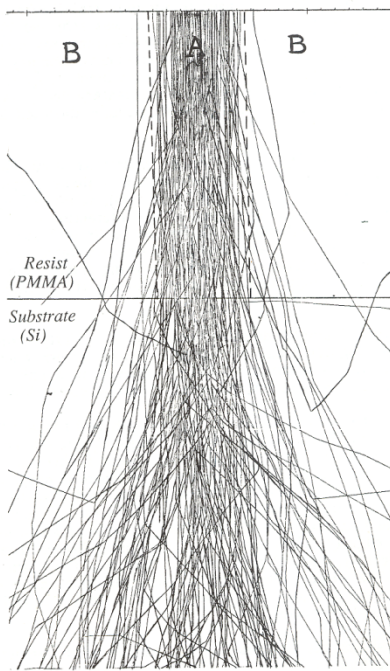


Figure 2-14 Simulated electron trajectories in PMMA for an electron beam of 25keV acceleration voltage and a spot size of 100 nm [106]

Figure 2-14 demonstrates the dynamics of the interaction of the electron beam with the PMMA showing electrons mainly scattered at low angles through the PMMA and scattered at larger angles once in the silicon substrate. Two of the key parameters which affect the electron beam interaction with PMMA are the spot size and the beam energy. After exposure, the PMMA pattern is developed in a 1 to 3 solution of methyl-isobutyl-ketone in isopropanol for about 75 seconds [107]. Lithography is generally followed by a process which transfers the pattern from the resist to the substrate, either by etching, growth of a material in the interstices of the resist, or doping [108].

#### 2.5.4 Nanometer Pattern Generation System

The Nanometer Pattern Generation System (NPGS) created by J.C. Nability in 1988 enables the control of an SEM for patterned exposures of the electron beam onto a surface. There are two types of variables, the first being those controlled by the SEM and the second being those controlled by NPGS. SEM controlled variables include the electron beam spot size, the beam current, the accelerating voltage and the aperture size. Some of the effects of these variables were discussed in section 2.5.2. NPGS controlled parameters include control of the primary beam, the magnification of the SEM, center-to-center distance and line spacing of the exposure, the dwell time and dose type of either area, line or point. The magnification must be set low enough so that the writing pattern fits into the field of view. The best results are obtained when the dimension of the written pattern is about 75% of the field of view dependent on the magnification. If the pattern is too large or the magnification too low, a greater amount of beam deflection is necessary to deflect the electron beam to the extremities of the pattern. The greater the deflection, the less focused the electron beam, leading to possible distortions at the edges of the pattern. The center-to-center distance is the distance between exposure points along a line or arc of exposure. The line spacing is the distance between adjacent lines of the beam when filling wide lines, arcs or filled polygons. The center-to-center spacing and line spacing are typically set to equal one another; they determine the desired radius of curvature of a feature. For example, if a 2 micron wide square is to be written using a 50 nanometer center-to-center distance and line spacing then the radii of the corners of the square will be on the order of 50 nanometers. The dwell time sets the exposure time for each step of pattern writing. The three types of dose parameter are area, line and point. Area doses are used for patterns requiring multiple passes of the beam such as filled polygons. The units of area dose are  $\mu\text{C}/\text{cm}^2$  and are determined by equation 2.14.

$$\text{area dose} = [(\text{beam current}) * (\text{dwell time})] / [(\text{center-to-center}) * (\text{line spacing})] \quad (2.14)$$

Line doses (units of  $\mu\text{C}/\text{cm}$ ) are used for single passes of the beam and are calculated based on equation 2.14 without the line spacing term. Point doses (units of  $\text{fC}$ ) are used for structures that can be written using single exposure points of the electron beam and are calculated simply by the beam current times the dwell time.

### 2.5.5 Etching

Once the resist has been exposed and developed the etching process transfers the pattern from the resist layer to the underlying layer. The primary figures of merit for etching include etch rate (with units of thickness per unit time), selectivity (the ratio of etch rates for various materials including the resist layer), and undercut (the lateral extent of the etch to the layer under the mask of the resist) [101]. Etch rates on the order of tens to hundreds of nanometers per minute are desirable; too high a rate can hinder control. Etches are done by a physical or chemical attack or a combination of the two. The two basic types of etching are referred to as wet etching and dry etching.

Wet etching is a purely chemical process. Serious drawbacks of wet etching include a lack of anisotropy in etch rate, poor process control and excessive particle contamination. However, wet etching can be highly selective and often does not damage the substrate [101]. Wet etching consists of three basic processes: delivery of etchant to surface, surface reaction producing soluble byproducts and the removal of the byproducts. One of the most common wet etch processes is the etching of silicon dioxide ( $\text{SiO}_2$ ) in dilute solutions of hydrofluoric acid (HF) [109]. A 6:1 water-to-HF solution will etch thermal  $\text{SiO}_2$  at about 120 nanometers per minute. The selectivity of an etchant refers to the difference in rate of etching between different media being etched by the etchant. HF solutions are extremely selective of oxide over silicon

with selectivities commonly better than 100:1 [110]. Wet etching is limited due to undercutting to about 3  $\mu\text{m}$  feature sizes in 1  $\mu\text{m}$  thick films [111].

Dry etching consists of plasmas which are generated in order to either physically sputter or chemically erode away the material, or the two processes may be used together. In general, dry etching is preferred to wet etching for several reasons: dry etching is easier to automate, is more anisotropic in pattern transfer, can etch smaller features due to the absence of surface tension or wettability effects, and should reduce the amount of waste material [112]. Sputter etching incorporates high-energy ions striking a surface which are sensitive to the strength of the atomic bonding forces and not to the composition, leading to a low selectivity in the removal of surface atoms [111]. Chemical etching refers to when the gas phase reacts with the surface creating volatile or gasified products which are removed from the surface [111]. Chemical etching is very selective due to its sensitivities to slight changes in bond energies of atoms; however, etching may be isotropic leading to undercutting that prohibits high resolution [111]. When physical sputtering, which creates defects, is combined with chemical etching, enhanced by the defects from the physical sputtering, a much more anisotropic etch can be achieved. Electron Cyclotron Resonance Reactive Ion Etching (ECRRIE) is an example of a technique which utilizes both chemical and physical sputtering. The system operates by exposing a gas at low pressure to an RF bias generating a plasma which is confined by magnetic fields and force electrons to travel in a cyclotron pattern, increasing the density of ions. The main parameters which affect the etch rate are gas species, pressure, RF and ECR power. Figure 2-15 illustrates the differences in etch rates achieved in multiple materials when the RF power is adjusted [113]. Typical ion fluencies of  $10^{15}$  ions/cm<sup>2</sup> are delivered at energies of 300 to 700 eV to the surface in RIE [101]. At these levels substrate damage becomes an issue [114].

## 2.6 ACTFELD and Photonic Crystal Characterization

### 2.6.1 Optical Characterization

Photometry is the science of the measurement of light in terms of perceived brightness with respect to the spectral response of the human eye [115]. Radiometry is the measurement of light in terms of quantifying absolute optical output and is not limited to the visible region of the electromagnetic spectrum as is photometry [115]. The radiometric unit used to measure photon flux density or irradiance is  $\text{W}/\text{cm}^2\text{-nm}$ . Since photometry takes into account the response of the human eye, a device that emits two wavelengths of light at the same radiometric output may have very different photometric values, which have units of candelas per meter squared.

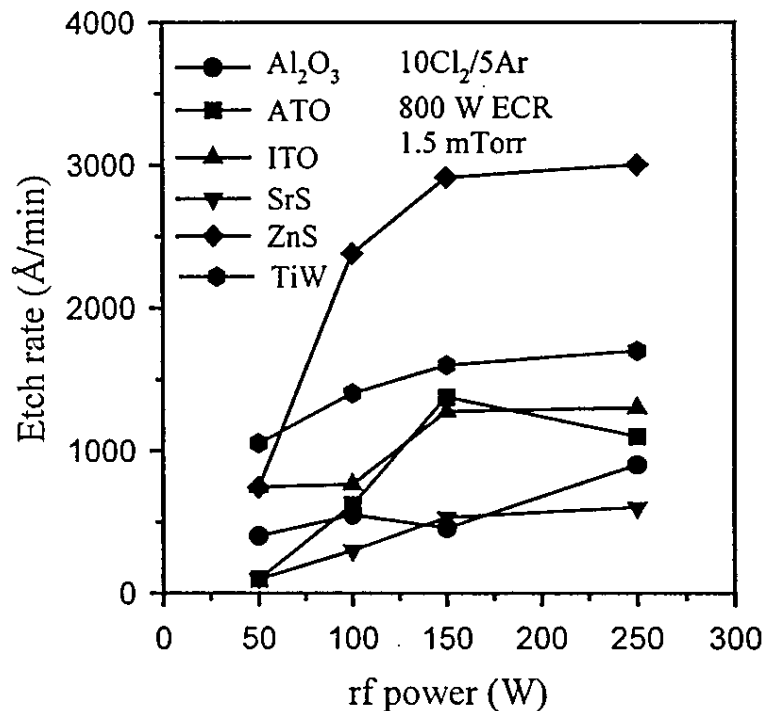


Figure 2-15 Etch rates of materials with respect to RF power in an ECRRIE plasma etch system [113]

The simplest and most common measurement technique for the radiometric output of ACTFEL devices is the measurement of EL light intensity as a function of applied voltage or brightness versus voltage (B-V) curve. Typically an AC voltage source using a trapezoidal pulse and

frequencies of either 60 Hz or 2.5 kHz are used to drive the devices. A spectrometer is used to measure the brightness data. A typical B-V curve is shown in figure 2-16.

A critical voltage value known as the threshold voltage of luminescence ( $V_{th}$ ) is determined by taking the slope of the near vertical section of the curve and intersecting that slope with the voltage axis, also presented in figure 2-16. This voltage signifies the onset of the electric field necessary for electron injection and acceleration to energies capable of exciting luminescent centers in the phosphor. There is typically a linear increase in brightness with voltage until the device saturates causing a flat line of the curve until the device dies by undergoing permanent dielectric breakdown of the phosphor or dielectric layers. Brightness levels at 20 volts ( $B_{20}$ ) and 40 volts ( $B_{40}$ ) above threshold voltage are the values most commonly used for comparing different devices. In order to compare between different devices it is most beneficial for the phosphor layer and dielectric layer thicknesses of the devices to be nearly identical and to be driven at the same voltage. Differences in thicknesses of devices cause shifts in the threshold voltages and brightness between devices.

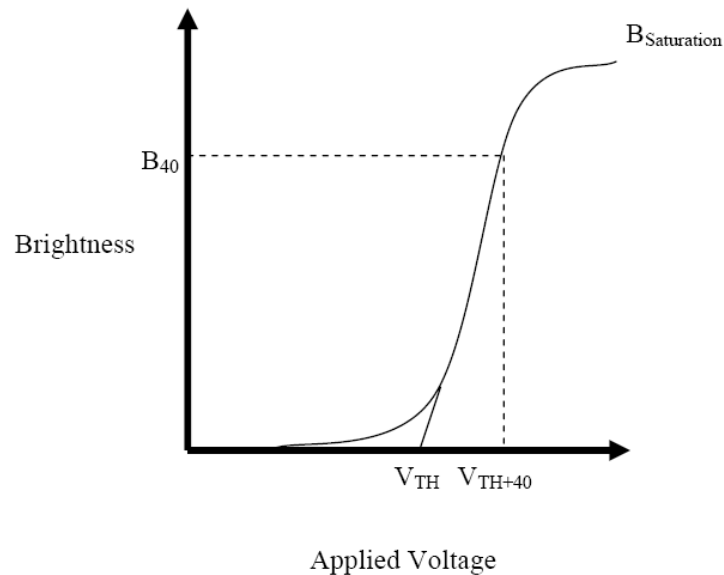


Figure 2-16 Typical brightness versus voltage data for an ACTFEL device

## 2.6.2 Electrical Characterization

The most common waveform used for testing ACTFEL devices is a bipolar trapezoidal wave as shown in figure 2-17. The pulses have a rise and fall time of  $\sim 5 \mu\text{s}$ , a  $30 \mu\text{s}$  plateau and a frequency between 60 Hz and 2.5 kHz.

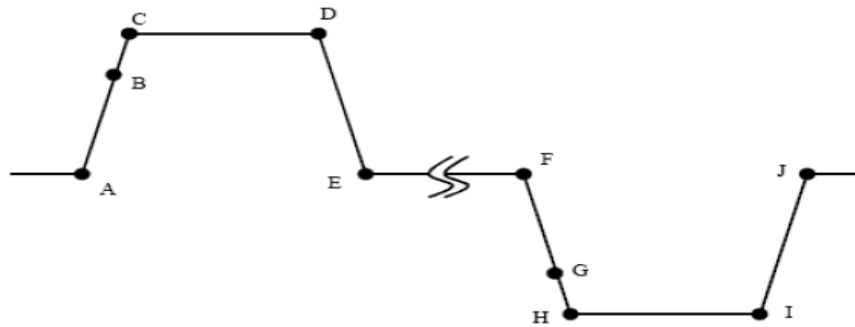


Figure 2-17 Trapezoidal voltage waveform diagram used for ACTFEL device operation [46].

In order to obtain electrical data from a device being driven under this waveform, a Sawyer-Tower circuit arrangement is typically used and is shown in figure 2-18 [116].

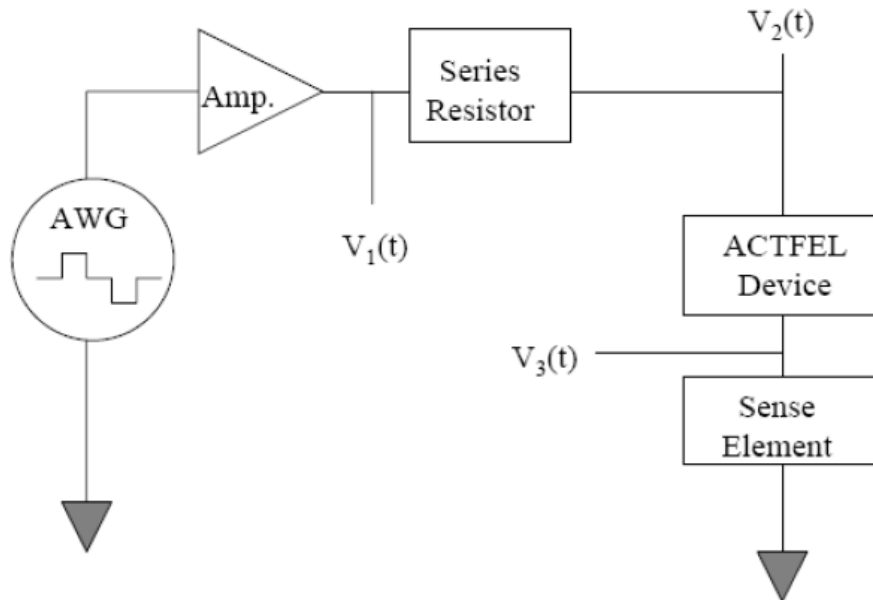


Figure 2-18 Schematic of a Sawyer-Tower bridge circuit [116].

A series resistor, the ACTFEL device and a sense element arranged in series constitute the circuit. The resistor simply limits current to the ACTFEL device in the event of dielectric

breakdown. The sensing element can be either a resistor used for the measurement of external current across the device or a capacitor used for the measurement of internal charge across the device. The voltage drop across the ACTFEL device is found from  $V_2$  and  $V_3$  in figure 2-18 as determined in equation 2.15.

$$V_{EL}(t) = V_2(t) - V_3(t) \quad (2.15)$$

When using a capacitor as the sense element, the external charge is determined from equation 2.16, where  $C_s$  is the sense element capacitance.

$$Q_{ext}(t) = C_s V_3(t) \quad (2.16)$$

When using a sense resistor, the current passing through the device is determined by equation 2.17.

$$i(t) = [V_1(t) - V_2(t)] / R_{series} \quad (2.17)$$

The resulting external charge is found by integrating this current over time as shown in equation 2.18.

$$Q_{ext}(t) = \int i(t) dt \text{ from } 0 \rightarrow t \quad (2.18)$$

The primary characteristics of the electric response of an ACTFEL device are determined from a graph of the charge versus the voltage, or a Q-V plot, of the device. The measurements needed to create a Q-V plot are the charge stored across the two external terminals of the capacitive ACTFEL device and the voltage applied across those terminals as can be determined from the Sawyer-Tower circuit and corresponding equations. At voltages below the threshold voltage the plot is a straight line with a slope equal to the total capacitance of the device. The Q-V plot exhibits a hysteresis loop response when the device is driven at voltages above the threshold voltage; this is due to the conduction charge that flows through the phosphor. Figure 2-19 shows a typical Q-V plot using labels (A-J) corresponding to those points of figure 2-17. In figure 2-19  $Q_{leak}$ ,  $Q_{pol}$ ,  $V_{to}$ ,  $V_{th}$ ,  $Q_{cond}$  and  $Q_{relax}$  stand for leakage charge, polarization charge,

electrical turn-on voltage, optical threshold voltage, conduction charge and relaxation charge, respectively. Points B and G correspond to the voltage values where the conduction charge becomes significant. Relaxation charge occurs when the applied voltage reaches a maximum value and reflects current which flows during the plateau of the voltage pulse (C-D in figure 2-17). At constant applied voltage the conduction charge creates an opposing electric field that relaxes across the phosphor. From segment D to E the voltage decreases linearly. The leakage charge which occurs when the voltage is zero between pulses of opposite polarity is attributed to electrons escaping from shallow interface states in the ACTFEL device. Above the threshold voltage there is a conduction charge which is responsible for light emission in the device [117].

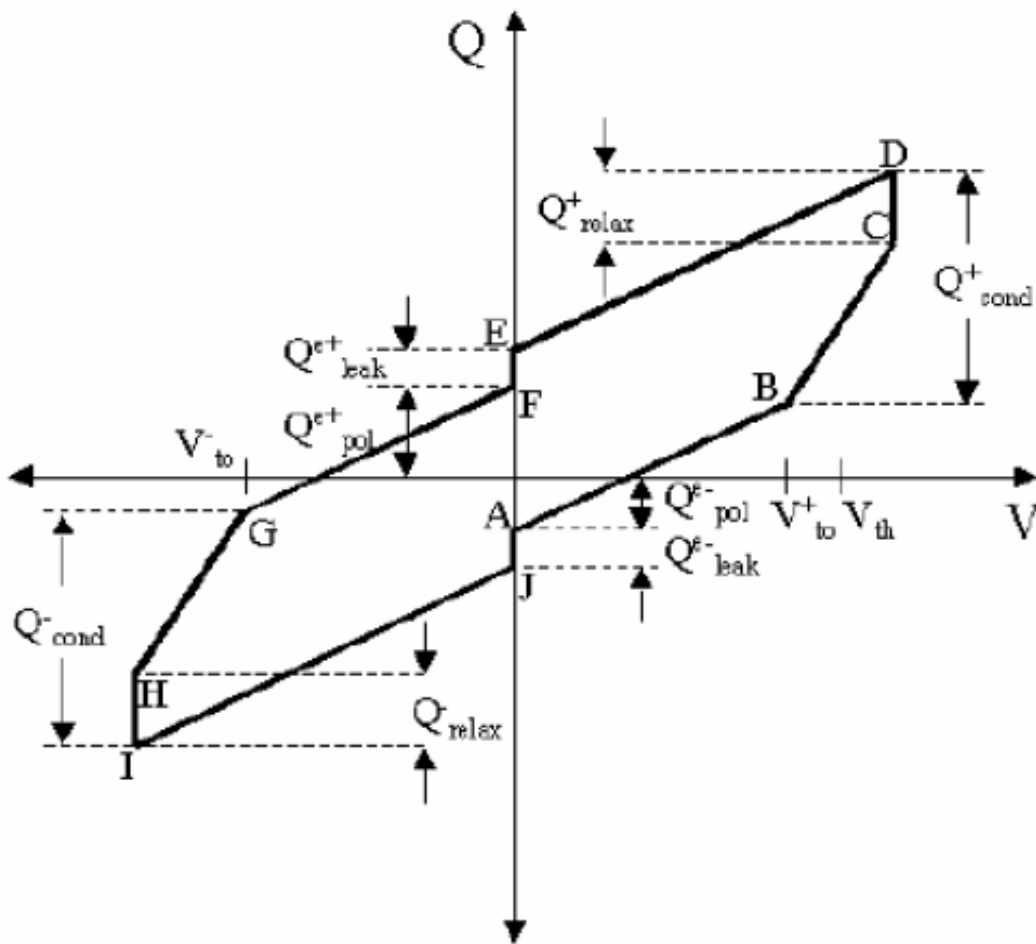


Figure 2-19 Typical Q-V plot for ACTFEL devices driven above the threshold voltage

A number of useful parameters for an ACTFEL device can be obtained from the Q-V data. Primarily the Q-V plot's slope below the threshold voltage is equal to the total capacitance of the device. Above threshold voltages the phosphor acts as a conductor and the slope of the Q-V plot is used to measure the capacitance of the insulating layers. If the device is not completely shorted, the total capacitance will be greater than that of the capacitance of insulating layers due to capacitance from the phosphor layer. Also, if the phosphor has a buildup of space charge, the slope will be larger than the insulator capacitance [80]. Finally, the area inside the Q-V plot is proportional to the input electrical power density delivered per pulse [118].

## CHAPTER 3 EXPERIMENTAL

### 3.1 Introduction

In this chapter, the procedures and conditions used to fabricate and characterize alternating current thin film electroluminescent (ACTFEL) devices with and without photonic crystal structures will be discussed. Methods of fabrication include deposition of thin films by sputtering and evaporation. Structural characterization techniques include atomic force microscopy (AFM), secondary electron microscopy (SEM) and secondary ion mass spectroscopy (SIMS). Finally, optical spectra and intensities were measured using an optical bench with a monochromator and detectors sensitive to visible and near-infrared emission.

### 3.2 ACTFEL Device Fabrication

#### 3.2.1 Substrate Materials and Preparation

Most substrates were supplied by Planar Systems and consisted of Corning 7059 glass, 2 x 2 x 0.04 inches thick, coated with 360 nm of polycrystalline indium-tin oxide (ITO) (90 wt%  $\text{In}_2\text{O}_3$  + 10 wt%  $\text{Sn}_2\text{O}_3$ ) as the transparent conducting electrode and 160 nm of amorphous aluminum-titanium oxide (ATO) ( $\text{Al}_2\text{O}_3/\text{TiO}_2$ ) as the bottom insulating layer. In order to achieve a high-quality, homogeneous insulator, the ATO dielectric layer was deposited by atomic layer deposition (ALD) [119].

Each substrate was dusted using dry nitrogen gas to remove airborne particulate matter. Substrates were cut into two-inch by two-inch squares in order to fit on the substrate platter and were also cleaned at room temperature in a UVOCS, Inc. ultraviolet light ozone cleaner for six minutes in air to remove organic contaminants. To achieve a step for thickness measurements by profilometry, substrates of bare Corning 7059 glass were cut to one inch wide by two inches long and were prepared using the same method as above followed by covering half the slide

lengthwise with Teflon® tape which was then removed after deposition. In addition, bare ITO on glass substrates cut to one inch long by two inches wide were prepared using the same method in order to determine the dielectric constant of the deposited ZnS:ErF<sub>3</sub> layer by means of a capacitance measurement across the ZnS:ErF<sub>3</sub> layer sandwiched between the ITO conducting layer and an aluminum dot contact deposited on top of the ZnS:ErF<sub>3</sub> EL layer.

### **3.2.2 Thin Film Deposition by RF Magnetron Sputtering**

An RF magnetron sputter deposition system was used to deposit ZnS:ErF<sub>3</sub> as the emitting layer of an ACTFEL device. The ZnS:ErF<sub>3</sub> layer was deposited using two sputter targets, one consisting of pure ZnS and the other of ZnS doped with 1.5 mol% ErF<sub>3</sub>. The pure ZnS target was purchased from Morton Thiokol where it was produced by chemical vapor deposition. It was cut with a diamond saw to a 2" diameter by 1/4" thickness for use in an Angstrom Science Onyx 2 magnetron sputtering gun. The doped ZnS was a 2" diameter by 1/4" thick pressed and sintered powder target (Target Materials Inc.) doped with 1.5 mol% of 99.9% pure ErF<sub>3</sub>, and used in an AJA A300 magnetron sputtering gun. The target-to-substrate distance is 10 cm for the pure ZnS target in the Angstrom Science gun and 5 cm for the doped ZnS:ErF<sub>3</sub> target in the AJA gun. The guns are powered by two RF Power Products RF5S radio-frequency controllers combined with an RF Power Products matching network. The duty cycle applied to the gun was varied on both targets independently from 0% to 100% to adjust the composition of the deposited film. The overall applied power was set to 100 watts on both sources; however, the duty cycle for the pure ZnS target was usually set to 100% while the duty cycle for the ZnS:ErF<sub>3</sub> was varied from 30% to 75%. Substrates were held on a sample holder with a capacity for four 2" x 2" substrates or eight 1" x 2" substrates. During deposition, samples were rotated at 11 seconds per revolution using a constant-speed stepping motor. Substrates were heated to temperatures ranging from 75°C to 300°C using carbon cloth heating elements underneath the sample stage. A

thermocouple was used to monitor deposition temperature. The typical deposition temperature was 150°C. Samples were loaded through a load lock which was evacuated to a pressure of 10 mTorr using a Leybold Trivac D65B wet rotary pump. The deposition chamber was evacuated by a Leybold Mag 1600 turbomolecular pump backed by the Leybold Trivac D65B wet rotary roughing pump. The ultimate pressure for the system varies between  $7 \times 10^{-7}$  and  $3 \times 10^{-6}$  Torr depending upon the time allowed to pump down between runs. Ultra high purity (99.9999%) argon was used as the sputtering gas for deposition. The gas was introduced into the chamber using Unit UFC 1100A 20, 50 or 100 standard cubic centimeters per minute (sccm) mass flow controllers on three inlet lines. Argon gas pressure was regulated using the mass flow controllers and a throttle valve installed between the deposition chamber and the turbomolecular pump. A number of gauges on the system allow monitoring of pressure in various regions of the system. Thermocouple gauges are used to monitor pressure in the fore line and load lock. An ionization gauge is used to measure the ultimate pressure in the main chamber and a capacitance manometer monitors the argon gas pressure in the chamber during sputter deposition. Figure 3-1 shows a schematic diagram of the RF magnetron sputter deposition system.

### **3.2.3 Post-Deposition Annealing**

Sputter deposited films were annealed in atmospheric pressure ultra high purity (99.9999%) nitrogen using water-cooled halogen lamps. A schematic of the annealing furnace is shown in Figure 3-2. The halogen lamps are located above and below a quartz tube to provide adequate heating. The quartz tube is loaded from one end, and samples are placed in a graphite oven centered in the quartz tube. The tube is then compression sealed, purged with N<sub>2</sub> and annealed at 425°C for 60 minutes. The nitrogen purge continues during the anneal and post-annealing cool-down period until the sample reaches room temperature. A thermocouple is placed in the graphite enclosure to measure the sample temperature during annealing. The

annealing cycle is controlled by a Micristar controller that controls the ramp-up rate and cool down profiles. Typical ramping time to 425°C was 5 minutes.

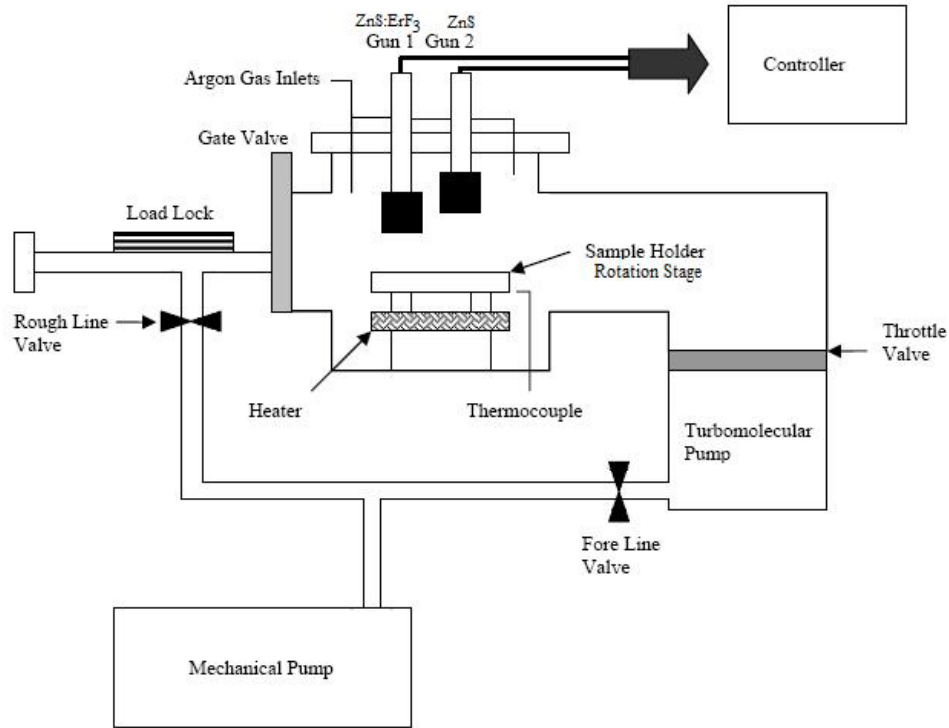


Figure 3-1 Schematic of RF magnetron sputter deposition system used to sputter deposit ZnS:ErF<sub>3</sub> thin EL films.

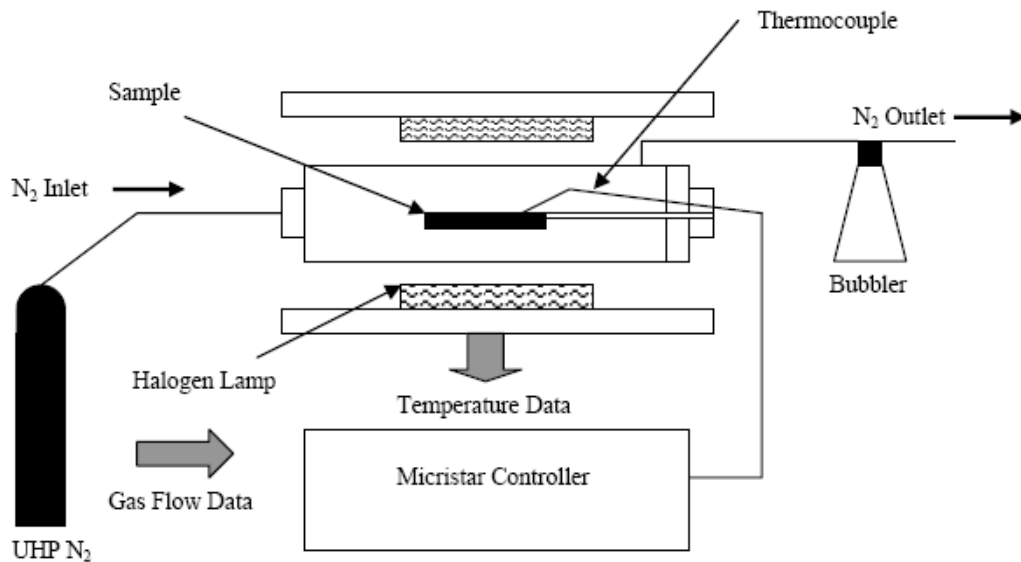


Figure 3-2 Schematic of thermal annealing furnace utilizing lamps as heating elements.

### 3.2.4 Thin Film Deposition by Electron Beam Evaporation

An electron beam deposition system was used for deposition of aluminum thin films for electrical contacts. Figure 3-3 shows a schematic of the system used for the evaporation process.

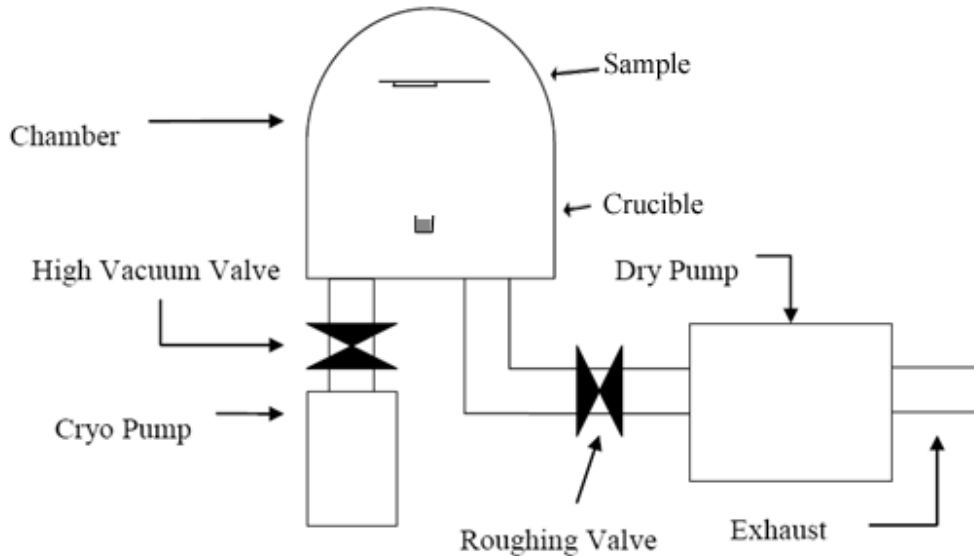


Figure 3-3 Electron beam evaporation system schematic

The dry mechanical pump, a Leybold Dryvac 100P scroll pump, evacuates the chamber to low vacuum in the range of 200-250 millitorr. The cryogenic pump, a CTI Cryogenics Cryo Torr 8, evacuates the chamber to high vacuum, in the range of  $10^{-6}$  Torr. Once the high vacuum is achieved, the electron beam is used to heat up a small amount of aluminum in a carbon crucible until it evaporates and coats everything in the line of sight of the aluminum source. An INFICON crystal monitor and INFICON XTC/266 deposition controller allowed real time monitoring of the deposition rate and semi-automatic control of the thickness of the deposition. A thin metal mask with 3.3 mm diameter holes was placed over the sample in order to define the aluminum dot contacts. The deposition parameters typically used were a base pressure of  $4 \times 10^{-6}$  Torr with a deposition rate on the order of 20 angstroms per second until about 500 nanometers of aluminum film was deposited.

### 3.3 Photonic Crystal Fabrication

The flow diagram of the multi-step process used to incorporate a photonic crystal into the ACTFEL device is shown in figure 3-4. Further details of the procedure are as follows in this section. The first step was RF magnetron sputter deposition of a ZnS:ErF<sub>3</sub> thin film on top of an as received substrates consisting of aluminum-titanium oxide (ATO) on indium-tin oxide (ITO) on glass. Next, an array of holes was created in the ZnS:ErF<sub>3</sub> layer by spin coating a polymethylmethacrylate (PMMA) positive electron-resist layer which was patterned over a 1.5 x 1.5 mm area by exposure to an electron beam (EB) and development. This patterned PMMA served as a mask during argon ion etch which transferred the pattern into the ZnS:ErF<sub>3</sub> thin film. Excess PMMA was removed and a top dielectric layer was deposited into the holes in and across the surface of the ZnS:ErF<sub>3</sub> layer to complete the photonic crystal with contrasting dielectric constants as discussed in Chapter 2. Finally, 3mm diameter circular aluminum dot contacts were deposited by electron beam evaporation to complete the ACTFEL device structure.

#### 3.3.1 Electron Beam Lithography

Electron beam lithography was carried out on a Philips XL40 field emission scanning electron microscope (SEM) operated at 30KV under the control of the Nanometer Pattern Generation System (NPGS) from J.C. Nability, Inc. Patterns were drawn out using DesignCAD® which allows for the following drawing elements: lines of arbitrary slope, circles, circular arcs, and arbitrary filled polygons, among others. An NPGS run file was created in order to control the electron dose applied to each point and to control the geometry and spacing of points to write the photonic crystal pattern onto the PMMA according to the dimensions set forth in the DesignCAD® pattern. The maximum dimension of the individual pattern that could be written by deflection of the electron beam was  $150 \times 150 \mu\text{m}^2$ , but the stage was stepped by the run file to create a 10 x 10 array of patterns covering a total area of 1.5 x 1.5 millimeters. Patterns

requiring beam deflections beyond  $150 \times 150 \mu\text{m}^2$  exhibited distortions, in particular at the edges, due to the deleterious effects of beam deflection on focus and stigmatism of the electron beam. Typical parameters for electron beam writing were a beam current of 350 picoamps at an accelerating voltage of 30 kV with a spot size of 3 and a working distance of 10 millimeters.

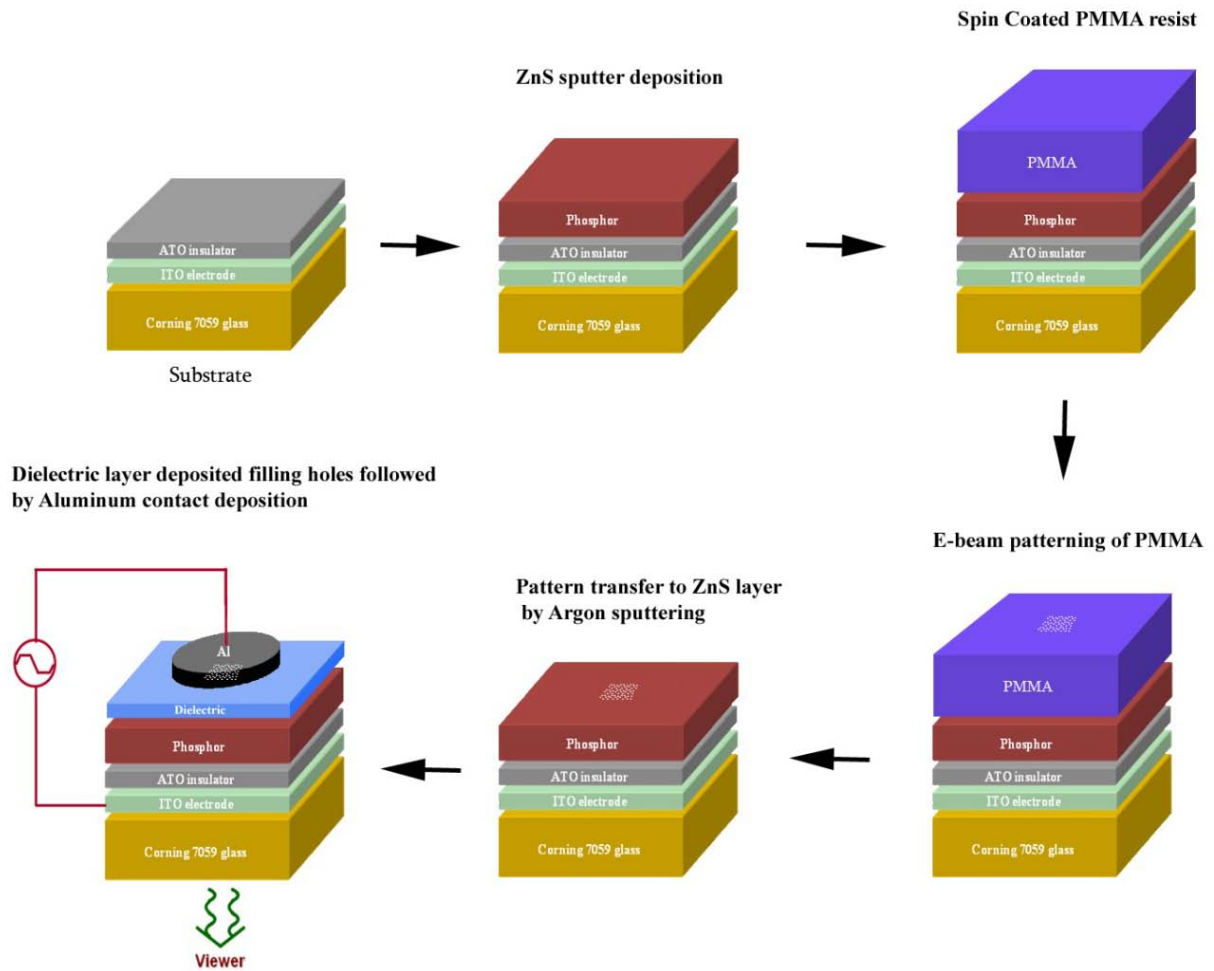


Figure 3-4 Photonic crystal device fabrication flow chart.

The PMMA electron beam resist, from Microchem Corporation had a molecular weight of 950,000 and was in a 4% solution with chlorobenzene. The PMMA acts as a positive resist such that irradiated regions become soluble in the developing chemical solution while non-irradiated regions remain insoluble. Before patterning, substrates were cleaned using a methanol rinse,

followed by a 10 minute oxygen plasma clean (Harrick model PDC-32G) with 18W applied to the RF coil. Then the PMMA was spin coated onto the substrate at 3000 rpm for 30 seconds using a Specialty Coating Systems Model p6700 spin coater. The thickness of the PMMA is ~500 nm as shown in Figure 3-5 which correlates film thickness with the spin coating speed for resist C4.

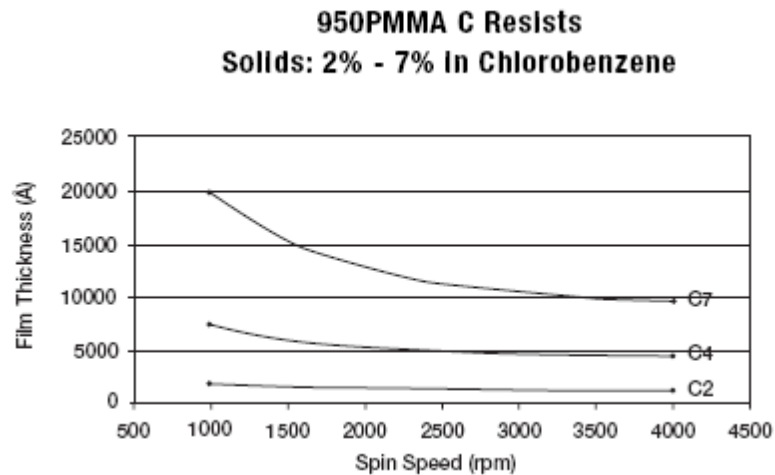


Figure 3-5 Film thickness versus spin coating speed for PMMA [107]

A hot plate post bake at 180°C for 10 minutes was used to remove the chlorobenzene solvent. After the PMMA had been exposed under the electron beam it was developed by a solution of 1 part methyl-isobutyl-ketone to 3 parts isopropanol for 75 seconds, followed by an isopropanol rinse.

### 3.3.2 Plasma Sputter Etch

The patterned PMMA mask was used to transfer the pattern into the underlying ZnS:ErF<sub>3</sub> layer by an argon ion physical etch in a Plasma Therm 770 SLR system. The discharge was generated in a low profile ASTEX 4400 ECR source (0–1000 W at 2.45 GHz), and the sample chuck power was separately biased with rf (13.56 MHz) power, typically 125W. The resultant DC self-bias was a function of both plasma chemistry and microwave power, but typical values

were 180 to 205 V at 125W RF. The etch gas pressure was controlled by throttling the main pump (1500 l s<sup>-1</sup> turbomolecular pump) and typically was set to 1 mTorr. The argon gas was injected directly into the ECR source at a flow rate of 30 standard cubic centimeters per minute. To reduce the deleterious effects on the PMMA mask of the heat associated with the argon etch, the maximum continuous etch time was 25 seconds long which etched 85 to 95nm of ZnS:ErF<sub>3</sub>. This was followed by cooling over approximately 5 minutes, followed by another 25 second etch. Typically five 25 second argon etches were used resulting in etched depths of approximately 500nm. Residual PMMA material remaining after the etch was removed by sonication in an acetic acid bath.

### **3.4 Device Characterization**

#### **3.4.1 Structural Characterization**

Film thicknesses for the deposited ZnS:ErF<sub>3</sub> thin films were typically determined by using a piece of bare 1"x2" Corning 7059 glass with a strip of Kapton® tape running the length of the glass as a mask in order to create a step once the tape was removed after the deposition, as discussed above. Film thickness was measured with a KLA Tencor P-2 Long Scan Profilometer, and the average step height was used as the film thickness.

Once the ZnS:ErF<sub>3</sub> thin film had been etched through and residual PMMA removed, the surface topology was analyzed for PC hole diameter, spacing and depth. A Philips FEI XL-40 field emission SEM was used for device structure characterization. This technique provided information on the hole diameter and spacing, but depth information was difficult to obtain. Instead, profiles of photonic crystal holes were obtained with a Digital Instruments Dimension 3100 atomic force microscope (AFM). The AFM tip was a Veeco Probes type RTESP tapping mode tip of the following dimensions: Tip Height = 15 μm – 20 μm, Front Angle (FA) = 15°,

Side Angle (SA) =  $17.5^\circ$ , Tip Set Back (TSB) =  $15\ \mu\text{m}$ . Figure 3-6 shows an image and schematics of this Veeco Probe Tip [120].

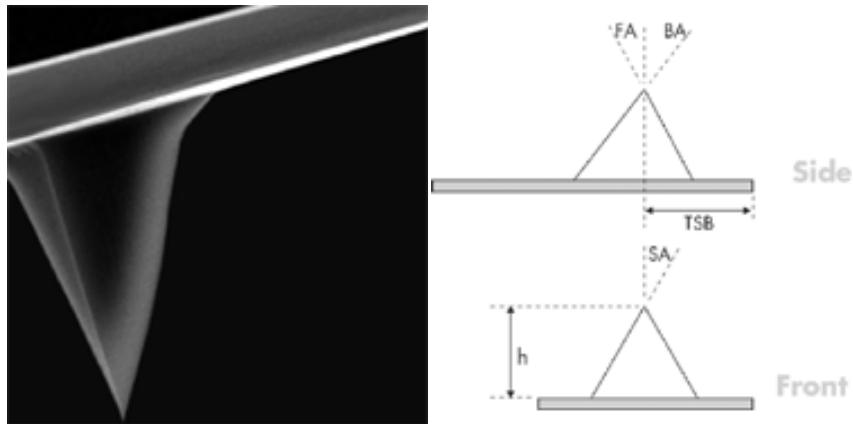


Figure 3-6 Veeco Probe tapping tip model RTESP image and schematic [120].

Since the dimensions of the cylindrical PC hole was  $\sim 250$  nanometers in diameter by 500 nanometers deep, the tip was expected to distort the image of the hole.

### 3.4.2 Compositional Characterization

To determine the chemical composition of the film, energy dispersive spectroscopy (EDS) was used. EDS uses the fluorescent X-rays produced by the primary electron bombardment of the sample in an SEM, refer to section 2.5.2 [121]. A JEOL 6400 SEM with a tungsten filament and an EDS detector was used to excite and detect x-rays emitted by the samples. The typical operating voltage of 20 kV was used to test half-stack devices, i.e. ACTFELDs without the top dielectric layer or electrode. The bottom ITO layer and carbon paint provided a conductive path to avoid charging.

In addition to EDS, a Perkin-Elmer PHI 660 Scanning Auger Multiprobe was used to map the composition of an area containing the photonic crystal structure. The main benefit of the data obtained from EDS and AES is analysis of the different compositions of the top of the ZnS:ErF<sub>3</sub> layer versus the bottom of the holes in this layer.

The concentration of erbium in the ACTFEL device is critical to the intensity of emissions from the device, [46] and secondary ion mass spectroscopy (SIMS) [122] was utilized to determine the relative erbium concentrations. SIMS is a qualitative characterization technique that provides good sensitivity and excellent depth resolution. A Perkin-Elmer/Physical Electronics 6600 Quadrupole Dynamic SIMS system was used. Depth profiles obtained by SIMS can also be used in conjunction with profilometry data to determine film thicknesses [123].

### **3.4.3 Optical Characterization**

The optical properties of brightness and emission spectrum were measured for all fabricated devices and deposited films, refer to section 2.6.1 for ACTFEL device optical characterization. Electroluminescent (EL) emission was driven by a custom driver based on a design by Planar Systems, Inc. Devices were excited with 2.5 kHz positive and negative trapezoidal pulses with a rise time of 5  $\mu$ s, a 30  $\mu$ s hold time and 5  $\mu$ s fall time. Emitted light was analyzed using an Oriel MS257 0.25m monochromator using reflective optics. A chopper and lock-in detection scheme was used to improve the signal-to-noise ratio. Filter wheels are used at the input to the monochromator to minimize detection of second and third harmonics. An Oriel model 77345 silicon-based photomultiplier tube (PMT) was attached to the off-axis port to detect emission wavelengths between 250 and 800 nm. An Oriel model 71614 thermoelectrically cooled germanium photodiode was attached to the on-axis port to detect emission wavelengths between 0.8 and 2  $\mu$ m. An Oriel Merlin radiometry system interfaced with the monochromator, chopper and detectors utilizing custom software written with Visual Basic was used for data collection. A schematic of the optical bench is shown in figure 3-7.

The spectrometer was calibrated using an Oriel model 63358 QTH calibrated lamp over the 200 to 2400 nm range. A 1  $\text{cm}^2$  aperture was used to define the source area and the lamp was

placed 50 cm from the sample position to minimize reflected light. The full emission spectrum was measured using fixed optics and constant monochromator settings so that the irradiance value could be used to generate a calibration curve, with units of  $\mu\text{W}/\text{cm}^2 \cdot \text{V}$ , that can be used to quantify the irradiance from any sample. Irradiance is obtained by multiplying collected data, in V, by the calibration constant for a given wavelength, resulting in units of  $\mu\text{W}/\text{cm}^2 \cdot \text{nm}$ .

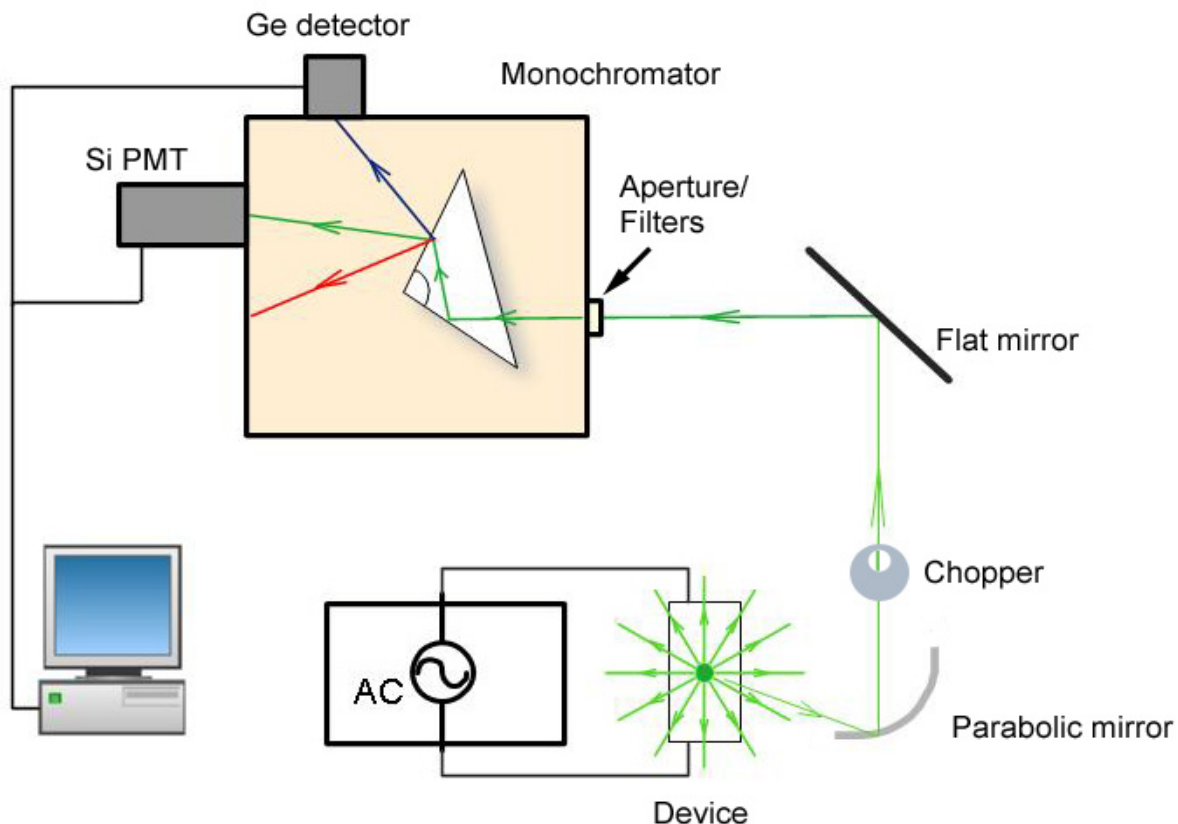


Figure 3-7 Optical Bench schematic

For normal emission, the device was placed in a holder that had a direct line of sight to a conical mirror which collects and directs that light towards the monochromator. Spring mounted probe contacts make electrical connection to the aluminum dot and to indium soldered through a scratch to the ITO conducting layer of the device allowing voltage to be applied to cause EL. The emitted intensity versus angle was also measured from the devices. The devices were mounted onto a rotation stage in a direct line of sight to the input port of the monochromator

with the chopper sitting in between and the devices were rotated while the data were collected corresponding to the rotation angle.

CHAPTER 4  
EFFECTS OF PHOTONIC CRYSTAL STRUCTURE IN ACTFEL DEVICES ON LIGHT  
SCATTERING AND ANGULAR EMISSIONS

**4.1 Introduction**

In this chapter the effects of photonic crystals (PCs) on the angular emissions of ACTFELDs will be considered as well as the light reflecting effects of the PC structure. Light emissions from the devices were measured with respect to the angle of emission. An empirical correlation exists between diffuse reflectance of a device and the degree of optical outcoupling from that device due to the fact that increased light scattering leads to increased outcoupling [47]. Diffuse reflectance measurements made by comparing the devices to a diffuse reflection standard are conducted in order to obtain information relating to the light outcoupling performance of the devices.

Erbium doped ZnS phosphor material possesses a near-infrared optical transition at 1550 nm, which has potential application in optical communications and advanced wound healing therapies [51, 124, 125]. The emission is the result of excitation and radiative relaxation of erbium luminescent centers in the phosphor film. ZnS:ErF<sub>3</sub> ACTFEL devices have several EL emission peaks [126, 79]. Visible emission at 525 and 550 nm corresponds to  $^2H_{11/2} \rightarrow ^4I_{15/2}$  and  $^4S_{3/2} \rightarrow ^4I_{15/2}$  transitions, respectively. Near-infrared emission at 1550 nm corresponds to the  $^4I_{13/2} \rightarrow ^4I_{15/2}$  transition. Additional emission peaks occur at 662, 985 and 1300 nm corresponding to the  $^4F_{9/2} \rightarrow ^4I_{15/2}$ ,  $^4F_{7/2} \rightarrow ^4I_{11/2}$  and  $^4S_{3/2} \rightarrow ^4I_{11/2}$  transitions, respectively. The energy levels and transitions for erbium are shown in Figure 4-1 and 2-5 [126, 79]. Figure 4-1 also presents a typical electroluminescence (EL) emission spectrum showing the major transitions for ZnS:ErF<sub>3</sub> ACTFEL devices.

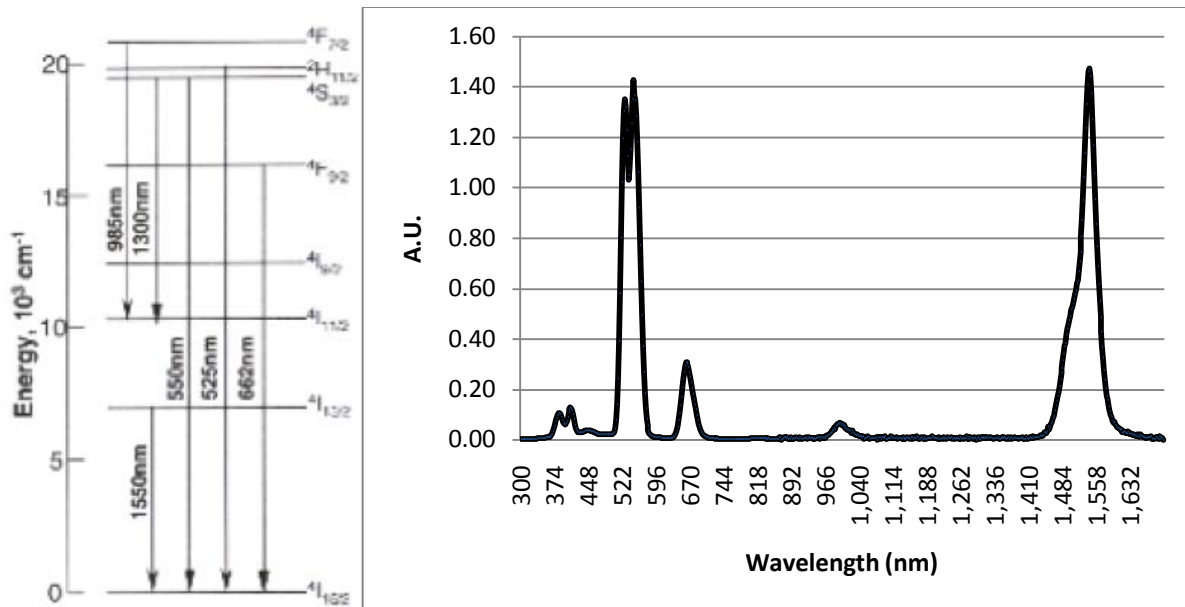


Figure 4-1 Energy levels and transitions for erbium in ZnS:ErF<sub>3</sub> ACTFELDs and typical emission spectrum [79, 80, 126].

The purpose of this study is to determine the effect a photonic crystal structure has when incorporated into the ZnS:ErF<sub>3</sub> layer of an ACTFEL device. The parameters of the photonic crystal structure have been tailored to a photonic band gap for the 1550 nm near-infrared (NIR) emission from the devices. The parameters that define the photonic band gap include the lattice geometry, lattice spacing, cylinder diameter and dielectric constant mismatch between cylinders and matrix. A photonic crystal structure designed to affect 1550 nm wavelength light may not necessarily affect 550 nm light depending upon whether or not a photonic band gap exists for both the 550 nm and 1550 nm wavelengths of light. For the parameters used in this study, a 550 nm wavelength photonic band gap is not expected based on theoretical modeling. Comparisons between the unaffected 550 nm emission versus the 1550 nm emission provide a means to quantify the photonic crystal effect. When considering the angular emission of the device, light emitted at 550 nm should only experience differences in scattering between photonic crystal and non-photonic crystal devices. However, since 1550 nm light should experience the effects of the

photonic crystal, there should be a difference in the 1550 nm light between photonic and non-photonic crystal structures.

In order to fully investigate photonic crystal phenomenon, three device types have been made. The first type is a device with no photonic crystal patterning and simply consists of the flat stacks of the thin films constituting the device; this device will be referred to as the NOPC device. The second device type is one in which the photonic crystal structure has been fabricated; this device will be referred to as the PC device. The final device provides a second type of control and is processed the same as the photonic crystal device except that the order of the array has been randomized to break up any photonic crystal effect due to the ordered array; this device will be referred to as the RND device.

## **4.2 Experimental Procedure**

The EL phosphors consist of ZnS:ErF<sub>3</sub> thin films that were RF planar magnetron sputter deposited onto standard glass/indium-tin oxide (ITO)/aluminum-titanium oxide (ATO) substrates. A process flow overview for device fabrication and photonic crystal incorporation is shown in Figure 4-2 and final device structures consisted of the “full-stack” structure described in section 2.1.2. As a quick summarization of figure 4-2, the phosphor layer is deposited onto the substrate and is then patterned with holes in the design of the photonic crystal which are then filled with a dielectric material and the device is completed with the deposition of a top aluminum electrode. Then the device is ready for electroluminescent characterization.

### **4.2.1 Substrate**

Corning 7059 glass of 0.04 inches thick coated with 360 nm of polycrystalline indium tin oxide (ITO) (90 wt% In<sub>2</sub>O<sub>3</sub> + 10 wt% Sn<sub>2</sub>O<sub>3</sub>), as transparent conducting electrode, and 160 nm of amorphous aluminum-titanium oxide (Al<sub>2</sub>O<sub>3</sub> / TiO<sub>2</sub>) (ATO), as the bottom insulating layer, comprise the initial substrate for device fabrication as supplied by Planar Systems. Atomic layer

deposition (ALD) was used to deposit the ATO insulating layer resulting in a high quality, homogeneous film. Substrate preparation begins with a dry nitrogen gas dusting to remove airborne particulates. Further substrate cleaning is done using an UVOCS, Inc. ultraviolet light ozone cleaner for six minutes to remove organic contaminants. For the purpose of thickness measurements, additional substrates of bare Corning 7059 glass were prepared using the same method.

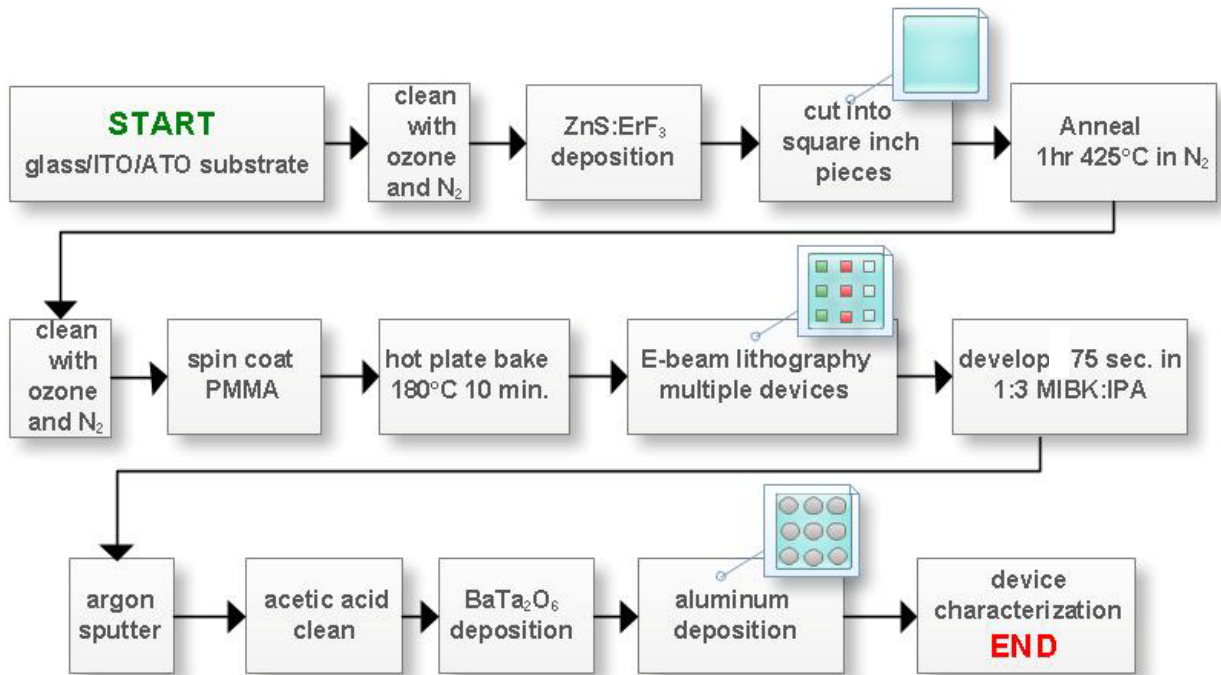


Figure 4-2 Process flow overview for ZnS:ErF<sub>3</sub> photonic crystal ACTFEL device fabrication

#### 4.2.2 Phosphor Layer Deposition

Two independently controlled RF magnetron sputter guns are used to deposit the ZnS:ErF<sub>3</sub> phosphor layer. One sputter gun contains a CVD grown polycrystalline pure ZnS target source purchased from Morton Thiokol, Inc. The other sputter gun uses a ZnS doped with ErF<sub>3</sub> compound target purchased from SCI Engineering Materials. This target is prepared by mixing 98.5 wt% ZnS powder and 1.5 wt% ErF<sub>3</sub> powder and hot pressing in inert gas to form the

target. The Corning 7059 glass coated with ITO and ATO substrates are placed on a sample platter with the capacity for four 2" x 2" substrates or eight 2" x 1" substrates. The sample platter is rotated at a speed of 8 revolutions per minute. The deposition chamber is evacuated to a base pressure between  $1.5 \times 10^{-6}$  and  $3.5 \times 10^{-6}$  Torr prior to phosphor deposition. Argon is used as the sputter gas and is introduced into the chamber using Unit UFC 1100A 20, 50 or 100 sccm mass flow controllers on three inlet lines. The argon pressure was 20 mTorr. The temperature of deposition was 150°C. The power applied to both the targets was 100 W, while the duty cycle for the undoped target was 100%, the duty cycle for the doped target varied from 40% to 75% depending upon the optimization of the resulting light emission characteristics prior to photonic crystal incorporation. Similarly, the deposition time was also varied from 60 to 150 minutes resulting in film thickness ranging from 400 to 700 nm, times and thicknesses resulting in optimum emission characteristics were used. Following phosphor layer deposition, devices were annealed in a quartz tube with an ultra high purity nitrogen (99.9999%) ambient at 425°C for 60 minutes. Halogen lamps placed above and below the quartz tube provided appropriate heating. The temperature inside the quartz tube was monitored by a thermocouple in conjunction with a Micristar controller used to control the power applied to the heating lamps.

#### **4.2.3 Electron Beam Lithography**

Substrates are cut into one square inch sections. In preparation for electron beam (e-beam) lithography, a substrate is cleaned with methanol then treated for 10 minutes in an oxygen plasma cleaner using a Harrick model PDC-32G plasma cleaner with 18W applied to the RF coil. Then PMMA is spin coated onto a substrate at 3000 rpm for 30 seconds using a Specialty Coating Systems model p6700 spin coater. For curing, the substrate is hot baked on a hot plate for 10 minutes at 180°C. Now the substrate is ready to undergo the e-beam lithography step. A DesignCAD® pattern consisting of a honeycomb array of circles of diameter 325 nm spaced at

806 nm covering an area of 150 x 150 square microns is used for e-beam writing. This area was determined best to minimize the deleterious effects of beam deflection as described in section 3.3.1. The line spacing and center-to-center distance of the write are both 24.97 nm. The area dose for exposure is set to 600  $\mu\text{C}/\text{cm}^2$ . The working distance is 10 cm and the magnification is 1100x. In order to cover a significantly large area of the device the 150 x 150 square micron pattern is repeated 100 times in 10 rows and 10 columns creating a total pattern covering a 1.5 x 1.5 mm square area. Stage alignments are used to step the patterns. Due to the limited resolution of the stage movement mechanism a buffer of about 10 microns between patterns is used to eliminate any possible overlap.

#### **4.2.4 Argon Sputter**

Argon sputtering is performed in a Plasma Therm 770 SLR system in which the discharge is generated in a low profile ASTEX 4400 ECR source (0–1000 W at 2.45 GHz), and the sample chuck power is separately biased with rf (13.56 MHz) power. The chuck power is set at 125W, and the ECR power set to 900W. The process pressure is set to 1 mTorr. The argon gas is injected directly into the ECR source at a flow rate of 30 standard cubic centimeters per minute. Five runs of 25 seconds long each, providing approximately 85 nm of ZnS:ErF<sub>3</sub> etching each, are carried out. Several minutes are taken between runs to allow time for cooling. Residual PMMA material remaining after etching is removed by dissolution in an acetic acid bath under sonication.

#### **4.2.5 BaTa<sub>2</sub>O<sub>6</sub> Deposition**

Barium tantalate (BaTa<sub>2</sub>O<sub>6</sub>) is deposited using a Materials Research Corporation magnetron sputter deposition system. Deposition was carried out with 8.8 mTorr of a mixture of 80% argon to 20% oxygen. The RF forward power was 400 Watts with a reflected power of 35 Watts, providing a peak voltage of 0.5 Volts. The deposition time was 9 hours. The thickness of

the sputtered film was ~400nm. By taking the capacitance of the BaTa<sub>2</sub>O<sub>6</sub> film the dielectric constant was found to be ~20.

#### **4.2.6 Top Opaque Electrode**

Aluminum comprises the top opaque electrode of the device, which is deposited by electron beam evaporation. A shadow mask with a circular dot size of 0.069 cm<sup>2</sup> is used. Aluminum is evaporated using a Davis and Wilder Electron Beam Coating System to a thickness of 500 nm. The base pressure for this process is approximately 6 x 10<sup>-6</sup> Torr. Electrical contact to the bottom (ITO) electrode is made by scratching through the phosphor layer and dielectric layer with a diamond-tip scribe. A piece of pure indium metal wire is then melted, using a soldering iron, into the scratch such that it wets to the ITO layer resulting in an electrical contact.

#### **4.3 Physical Structure Analysis**

Atomic force microscopy (AFM) is used to characterize the surface topographies obtained from the device processing steps. AFM analysis is conducted after the processing step of argon sputtering which transfers the PMMA pattern into the ZnS:ErF<sub>3</sub> layer and after any excess PMMA has been removed by an acetic acid cleaning. Figure 4-3 shows a two-dimensional image of a 7 x 7 μm<sup>2</sup> area of holes in the ZnS:ErF<sub>3</sub> layer probed by AFM.

The depths of the holes is determined by averaging over a sampling of typically 15 holes using the AFM software program to view line scan depth profiles. The values determined for the average hole depth for the PC structure and the RND structure are 403 nm with a standard deviation of 16 nm and 397 nm with a standard deviation of 19 nm, respectively. The thickness of the ZnS:ErF<sub>3</sub> layer was ~650 nm thick.

The AFM micrograph is also analyzed using imageJ® software in order to determine the average hole diameter and lattice spacing as well as to quantify variance from the average.

Photo manipulation of threshold and balance is carried out for the elimination of noise and to

distinctly mark the holes. The manipulated image comprises black holes on a white background, which enables the software to easily quantify the parameters of radii and center positions of the holes.

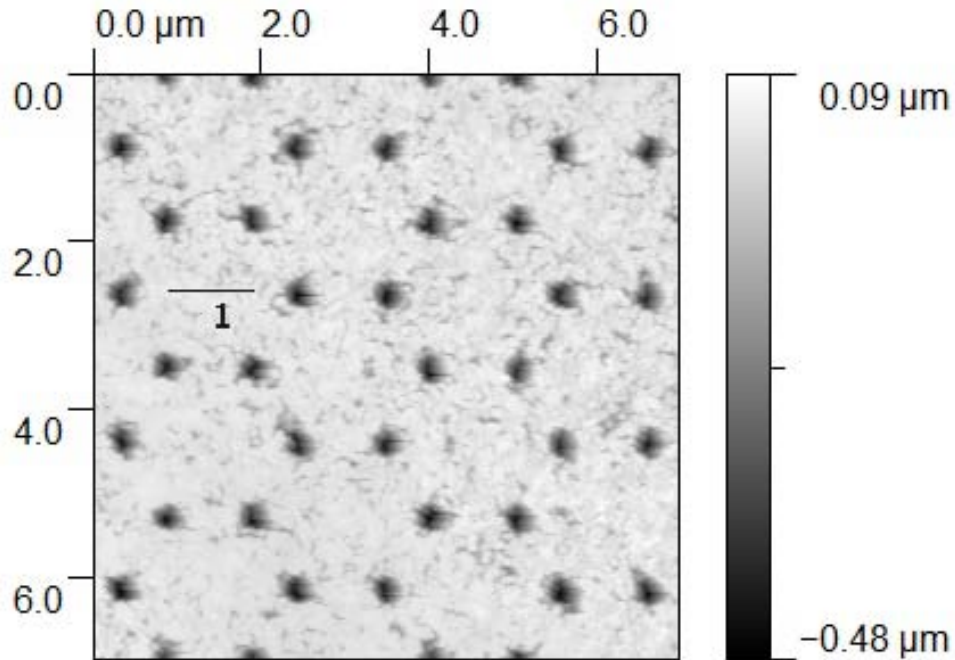


Figure 4-3 AFM analysis of a PC device

An image showing the manipulation of the AFM image of figure 4-3 is shown in figure 4-4, where the holes have been numbered and outlined. The average hole diameter for the PC device was 348 nm with a standard deviation of 20 nm and the average lattice spacing was 998 nm with a standard deviation of 16 nm. For the RND device the average hole diameter was 372 nm with a standard deviation of 73 nm.

Further analysis was carried out through energy dispersive spectroscopy (EDS). Figure 4-5 shows an EDS scan of the ZnS:ErF<sub>3</sub> layer. The strong zinc and sulfur signals are expected due to the presence of the ZnS:ErF<sub>3</sub> layer at the surface of the sample. Weak signals from aluminum, indium and titanium come from the layers under the ~650 nm ZnS:ErF<sub>3</sub> film. The

oxygen signal is present due to the alumina and titania of the bottom dielectric layers as well as from surface oxygen contamination.

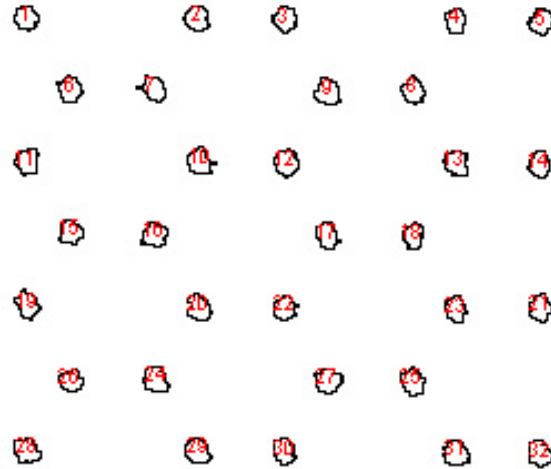


Figure 4-4 Image produced by ImageJ® from the AFM data for spatial analysis.

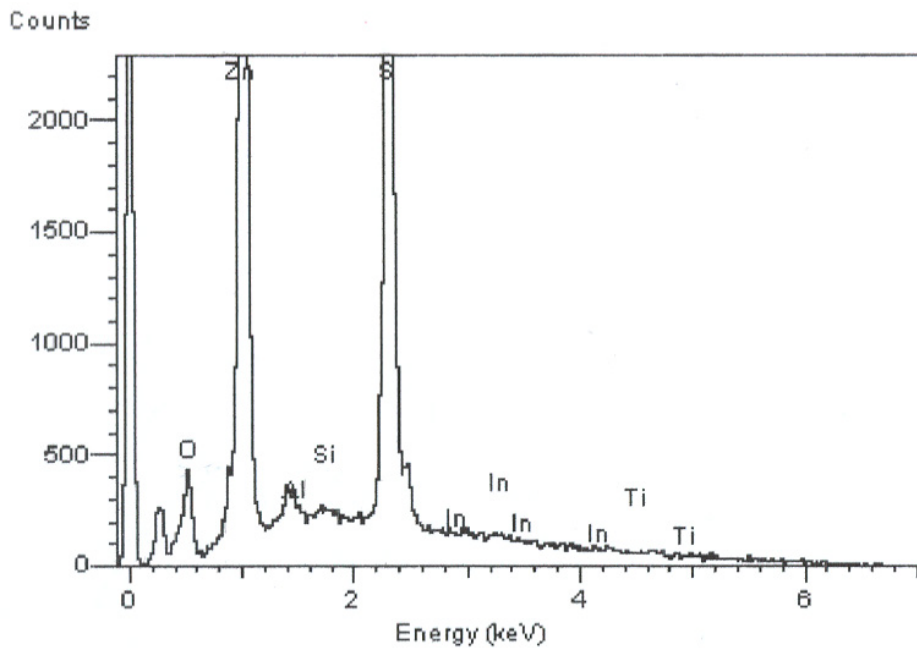


Figure 4-5 EDS spot scan of ZnS:ErF<sub>3</sub> layer.

For devices processed to the same device processing step as that for when AFM was taken, namely holes patterned into the ZnS:ErF<sub>3</sub> layer, EDS provides additional information.

Figure 4-6 shows on the left an SEM photomicrograph of a patterned surface with a horizontal

line in the center along which the relative intensities of the secondary electron current (image) and Zn, Al and S  $L_{\alpha}$  or  $K_{\alpha}$  x-ray intensities are plotted to the right.

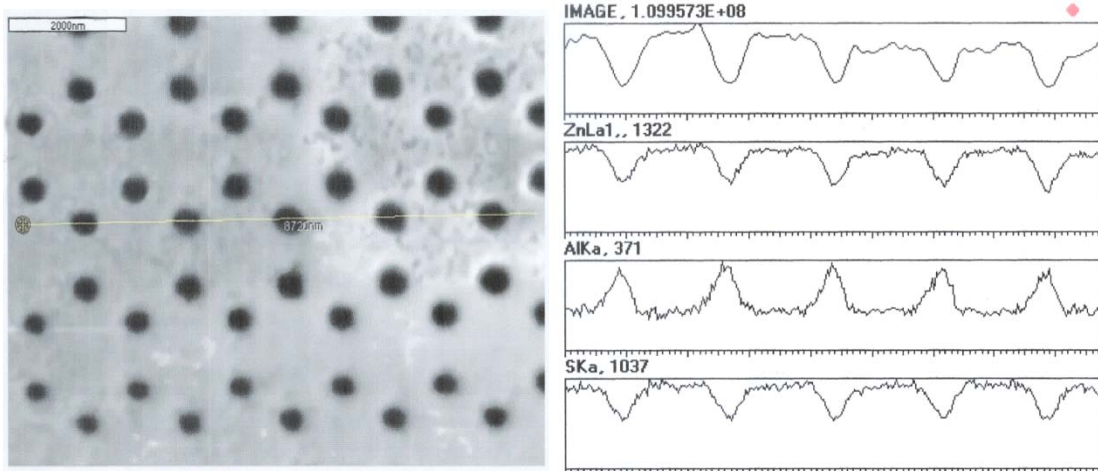


Figure 4-6 EDS line scan analysis of patterned ZnS:ErF<sub>3</sub> layer.

It is clear from these data that the zinc and sulfur signals decrease when the line scan crosses the holes, while the aluminum signal becomes stronger in the holes. This is expected due to the fact that the layer beneath the ZnS:ErF<sub>3</sub> layer is ATO which contains aluminum causing increased aluminum detection at the bottom of the holes. These data show the chemical correlation to the physical AFM data are consistent with the existence of holes in the ZnS:ErF<sub>3</sub> layer. Whether or not the bottoms of the holes are at the ATO/ZnS:ErF<sub>3</sub> interface cannot be determined from these data due to the possibility of electron beam penetration of any thin layer of residual ZnS:ErF<sub>3</sub> at the bottom of the holes. Matching the AFM depth of holes data to the thickness of the ZnS:ErF<sub>3</sub> film also does not provide conclusive evidence due to variations in hole depth and film thicknesses. The film thickness for these devices is on the order of 650 nm while the average hole depth found from AFM was ~400 nm. It is not believed that creating holes flush to the ATO layer is vital to the effects of the photonic crystal structure because if the

photonic crystal structure is present there will be an effect on the light. There does exist a critical thickness for the optimization of the photonic crystal effect which is maximized around the thickness region of 0.6 times the lattice spacing [127]. This would imply that for a structure with lattice spacing of 1000 nm the ideal thickness would be 600 nm. Since the devices measured in this chapter fall short of this thickness there is room for improvement.

#### 4.4 Theoretical Analysis

Photonic band gap modeling was carried out using the MIT Photonic-Bands (MPB) package with Mark Allen's gap map add on program [88, 89]. The main input variables are lattice pattern and dielectric mismatch between regions with a high and low dielectric constant. The lattice pattern used in this research is the honeycomb structure of high dielectric cylinders contained in a low dielectric matrix. For the devices reported in this chapter the dielectric constant of the ZnS:ErF<sub>3</sub> layer was ~9 and the dielectric constant for the BaTa<sub>2</sub>O<sub>6</sub> was ~20, providing a dielectric mismatch of ~11. Figure 4-7 shows the calculated photonic band gap map for a honeycomb structure of high dielectric cylinders embedded in a low dielectric matrix with a dielectric mismatch of 11.4. The lattice spacing ( $a$ ), which is equivalent to the lattice parameter of the honeycomb lattice, and the diameter ( $d$ ) of the holes are indicated in the insert of figure 4-7. The y-axis of figure 4-7 indicates the frequency of light which experiences the plotted band gaps and scales with the lattice spacing. The light gray regions indicate photonic band gaps for the TM mode, the gray regions indicate band gaps for the TE mode and the black regions indicate a complete photonic band gap where the two modes overlap. The gap map of figure 4-7 is independent of dimension, but when the wavelength of interest is set to 1550 nm, then the y-axis scales to 1550 nm and the x-axis is dependent upon the y-axis. The inserted horizontal line in figure 4-7 indicates a lattice spacing of 998 nm as dependent upon scaling the gap map to

1550 nm and the vertical line indicates a hole diameter of 348 nm. These are the average values determined from the imageJ® analysis of the PC device from section 4.3.

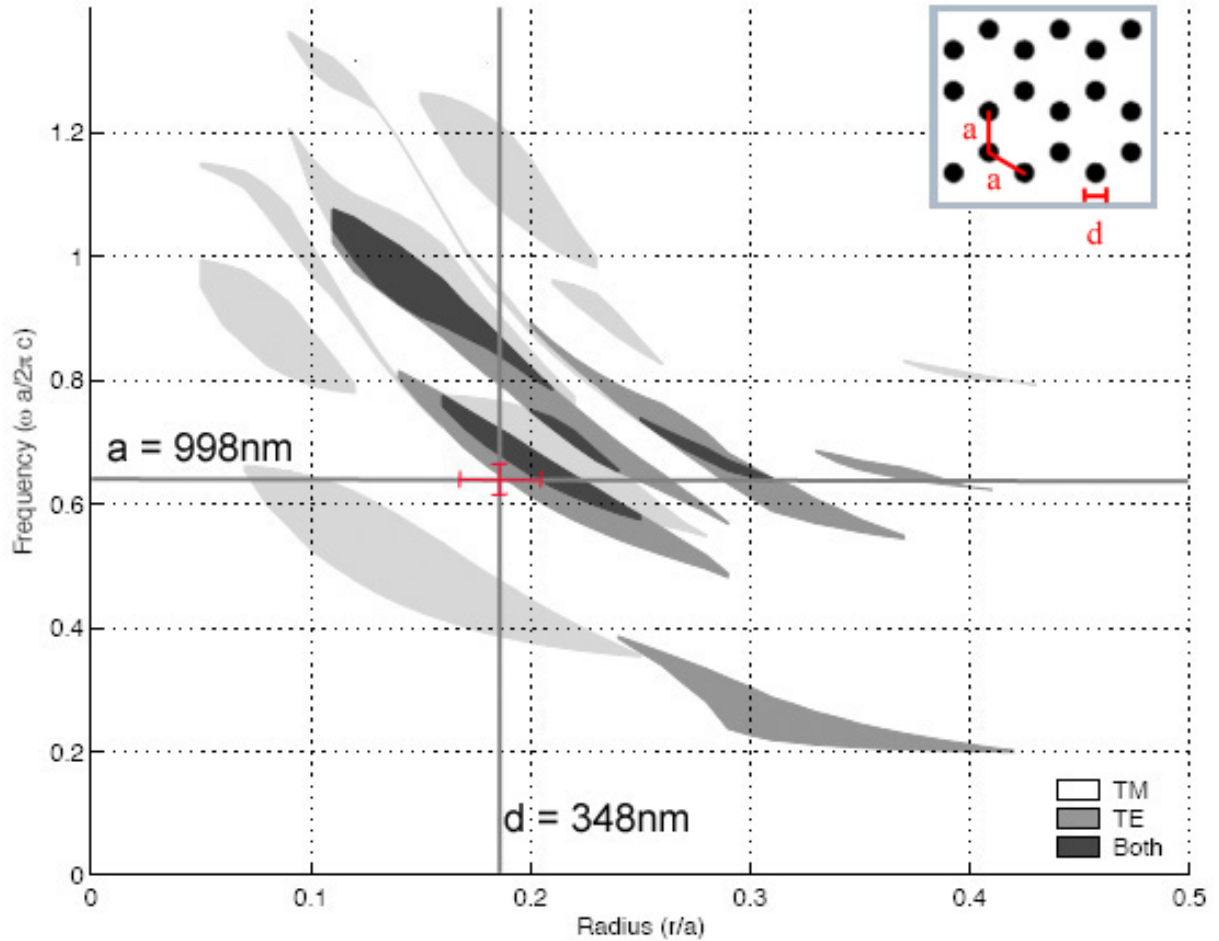


Figure 4-7 Photonic band gap map for honeycomb structure with dielectric mismatch of 11.4. The horizontal and vertical bars indicate the standard deviations from the analysis in section 4.3. If this gap map is scaled to affect 550 nm wavelength light, then the position on the map for a lattice spacing of 998 nm and hole diameter of 348 nm would place the position at 1.8 on the y-axis with the same x-axis value, which would be well away from any photonic band gap region. In this case in order to achieve the same photonic band gap position as in the case of the 1550 nm light, the structure required would be a lattice spacing of 354 nm and hole diameter of 123.4 nm, which would be more difficult to fabricate.

## 4.5 Optical Analysis

Reflectance data was taken to provide information regarding the effects on light propagation through the device resulting from incorporating a photonic crystal or random structure into the device. Due to the correlation between diffuse scattering and optical outcoupling, measurement of the diffuse scattering of the devices will yield information beneficial in understanding the optical response of the device structures. Reflected intensity normalized to a diffuse reflectance standard measurements were taken using an Ocean Optics® setup as diagramed in figure 4-9 with the light source and exiting light for detection set at an angle of 45 degrees to the sample. Figure 4-10 shows the diffuse reflectance spectra for the three types of devices over the detector's wavelength range.

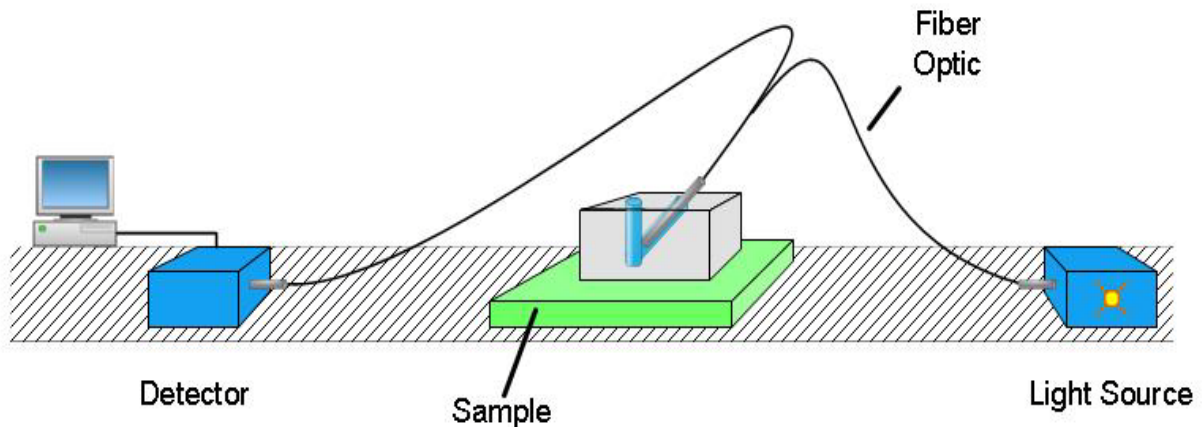


Figure 4-9 Ocean Optics reflectance measurement setup.

The spectra shown in Figure 4-10 are very similar to one another for the three device types. Since the added structuring of the PC and RND devices does not significantly influence the diffuse scattering throughout the device, this indicates that the diffuse scattering of light would not make a major contribution to the increase of outcoupling in the PC and RND devices.

Angle resolved emissions data from devices were collected using an optical bench consisting of a rotation stage and sample holder, chopper, aperture, monochromator, and detector as shown in figure 4-11. The sample sat 100 mm from a rectangular aperture with dimensions of 12 mm high by 5 mm wide which yielded a solid angle of 0.0106. Devices were held on the rotation stage in direct line of sight into the aperture, and driven at 150 volts. The rotation stage had demarcations at one degree intervals comprising a full 360 degrees of the circle. The zero degree angle corresponded to the visual alignment of the sample surface plane perpendicular to the aperture, i.e. the surface normal of the sample was parallel to the optical axis between the sample and the aperture. At 90 degrees the sample was perpendicular to the optical axis. Devices were rotated from minus 20 degrees to plus 90 degrees with data collected at 5 degree intervals. Figure 4-12 shows the normalized angle resolved emissions results for the three device types: PC, RND, NOPC.

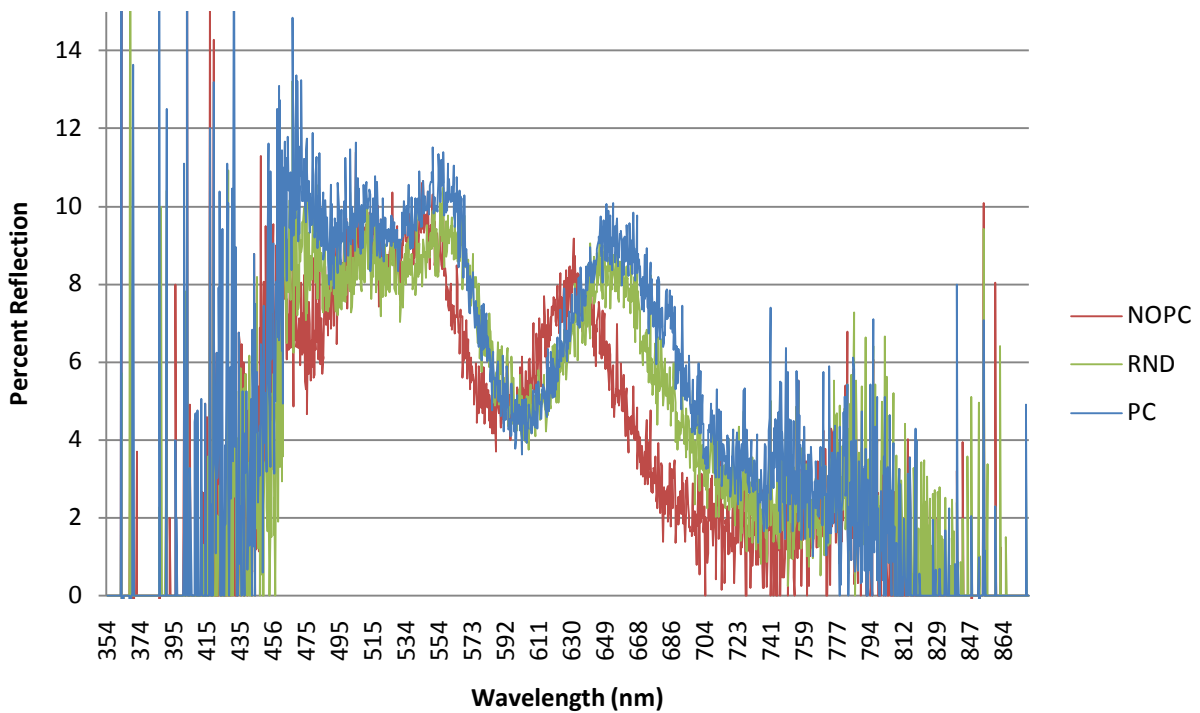


Figure 4-10 Diffuse reflectance spectra for the three device types (PC, RND, NOPC).

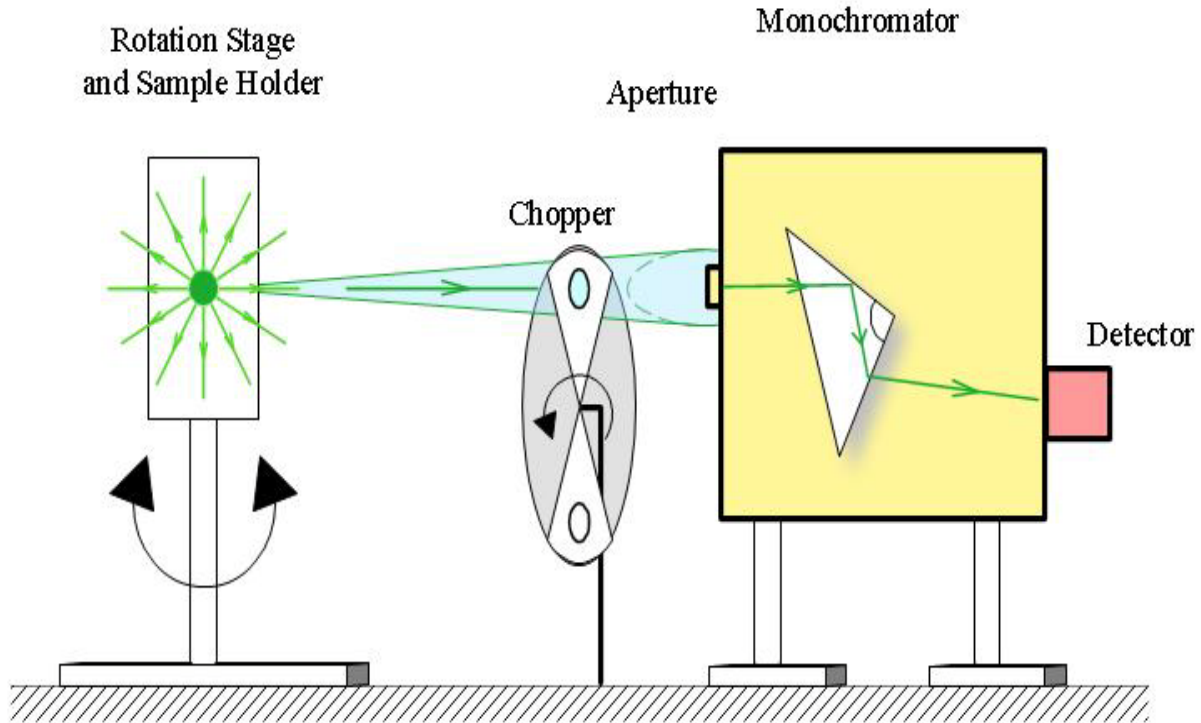


Figure 4-11 Optical Bench setup for angle resolved emission.

The PC device shows increased emissions at about 15 degrees emission angle relative to the 0 degree emission angle as compared to the RND and NOPC devices. For the RND and NOPC devices, emissions from 0 degrees to 15 degrees showed an ~11% reduction while for the PC device there was an ~7% increase. This increase is due to frustration of modes in the film due to the photonic crystal structure and not due to scattering effects. Since there is no band gap for 550 nm light it is expected that the only variation to the light output of 550 nm light from the devices would be due to scattering effects. For light output at 1550 nm where there should be a photonic band gap, deviations from the NOPC device would be expected for the photonic crystal device and not for the random device, since it has no photonic band gap to affect the 1550 nm light. This scenario is confirmed by the data, leading to the belief that the photonic crystal structure causes the deviation in the 1550 nm angular light output.

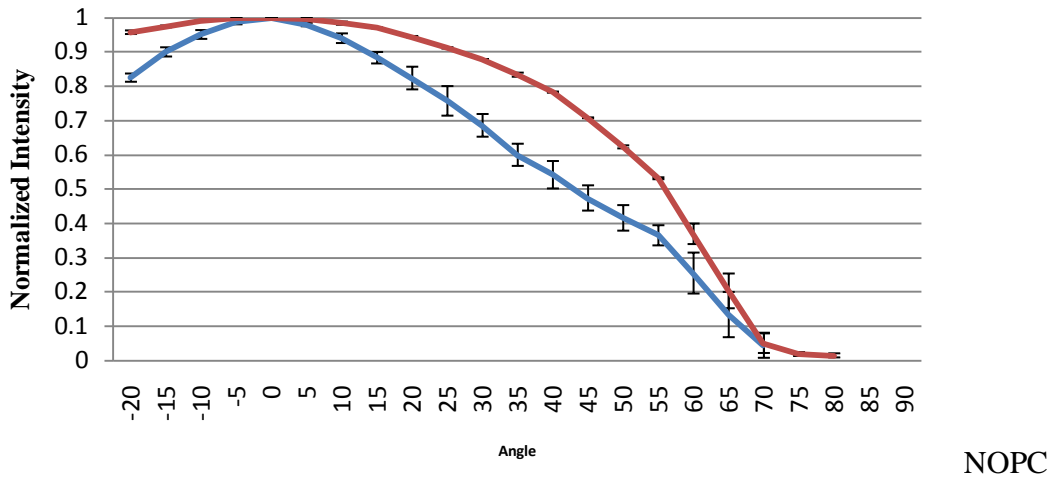
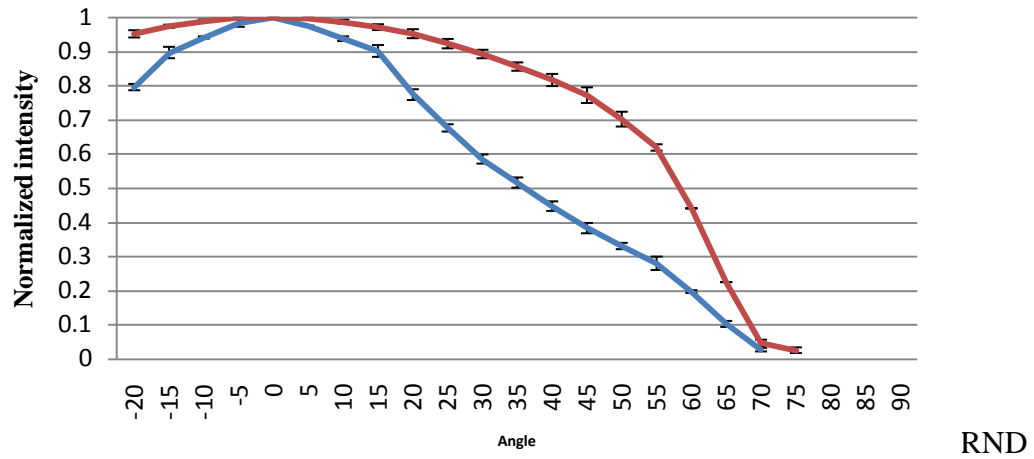
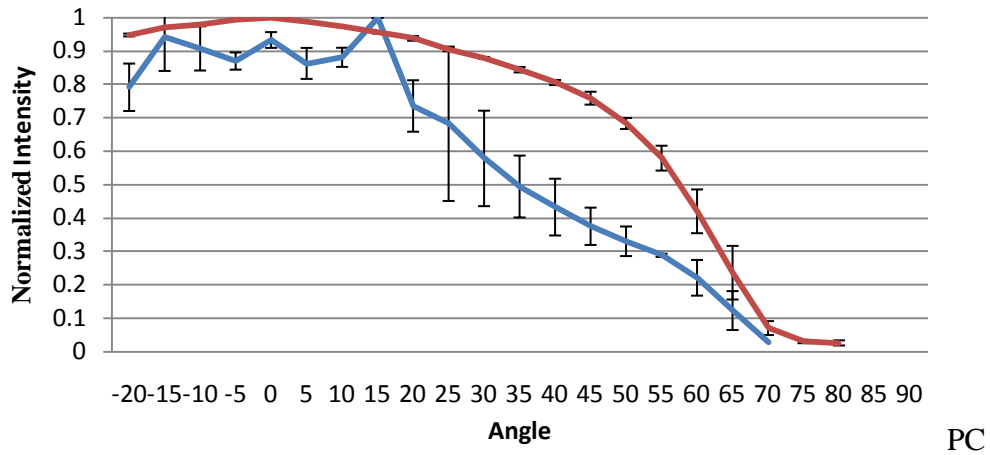


Figure 4-12 Normalized angle resolved emissions data for PC, RND and NOPC devices with the red lines corresponding to 550 nm emission and the blue lines to 1550 nm emission.

## CHAPTER 5 EFFECTS OF PHOTONIC CRYSTAL STRUCTURE IN ACTFELDS ON INFRARED EMISSION

### 5.1 Introduction

The effects of incorporating a photonic crystal structure into the active layer of a ZnS:ErF<sub>3</sub> ACTFELD with a different top dielectric layer on infrared electroluminescence emissions are reported in this chapter. The purpose of this study is to increase near-infrared optical outcoupling of ACTFEL devices by the incorporation of a photonic crystal structure into the ZnS:ErF<sub>3</sub> layer of the device. The ratio of the 1550 nm to the 550 nm light emission can be used to compare different photonic crystal devices and to devices with no photonic crystal structure. The ratio is expected to increase for devices with photonic crystal structures of appropriate dimension to create a photonic band gap inhibiting light propagation along total internal reflecting directions thus transferring the light to modes of propagation which lead to outcoupling from the device, for 1550 nm light. The 550 nm light will not be increased because the structure does not provide for a photonic band gap for this wavelength of light.

### 5.2 Experimental Procedure

The procedure for device fabrication is identical to that as detailed in section 4.2 except for yttria-stabilized-zirconia (YSZ) was used as the dielectric instead of BaTa<sub>2</sub>O<sub>6</sub>. YSZ was deposited in a Kurt J. Lesker CMS-18 Multi-target sputter deposition system. The sputtered film was ~900 nm thick. By taking the capacitance of the YSZ film the dielectric constant was found to be ~24.

### 5.3 Physical Structure Analysis

Atomic force microscopy (AFM) is used to characterize the structures obtained after the processing step of argon sputtering which transfers the PMMA pattern into the ZnS:ErF<sub>3</sub> layer and after any excess PMMA has been removed by an acetic acid clean. Figure 5-1 shows three-

dimensional images of  $7 \times 7 \mu\text{m}^2$  areas of holes in the  $\text{ZnS:ErF}_3$  layer probed by AFM; the left side is for a photonic crystal device while the right is for a device with a random array of holes. Figure 5-1 also shows line profiles taken from the two three-dimensional renders taken for the three lines as indicated on each.

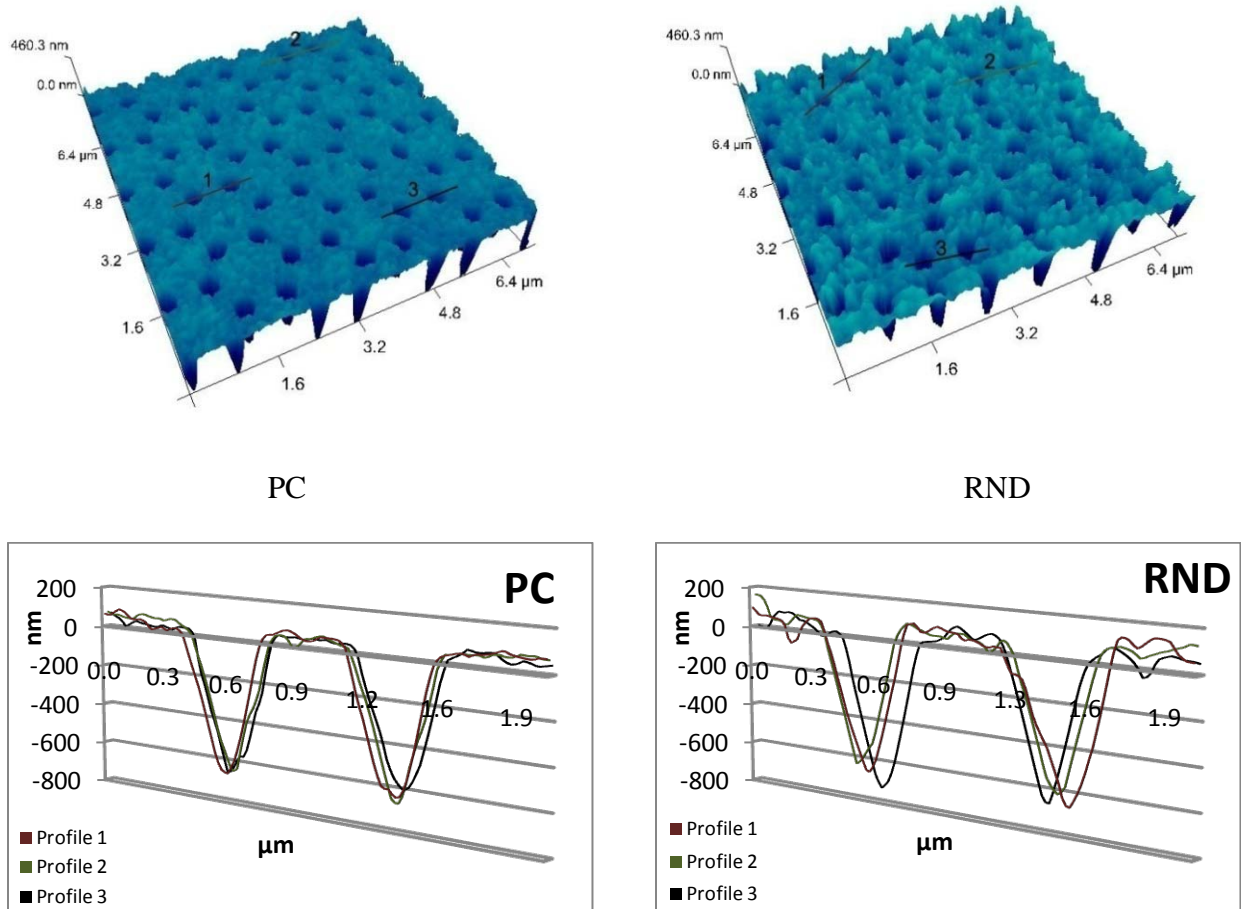


Figure 5-1 AFM images and line profiles for PC and RND devices.

The depths of the holes are determined by averaging over a sampling of  $\sim 20$  holes. The “V” shape of the holes is believed to be due to the “V” shape of the AFM tip. Using the parameters of the AFM tip, as provided in section 3.4, at 650 nm up from the bottom of the tip the diameter would be approximately 348 nm which would indicate that the profiles in figure 5-1

are images of the tip. The values determined for the average hole depth for the PC structure and the RND structure are 648 nm with a standard deviation of 31 nm and 683 nm with a standard deviation of 18 nm, respectively. The thickness of the as-deposited ZnS:ErF<sub>3</sub> layer was ~650 nm. The data were also analyzed using imageJ® software in order to determine the average hole diameter and lattice spacing as well as to quantify the variance from the normal. For the PC device, the average hole diameter was 342 nm with a standard deviation of 11 nm; the average lattice spacing was 748 nm with a standard deviation of 12 nm. For the RND device the average hole diameter was 369 nm with a standard deviation of 25 nm.

#### **5.4 Theoretical Analysis**

From the lattice spacing and column diameter parameters obtained from the physical structure analysis, the photonic crystal optical band gap can be conducted. The calculated dielectric constant for the YSZ film ranged from 24-40. By using MIT MPB program with Mark Allen's band gap program, for a structure of high-dielectric columns in a honeycomb structure embedded in a low dielectric matrix with a dielectric difference of 20 between the low- and high-dielectric regions, the optical band gap map correlating band gaps to lattice spacing ( $a$ ) and column diameter ( $d$ ) was calculated. Figure 5-2 shows such a gap map with an insert indicating  $a$  and  $d$ . As described in section 4.4 these gap maps are independent of dimension; they scale to whatever the wavelength of interest is. For example to achieve a band-gap for 550 nm light the lattice spacing and column diameters will be smaller than that necessary for the same band gap for 1550 nm light. Inserted into figure 5-2 are lines for the average lattice spacing and average radius of columns found for the 1550 nm device analyzed in the previous section 5.3. The red horizontal and vertical lines indicate the standard deviations of the results. In figure 5-2 the light gray shaded regions correspond to optical TM mode band-gaps and the gray shaded regions are TE mode gaps; the black regions occur when the TE and TM mode gaps overlap forming a

complete band-gap. The location of the structure analyzed is inside a complete band-gap region for 1550 nm light. For 550 nm light the red X mark of figure 5-2 indicates the position for the photonic crystal structure which is well away from any gaps.

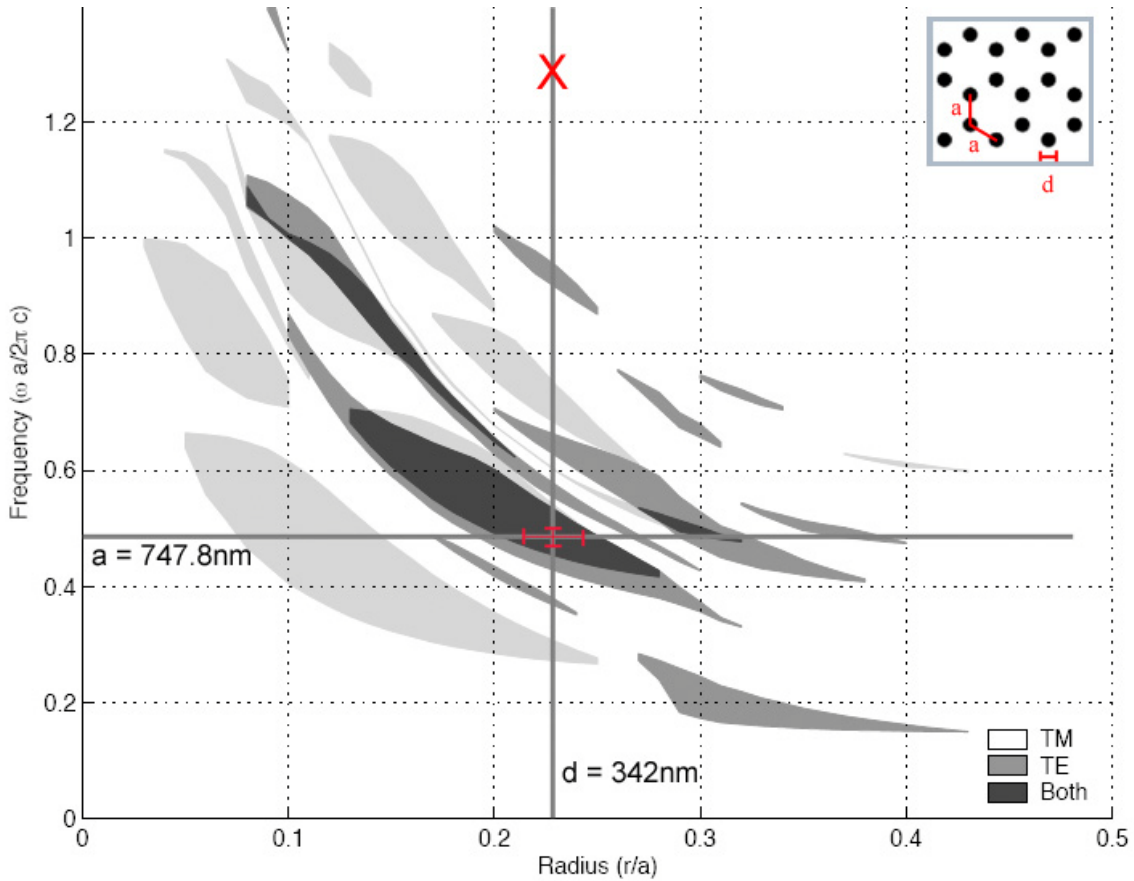


Figure 5-2 Photonic band gap map for honeycomb structure with dielectric mismatch of 20.

Increased light scattering from techniques such as increased surface roughness have been shown to increase the optical outcoupling of light emitting devices [128]. This leads to the analysis of increased optical outcoupling which may arise due to increased scattering provided by the cylinders present in a photonic crystal versus a randomly patterned device. The following is an analysis of optical scattering of light based on the assumption that the columns of the photonic crystal structure can be approximated as spheres in order to use the Mie scattering theory of light. Mie scattering calculation software is used to make these calculations [129].

Figure 5-3 contains the light scattering curves calculated from Mie theory showing the magnitude of scattering versus the angle between entrance and exit rays for 550 nm and 1550 nm light.

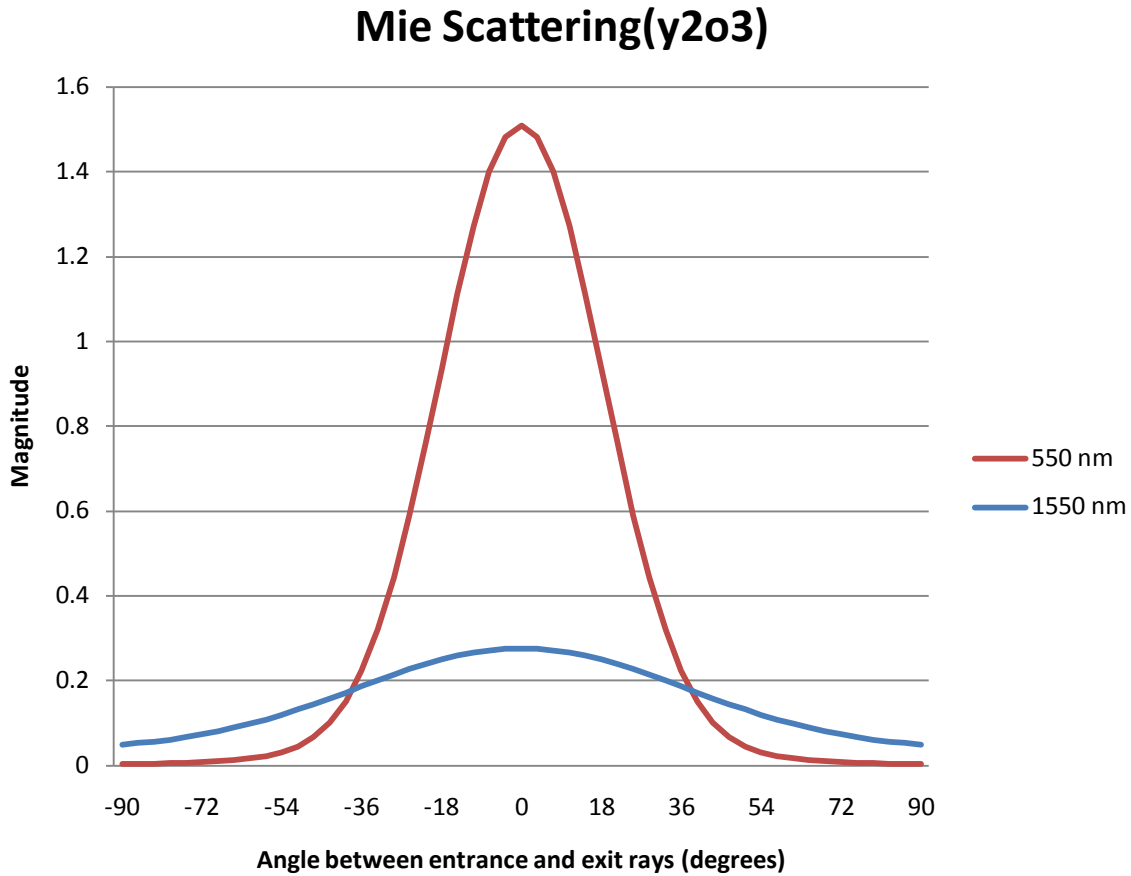


Figure 5-3 Mie calculated scattering for YSZ scattering spheres in a ZnS:ErF<sub>3</sub> matrix for 550 nm and 1550 nm wavelength light [129].

The input variables for both curves are the refractive index of the spherical YSZ and refractive index of the ZnS:ErF<sub>3</sub> medium which are both wavelength dependent, sphere diameter (341.9 nm as taken from PC hole diameter) and sphere concentration which was kept constant at 2 spheres per cubic micron for both PC and RND devices. When applying the scattering analysis of figure 5-3 to the devices which contain columns it is beneficial to analyze the light propagating in the plane of the ZnS:ErF<sub>3</sub> as the incident light. The area under the scattering curve of figure 5-3 is

equivalent to the percentage of light which is scattered over the given angles. Examining the 550 nm scattering curve the percentage of light scattered to high angles, ranging from 36 to 90 degrees, is only about 2% of total light scattering. As for the 1550 nm light, the scattering at angles of 36 to 90 degrees accounts for about 37% of total scattering. Light propagating in the plane of the ZnS:ErF<sub>3</sub> layer will not outcouple from the device. Only the light that scatters at large angles from this in plane propagating light will be able to reach a sufficient angle in order to outcouple from the device. Assuming that increased scattering leads to increased optical outcoupling [47], based on this analysis there will be increased light output at 1550 nm, due to the higher percentage of high angle scattering, in comparison with the 550 nm light which undergoes little high angle scattering. This analysis implies that there will be a higher ratio of 1550 nm to 550 nm emission for the random device structure than that of the no photonic crystal structure device in which there are no columns which would cause scattering in the ZnS:ErF<sub>3</sub> layer.

## 5.5 Optical Analysis

An optical bench setup is used to collect optical emissions data from the devices. Devices are set in a sample holder aligned for light emission into a conical collector mirror aimed such that the collected light travels through a chopper, a filter, an aperture, a monochromator and finally into a detector as shown in figure 5-4. Devices were driven by an alternating current power supply capable of delivering up to 300 volts. The sample was physically aligned for the maximum signal and TracQ® software was used to collect the emissions data. Figure 5-5 shows plots of brightness ( $\mu\text{W}/\text{cm}^2$ ) versus time at various voltages for the three device types; the left graph is for 550 nm emission and the right graph is for 1550 nm emission. All three devices experienced a 10-30% decay in brightness over times of 30-60 seconds, which is believed to be caused by defects in the YSZ dielectric layer. The rate of decay

slows after a period of ~30 seconds and becomes nearly stable. It is in this comparatively stable region where values are taken in order to analyze the different devices. Figure 5-6 shows the percentage change from the NOPC flat stack device to the RND and PC devices for 550 nm emission on the left and 1550 nm emission on the right.

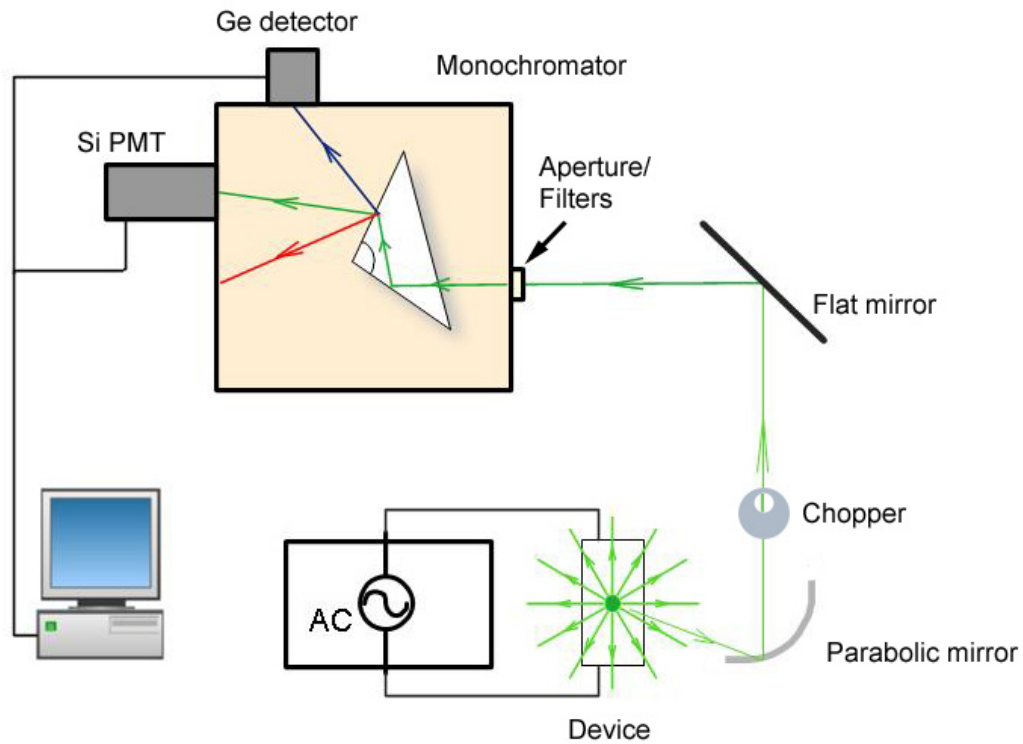


Figure 5-4 EL measurement on the optical bench.

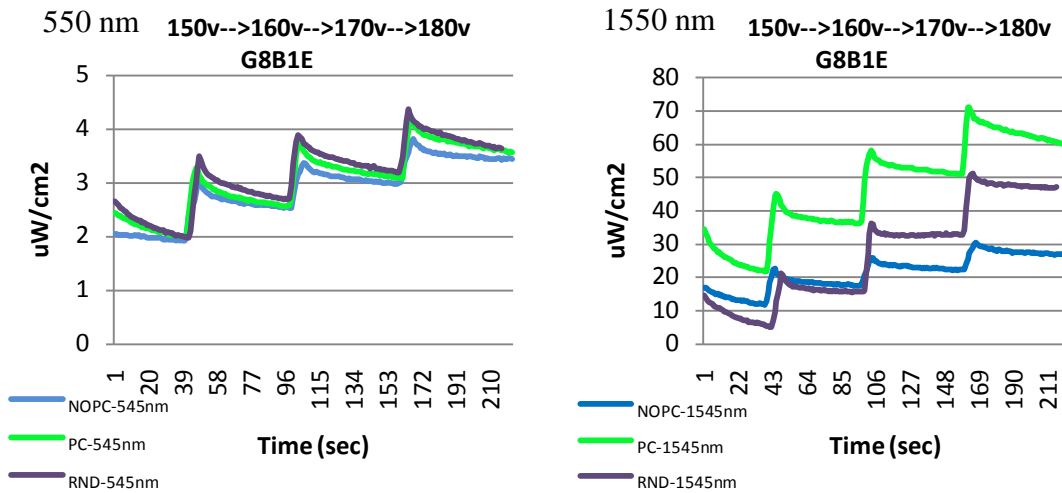


Figure 5-5 Brightness versus time at various voltages plots.

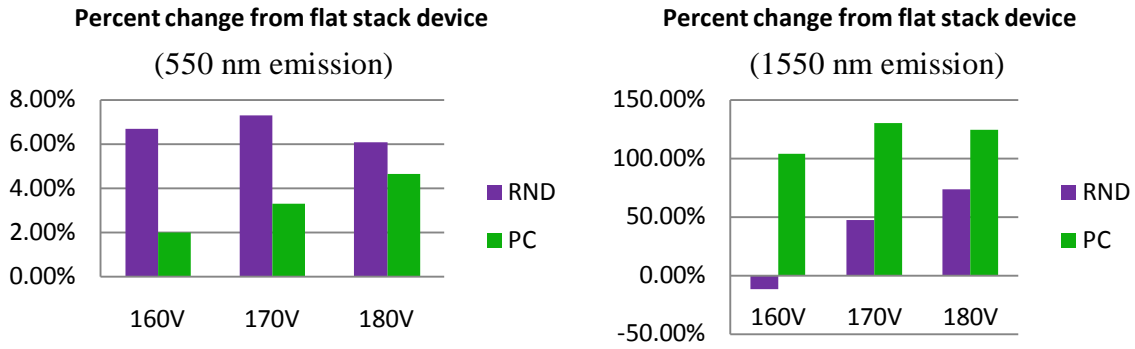


Figure 5-6 Percent change in luminance for RND and PC devices normalized to the NOPC device.

In order to more clearly analyze the optical emissions a comparison is made between the IR emissions and the VIS emissions. Figure 5-7 shows the ratio of 1550 nm light to the 550 nm light for the three devices at three voltages.

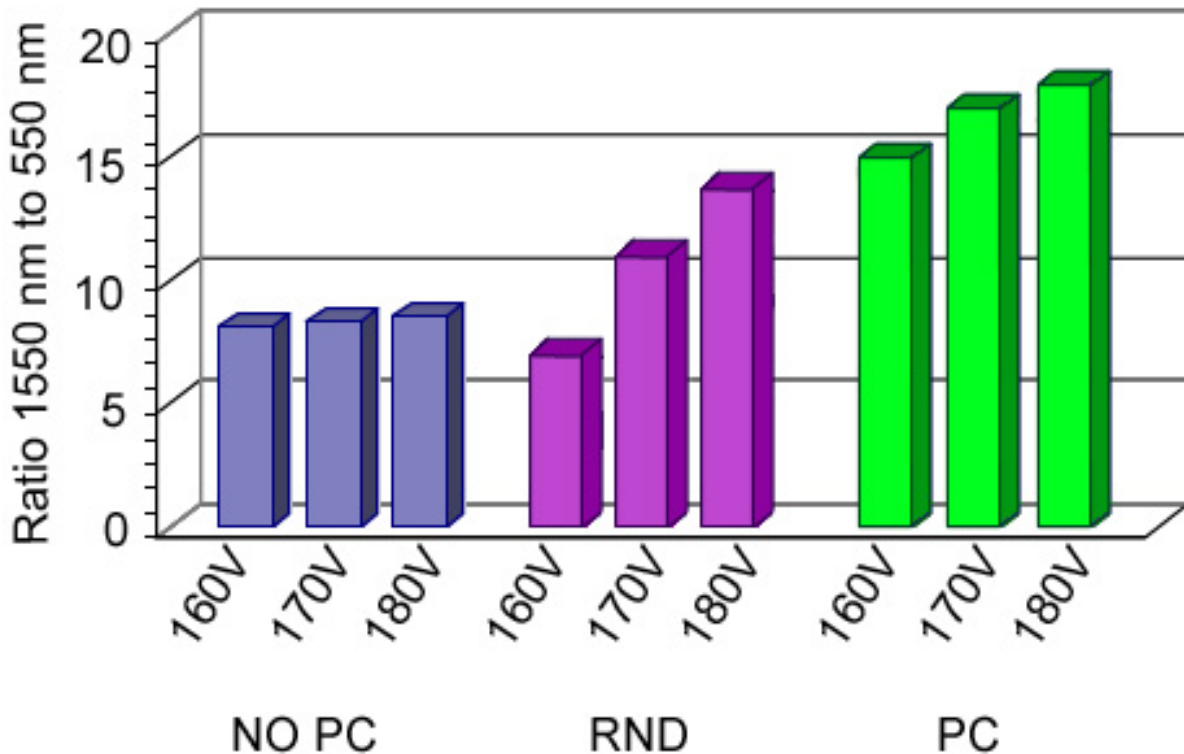


Figure 5-7 Ratio of IR/VIS for devices at 3 voltages.

## 5.6 Discussion

Based on the data in figure 5-7 the photonic crystal structure caused the inhibition of totally internally reflected light at 1550 nm due to the photonic band gap while simultaneously redistributing that light to modes of propagation leading to an approximately two fold increase in outcoupling. The IR/VIS ratio data (figure 5-7) clearly show that there is an enhancement in the IR emissions of the photonic crystal structured device compared to the flat stack device. For comparison, Fujito et al. reports an approximately three to five fold increase in vertical emission of a photonic crystal quantum-well device [93].

The mechanism of scattering also plays a role in emissions. The Mie scattering analysis as presented in section 5.4 indicates that the 1550 nm light should be scattered more at high angles as compared to the 550 nm light resulting in preferential enhancement of the 1550 nm light compared to the 550 nm light. This analysis explains why there is an increased IR/VIS ratio for the RND structured device compared to the NO PC device. However, since the PC structure device shows an even greater enhancement of 1550 nm emission this enhancement can not be attributed solely to a scattering affect. The photonic crystal band gap property, transferring internally reflected modes of light propagation to outcoupling modes of light propagation, explains this extra enhancement.

Another area of key importance in data interpretation is the electrical characteristics of the devices. In order for accurate comparisons to be made the devices must be driven at comparable voltages. If the incorporation of a photonic crystal structure causes the device to turn on at much lower voltage, comparing devices at the same applied voltages would not necessarily ensure equality of brightness. One method to ensure equal driving conditions between devices is to analyze the brightness versus voltage curves of the devices and if the curves are similar then direct comparisons between devices at equal driving voltages would be

acceptable. Figure 5-8 shows partial brightness versus voltage (B-V) curves for the three types of devices under consideration as well as a curve indicating an ideal B-V curve for an ACTFEL device.

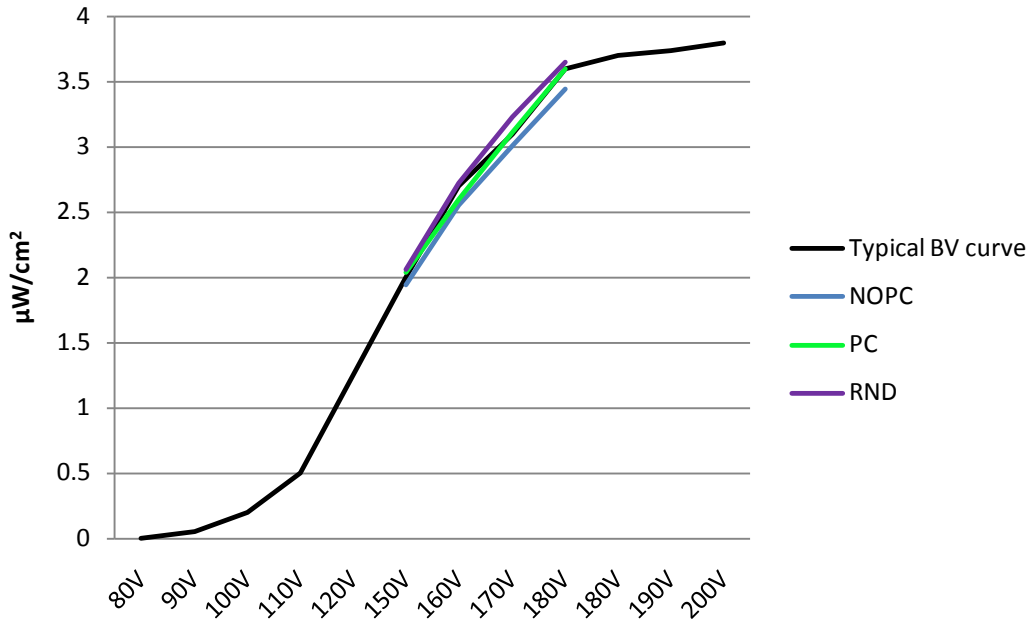


Figure 5-8 Brightness versus voltage curves for the three types of devices in this study, and for an “ideal” ACTFEL device.

From figure 5-8 it is clear that the three device types perform very similarly which justifies the comparisons between devices at equal voltages.

## CHAPTER 6 CONCLUSIONS

### 6.1 ACTFEL Photonic Crystal Fabrication

A process to fabricate photonic crystal structures incorporated into an ACTFEL device has been developed and implemented. This multi-step process consisted of 1) depositing ZnS:ErF<sub>3</sub> thin film phosphor on an ATO (Al<sub>2</sub>O<sub>3</sub>-TiO<sub>2</sub>)/ITO (indium-tin oxide)/glass substrate using RF magnetron sputter deposition, 2) depositing polymethylmethacrylate (PMMA) on the substrate using spin coating, 3) patterning the PMMA using electron beam lithography, 4) developing the patterned PMMA in a solution of methyl isobutyl ketone and isopropyl alcohol, 5) transferring the pattern from the PMMA to the underlying ZnS:ErF<sub>3</sub> thin film by argon sputter etching, 6) removing all excess PMMA, 7) depositing a dielectric layer thin film across the surface and into the holes created in the ZnS:ErF<sub>3</sub> layer to complete the photonic crystal structure, and 8) depositing aluminum top electrodes to complete the device structure. In this research significant effort was required to optimize the electron beam lithography of the PMMA and pattern transfer into the ZnS:ErF<sub>3</sub> layer by argon sputter etching. For the electron beam lithography, the most difficult step was to properly account for the additive property of radiative doses from adjacent exposure points. Therefore, proper dose per point and distance between points was critical to obtaining the desired result of uniform circular holes in the PMMA without defects. For the argon sputtering step, the most difficult step was to achieve sufficiently deep etches to reach the ZnS:ErF<sub>3</sub> layer before destroying the PMMA layer [130]. Therefore, the argon ion etch was only done for 25 seconds at a time and the PMMA was given sufficient time (typically about five minutes) to cool between etch cycles. This allowed for a deeper etch down into the ZnS:ErF<sub>3</sub> layer to be achieved before the PMMA lost its effectiveness as a mask.

## 6.2 Photonic Crystal Properties

Photonic crystals consisting of electromagnetic media structured with proper periodic geometry and scale exhibit a photonic band gap at particular wavelengths of light. In this research, fabrication of alternating current thin film electroluminescent (ACTFEL) photonic crystal devices has been shown by the characteristics of the devices, by both structural and optical response analysis. The optical intensity data are consistent with the photonic crystal structures prohibiting propagation of light parallel to the surface and simultaneously redistributing the energy into light propagating in modes normal to the surface [93]. In this research photonic crystal ACTFEL devices were fabricated which display this phenomenon of prohibiting modes of light in the thin film which do not outcouple, while simultaneously transferring a fraction of this energy to modes which do outcouple.

The first type of ACTFEL device, as detailed in Chapter 4, consisted of a full stack ACTFEL device with barium tantalate filling the etched PC holes and as a top sandwiching dielectric layer to provide a dielectric mismatch of  $\sim 11$  for the photonic crystal structure in the ZnS:ErF<sub>3</sub> layer. The photonic crystal device had the honeycomb lattice structure with a lattice spacing of 998 nm, a hole depth of 403 nm and a hole diameter of 348 nm. The angle resolved emissions data for this photonic crystal device were unique when compared to the random structure and non-photonic crystal devices for 1550 nm light. The photonic crystal device exhibited a maximum intensity of emission at an angle of 15 degrees off normal to surface while the random structure and non-photonic crystal devices both exhibited maximum emission intensity at the normal to surface angle. The photonic crystal structure's 15 degrees emission was  $\sim 7\%$  greater than its normal to surface emission, while for the random structure and non-photonic crystal structure devices their 15 degrees emission was  $\sim 11\%$  less than their 0 degree emissions. For light emission at 550 nm, the angle resolved emissions were indistinguishable for

the three devices. This analysis serves to show that indeed the photonic crystal structure preferentially affects only the 1550 nm light as theorized. The second type of device, as detailed in Chapter 5, consisted of a full stack ACTFEL device with yttria-stabilized-zirconia filling the etched PC holes and as a top sandwiching dielectric layer to provide a dielectric mismatch of  $\sim 20$  for the photonic crystal structure in the ZnS:ErF<sub>3</sub> layer. The photonic crystal device had the honeycomb lattice structure with a lattice spacing of 748 nm, a hole depth of 648 nm and a hole diameter of 342 nm. This photonic crystal structure is expected from modeling to only affect 1550 nm light, not 550 nm. Since the ACTFEL devices emit 1550 nm and 550 nm light, comparison is made between these two wavelengths to characterize the enhancement to the 1550 nm light outcoupling. The photonic crystal structure exhibits an  $\sim 100\%$  increase in the ratio of 1550 nm light to 550 nm light when compared to the non-photonic crystal structure. The random structured device exhibits  $\sim 50\%$  increase in this ratio when compared to the non-photonic crystal device. Analysis of light scattering serves to explain the increase seen in the random structured device. Diffuse reflection analysis indicates similar responses from the three device types. Scattering and diffuse reflection do not serve to explain the enhanced outcoupling of 1550 nm light for the photonic crystal structured device. Therefore, it is due to the photonic band gap prohibiting 1550 nm light propagation in the plane of the ZnS:ErF<sub>3</sub> layer such that this light is transferred into modes of light propagation that outcouple from the device which is responsible for the enhanced 1550 nm emission of the photonic crystal device.

### **6.3 Future Work**

Optimization of the photonic crystal enhancement of the near-infrared emission should be possible by fine tuning of the fabricated device structure. Due to experimental difficulties complete overlap of the photonic crystal structure with the modeled photonic band gap was not achieved as seen in figure 4-7. Optimization of the photonic crystal effect would be expected

when the fabricated structure lies completely in the area of the full band gap region. This should be verified. This optimization correlates with the interest in determining the effects of variations in the hole diameter, spacing and depth of the PC structure. Detailed experimentation varying these parameters based on the guide of the photonic gap maps should result in the optimization of the enhancement of 1550 nm light output due to the PC effect in these devices. Ideally fabrication of devices of structures which lie on the gap map regions of no band gap, only TM band gap, only TE band gap, and both TM and TE band gap should be performed with the expectation of no enhancement from no gap and greatest enhancement from complete TM and TE gap overlapping regions.

One other area of future interest lies in the fact that across the top insulating layer and the top transparent conducting oxide layer of the device structure, light traversing these layers undergoes total internal reflection as well at the interfaces. By continuing the photonic crystal structure throughout these layers it is believed further enhancement can be achieved by the same mechanism as that of the enhancement achieved by the photonic crystal structure built into the emitting layer. Furthermore, the columns of dielectric material will influence the electrical properties of the device. Investigation into the full affects of the structuring onto the electrical properties and the subsequent influence on the emissions from the device requires further consideration.

## LIST OF REFERENCES

- [1] Y.A. Ono, "Materials for Full-Color Electroluminescent Displays" *Annu. Rev. Mater. Sci.* **27**, 283-303 (1997).
- [2] Y.A. Ono, *Electroluminescent Displays*, (World Scientific Publishing Co., 1995).
- [3] E. F. Schubert, N. E. J. Hunt, M. Micovic, R. J. Malik, D. L. Sivco, A.Y. Cho, and G. J. Zydzik, "Highly Efficient Light-Emitting Diodes with Microcavities," *Science* **265**, 943–945 (1994).
- [4] I. Schnitzer, E. Yablonovitch, C. Caneau, and T. J. Gmitter, "Ultrahigh Spontaneous Emission Quantum Efficiency, 99.7% Internally and 72% Externally, from AlGaAs/GaAs/AlGaAs Double Heterostructures," *Appl. Phys. Lett.* **62**, 131–133 (1993).
- [5] R. Windisch, C. Rومان, S. Meinschmidt, P. Kiesel, D. Zipperer, G. H. Dohler, B. Dutta, M. Kuijk, T. Borghs, and P. Heremans, "Impact of Texture-Enhanced Transmission on High-Efficiency Surface-Textured Light Emitting Diodes," *Appl. Phys. Lett.* **79**, 2315–2317 (2001).
- [6] M. R. Krames, M. Ochiai-Holcomb, G. E. Hofler, C. Carter-Coman, E. I. Chen, I. H. Tan, P. Grillot, N. F. Chui, J. W. Huang, S. A. Stockman, F. A. Kish and M. G. Craford, "High-Power Truncated-Inverted-Pyramid  $(\text{Al}_x\text{Ga}_{1-x})_{0.5}\text{In}_{0.5}\text{P}/\text{GaP}$  Light-Emitting Diodes Exhibiting >50% External Quantum Efficiency," *Appl. Phys. Lett.* **75**, 2365–2367 (1999).
- [7] J. Vücković, M. Loncar, and A. Scherer, "Surface Plasmon Enhanced Light-Emitting Diode," *IEEE J. Quantum Electron.* **36**, 1131–1143 (2000).
- [8] S. Fan, P. R. Villeneuve, J. D. Joannopoulos, and E. F. Schubert, "High Extraction Efficiency of Spontaneous Emission from Slabs of Photonic Crystals," *Phys. Rev. Lett.* **78**, 3294–3297 (1997).
- [9] B.E.A. Saleh and M.C. Teich, *Fundamentals of Photonics*, (New York: John Wiley and Sons Inc., 1991).
- [10] R. Sakai, T. Katsumata, S. Komuro and T. Morikawa, "Effect of Composition on the Phosphorescence from  $\text{BaAl}_2\text{O}_4: \text{Eu}^{2+}, \text{Dy}^{3+}$  Crystals," *J. Luminescence* **85**, 149-154 (1999).
- [11] D.J. Kim, H.M. Kim, M.G. Han, Y.T. Moon, S. Lee and S.J. Park, "Effects of KrF (248 nm) Excimer Laser Irradiation on Electrical and Optical Properties of GaN:Mg," *J. of Vac. Sci. & Tech. B* **21**, 641-645 (2003).
- [12] M.G. Tomilin, "Advanced Display Technologies," *J. Opt. Technol.* **70** (7), 454-464 (2003).

- [13] J.C. Hitt, J.P. Bender and J.F. Wager, "Thin-Film Electroluminescent Device Physics Modeling," *Critical Reviews in Solid State & Mat. Sci.* **25**, 29-85 (2000).
- [14] P.D. Rack and P.H. Holloway, "The Structure, Device Physics, and Materials Processing of Thin Film Electroluminescent Displays," *Material Science and Engineering Reports*, R21, 171-218 (1998).
- [15] B. Gudden and R.W. Pohl, "über Ausleuchtung der Phosphoreszenz durch Elektrische Felder," *Zeitschrift für Physik*, vol. 2, 192-196 (1929).
- [16] G.Destriau, *Journal de Chim. Phys. et Physico-Chimie Biol.* **33**, 620 (1936).
- [17] L. E. Tannas, *Flat-Panel Displays and CRT's* (New York: Van Nostrand Reinhold, 1985).
- [18] M. Yoshida, A. Mikami and T. Inoguchi, "Electroluminescent Materials," in *Phosphor Handbook*, S. Shionoya and W. Yen, eds (Taylor & Francis, Inc., 2006), pp. 581-600
- [19] A. Vecht, N.J. Werring and P.J.F. Smith, "High-efficiency D.C. Electroluminescence in ZnS (Mn, Cu)," *Brit. J. Appl. Phys. (J. Phys. D)* **1**, 134-136 (1968).
- [20] D. Kahng, "Electroluminescence of Rare-Earth and Transition Metal Molecules in II-VI Compounds via Impact Excitation," *Appl. Phys. Lett.* **13**, 210-212 (1968).
- [21] M.J. Russ and D.I. Kennedy, "The Effects of Double Insulating Layers on the Electroluminescence of Evaporated ZnS:Mn Films," *J. Electrochem. Soc.* **114**, 1066-1072 (1967).
- [22] T. Inoguchi, M. Takeda, Y. Kakihara, Y. Nakata and M. Yoshida: *SID Int. Symposium Digest (Soc. Inf. Display, Los Angeles, 1974)* p. 84.
- [23] S. Mito, C. Suzuki, Y. Kanatani and M. Ise: *1974 SID Int. Symposium Digest (Soc. Inf. Display, Los Angeles, 1974)* p. 86.
- [24] J. A. Castellano, *Handbook of Display Technology* (Harcourt Brace Jovanovich, 1992)
- [25] H. Uede, Y. Kanatani, H. Kishishita, A. Fujimori and K Okano, *SID Digest*, 1981: p. 28.
- [26] M. Takeda, Y. Kanatani, H. Kishishita, T. Inoguchi and K. Okano, *SID proceedings*, 1981. 57: p. 22.
- [27] C. N. King, "Electroluminescence: an industry perspective," *J. SID* **4**(3), 153-156 (1996).
- [28] M.K. Jayaraj and C.P.G. Vallabhan, "AC Thin Film Electroluminescent Devices with Rare Earth Doped ZnS," *J. Electrochem. Soc.* **138**(5), 1512-1516 (1991).

- [29] H. Kobayashi, S. Tanaka, V. Shanker, M. Shiiki, T. Kunou, J. Mita and H. Sasakura, "Multicolor Electroluminescent ZnS Thin Films Doped with Rare Earth Fluorides," *Physica Status Solidi A* **88**(2), 713-720 (1985).
- [30] R.E. Coovert, C.N. King, R.T. Tuenge, *SID Digest* (1982) 128.
- [31] W.A. Barrow, R.C. Coovert, E. Dickey, C.N. King, C. Laakso, S.S. Sun, R.T. Tuenge, *SID Digest* (1993) 76.
- [32] M. Leskelä, "Rare Earths in Electroluminescent and Field Emission Display Phosphors," *J. Alloys and Compounds* **275**, 702-708 (1998).
- [33] M. Shikada, *Telecommunications*, 26, 4 (1992).
- [34] S. O. Kasap, *Principles of Electronic Materials and Device* (McGraw-Hill, 2002).
- [35] M. Godlewski and M. Leskelä, "Excitation and Recombination Processes During Electroluminescence of Rare Earth-Activated Materials," *Crit. Rev. Solid State Mater. Sci.* 19(4), 199-239 (1994).
- [36] Glass Dynamics, LLC, "Alkali Free Borosilicate: Corning® 7059," <http://www.glassdynamicsllc.com/Alkali%20Free%20Borosilicate%207059.htm>
- [37] S. Ochiai, T. Kato, T. Ogawa, K. Kojima, Y. Uchida, A. Ohashi, M. Ieda and T. Mizutani, *Conf. on Elec. Ins. and Dielec. Phenom.*, 1994. p. 681.
- [38] Haaranen, J., R. Tornqvist, J. Koponen, T. Pitanen, M. Surma-aho, W. Barrow and C. Laakso, *SID 92 Digest*, 1992. 23: p. 348.
- [39] Khormanei, R., S. Thayer, K. Ping, G. Dolney, A. Ipri, F.L. Hsueh, R. Stewart, T. Keyser, G. Becker, D. Kagey and M. Spitzer, *SID 94 Digest*, 1994. 25: p. 137.
- [40] Wu, X., *EL* **96**, 285 (1996).
- [41] D. Moorehead, "Optical and Electrical Characterization of Alternating Current Thin Film Electroluminescent Displays," M.S. thesis, 2000, University of Florida: Gainesville.
- [42] J. F. Wager, J. C. Hitt, B. A. Baukol, J. P. Bender, and D. A. Keszler, "Thin Film Electroluminescent Phosphor Luminescent Impurity Doping Trends." 11th International Workshop on Inorganic and Organic Electroluminescence, Ghent, Belgium, September 23-26, 2002.
- [43] J.I. Pankove, *Electroluminescence*. Topics in Applied Physics Vol. 17 (Springer-Verlag, Berlin, 1977).
- [44] II-VI Incorporated Optics Catalog, July 1998 Revision, p. 6 and at [www.ii-vi.com](http://www.ii-vi.com).

- [45] R. Mach and G.O. Mueller, "Efficiency and Saturation in A.C. Thin Film EL Structures," *Physica Status Solidi A: Applied Research* **81**(2), 609-623 (1984).
- [46] D. M. DeVito, "Electroluminescence from Zinc Sulfide Thin Films Doped with Erbium Trifluoride." Ph.D. dissertation, 2006, University of Florida: Gainesville.
- [47] A. Kale, "Alternating Current Thin Film Electroluminescence in the Near Infrared from Zinc Sulfide Doped with Rare Earths." Ph.D. dissertation, 2003, University of Florida: Gainesville.
- [48] Stevens, H. 2000, Dow Corning, Inc.
- [49] P.D. Keir, "Fabrication and Characterization of ACTFEL devices," M.S. thesis, 1999, Oregon State University: Corvallis.
- [50] Präzisions Glas & Optik, "Precision Optics, thin film coatings, technical class," <http://www.pgo-online.com>, retrieved January 2006.
- [51] A. Kale, N. Shepherd, W. Glass, D. DeVito, M. Davidson and P.H. Holloway, "Infrared Emission from Zinc Sulfide: Rare Earth Doped Thin Films," *J. Appl. Phys.* **94**, 3147-3152 (2003).
- [52] P.M. Alt, *SID Digest*, 1984 p. 79.
- [53] Y. Ono, *Encyclopedia of Applied Physics* (New York: VCH publishers, 1993).
- [54] Ono. Y., *SID Seminar lecture notes*, Volume II, F-1, F-1/1, 1993.
- [55] Y. Ono, *Progress in Information Display Technology*, ed. S. Kobayashi. Vol. 1. (Singapore: World Scientific Publishing Co, 1995).
- [56] Howard, W.E., *IEEE Transactions on Electron Devices*, 1977. ED-24: p.903.
- [57] Tiku, S.K. and G.C. Smith, *IEEE Transactions on Electron Devices*, 1984. ED-31: p.105.
- [58] W.D. Callister, *Materials Science and Engineering, An Introduction* (New York: John Wiley and Sons, Inc., 1997)
- [59] P.D. Keir, H. Le, R.L. Thuemler, H. Hitt and J.F. Wager, "Relaxation Charge Anomalies in the Charge-Voltage Characteristics of Alternating-Current Thin-Film Electroluminescent Devices," *Appl. Phys. Lett.* **69**(16), 2421-2423 (1996).
- [60] Fujita, Y., Kuwata, J., Nishikawa, M., Tohda, T., Matuoka, T., Abe, A., and Nitta, T., *Proc. Soc. Inf. Disp.*, 25, 177, 1984

- [61] H. Kim, C.M. Gilmore, A. Piqué, J.S. Horwitz, H. Mattoussi, H. Murata, Z.H. Kafafi, and D.B. Chrisey, “Electrical, Optical, and Structural Properties of Indium–Tin–Oxide Thin Films for Organic Light-Emitting Devices,” *J. Appl. Phys.* **86**(11), 6451-6461 (1999).
- [62] S. Honda, A. Tsujimoto, M. Watamori and K. Oura, “Oxygen Content of Indium Tin Oxide Films Fabricated by Reactive Sputtering,” *J. Vac. Sci. Tech. A* **13**(3), 1100-1103 (1995).
- [63] Suzuki, M., Y. Maeda, M. Muraoka, S. Higuchi and Y. Sawada, “ITO Films Sputter-Deposited Using an ITO Target Sintered with Vanadium Oxide Additive,” *Mater. Sci. Eng. B* **54**, 43-45 (1998).
- [64] Q. X. Jia, J. P. Zheng, H. S. Kwok, W. A. Anderson, “Indium Tin Oxide on InP by Pulsed Laser Deposition,” *Thin Solid Films* **258**, 260-263 (1995).
- [65] M. Kamei, Y. Shigesato, I. Yasui, N. Taga and S. Takaki, “Comparative Study of Heteroepitaxial and Polycrystalline Tin-doped Indium Oxide Films,” *J. Non-Crystalline Solids* **218**, 267-272 (1997).
- [66] S. Laux, N. Kaiser, A. Zoller, R. Gotzelmann, H. Lauth and H. Bernitzki, “Room Temperature Deposition of Indium Tin Oxide Thin Films with Plasma Ion-Assisted Evaporation,” *Thin Solid Films* **335**, 1-5 (1998).
- [67] K. Tominaga, T. Ueda, T. Ao, M. Kataoka and I. Mori, “ITO Films Prepared by Facing Target Sputtering System,” *Thin Solid Films* **281-282**, 194-197 (1996).
- [68] K. Utsumi, O. Matsunaga and T. Takahata, “Low Resistivity ITO Film Prepared Using the Ultra High Density ITO Target,” *Thin Solid Films* **334**, 30-34 (1998).
- [69] F. Aduodija, H. Izumi, T. Ishihara and H. Yoshioka, “High-Quality Indium Oxide Films at Low Substrate Temperature,” *Appl. Phys. Lett.* **74**(20), 3059-3061 (1999).
- [70] D.C. Paine, T. Whitson, D. Janiac, R. Beresford and C. Ow Yang, “A study of Low Temperature Crystallization of Amorphous Thin Film Indium–Tin–Oxide,” *J. Appl. Phys.* **85**(12), 8445-8450 (1999).
- [71] K.L. Chopra, S. Major and D.K. Pandya, “Transparent Conductors—A Status Review,” *Thin Solid Films* **102**, 1-46 (1983).
- [72] Kobayashi, H., and S. Tanaka, *J. SID*, 1996. 4(3): p. 157-163
- [73] Mauch, R.H., *J. SID*, 1997. 5(3): p. 173-178.
- [74] Rack. P.D., A. Namen, P.H. Holloway, S-S. Sun and R.T. Tuenge, *MRS Bulletin*, 1996. 21: p. 49.

- [75] S. Nakamura, Y. Yamada and T. Taguchi, "Room-Temperature 340 nm Ultraviolet Electroluminescence from ZnS-Based Light-Emitting Diodes," *J. Cryst. Growth* **214**, 1091-1095 (2000).
- [76] P.J. Dean, D.C. Herbert, Excitons, in K. Cho (Ed.), Springer-Verlag, Berlin-Heidelberg, 1979, pp.138.
- [77] Blasse, G. and B.C. Grabmaier, *Luminescent materials* (Springer-Verlag, 1994).
- [78] J.A. Duffy, Bonding, Energy Levels and Bands in Inorganic Solids, Wiley, New York, 1990, pp.40
- [79] A. N. Georgobiani, A.N. Gruzintsev, C. Barthou, P. Benalloul, J. Benoit, B.G. Tagiev, O.B. Tagiev and R.D. Zhabborov, "Infrared Luminescence of Er<sup>3+</sup> in Calcium Thiogallate," *Journal of the Electrochemical Society* **148**(11), H167-H170 (2001).
- [80] D. H. Smith, "Modeling A.C. Thin-Film Electroluminescent Devices," *J. Luminescence* **23**, 209-235 (1981).
- [81] T. A. Oberacker and H.W. Schock, "Investigations of the Influence of Halides on the Properties of CeX<sub>3</sub>-doped (X = Cl, F) Strontium Sulfide Thin Film Electroluminescence Devices," *J. of Cryst. Growth* **159**, 935-938 (1996).
- [82] C.T. Hsu, Y.J. Lin, Y.K. Su and M. Yokoyama, "Effects of Insulating Layers and Active Layer on ZnS:Tb, F Thin-Film Electroluminescent Devices," *Jpn. J. Appl. Phys.* **32**, 1983-1986 (1993).
- [83] W. Glass, A. Kale, N. Shepherd, M. Davidson, D. DeVito, and P. Holloway, "Sputter Deposited Electroluminescent Zinc Sulfide Thin Films Doped with Rare Earths," *J. Vac. Sci. Technol. A* **25**, 492 (2007).
- [84] G.N.v.d. Hoven, E. Snoeks, A. Polman, C. van Dam, J.W.M. van Uffelen and M.K. Smith, "Upconversion in Er-implanted Al<sub>2</sub>O<sub>3</sub> Waveguides," *Journal of Applied Physics* **79**(3), 1258-1266 (1995).
- [85] Lord Rayleigh, "On the dynamical theory of gratings," *Proceedings of the Royal Society of London: Series A* **79**(532), 399-416 (1907).
- [86] Johnson, S.G.; Joannopoulos, J. D. "Introduction to Photonic Crystals: Bloch's Theorem, Band Diagrams, and Gaps (But No Defects)" MIT MRS Chapter, 2003 IAP tutorial series.
- [87] J. D. Joannopoulos, R. D. Meade, J. N. Winn, *Photonic Crystals: Molding the Flow of Light* (Princeton University Press, 1995).

- [88] Steven G. Johnson and J. D. Joannopoulos, "Block-iterative frequency-domain methods for Maxwell's equations in a planewave basis," *Optics Express* **8**, no. 3, 173-190 (2001), <http://www.opticsexpress.org/abstract.cfm?URI=OPEX-8-3-173>.
- [89] M. Allen, "Gap Maps for Photonic Crystals", August 2003, Helsinki University of Technology/Electromagnetics Lab. Report Series, Report 412, 25p.
- [90] Jean-Michel Lourtioz, *Photonic Crystals: Towards Nanoscale Photonic Devices* (Springer-Verlag Berlin Heidelberg, 2005).
- [91] S. Ogawa, M. Imada, S. Yoshimoto, M. Okano and S. Noda, "Control of Light Emission by 3D Photonic Crystals," *Science* **305**, 227-229 (2004).
- [92] E. Yablonovitch, "Inhibited Spontaneous Emission in Solid-State Physics and Electronics," *Phys. Rev. Lett.* **58**(20), 2059-2062 (1987).
- [93] M. Fujita, S. Takahashi, Y. Tanaka, T. Asano and S. Noda, "Simultaneous Inhibition and Redistribution of Spontaneous Light Emission in Photonic Crystals," *Science* **308**, 1296-1298 (2005).
- [94] X.D. Liu, Y.Q. Wang, B.Y. Cheng and D.Z. Zhang, "Conservative Form of the Density of States of a Photonic Crystal with a Pseudogap," *Physical Review E* **68**(3), 036610 (2003).
- [95] S. Noda and M. Fujita, "Light-emitting diodes: Photonic crystal efficiency boost," *Nature Photonics* **3**(3), 129-130 (2009).
- [96] S. He Guang, H.Y. Qin and Q. Zheng, "Rayleigh, Mie, and Tyndall Scatterings of Polystyrene Microspheres in Water: Wavelength, Size, and Angle Dependences," *Journal of Applied Physics* **105**, 023110 (2009).
- [97] Y. Yonghong, Z. Jiayu, G. Peifu and T. Jinfa, "Study on Optical Efficiency of Alternating-Current Thin-Film Electroluminescent Devices," *Thin Solid Films* **315**(2), 251-256 (1991).
- [98] Lawrence B. Wolff, "Relative Brightness of Specular and Diffuse Reflectance," *Optical Engineering* **33**(1), 285-293 (January 1994).
- [99] L. Rayleigh, *Philos. Mag.* **41**, 107 1871; **41**, 447 1971.
- [100] I. Zailer, J. E. F. Frost, V. Chabasseur-Molyneux, C. J. B. Ford and M. Pepper, "Crosslinked PMMA as a High-Resolution Negative Resist for Electron Beam Lithography and Applications for Physics of Low-Dimensional Structures," *Semicond. Sci. Technol.* **11**, 1235-1238 (1996).

- [101] Stephen A. Campbell, *The Science and Engineering of Microelectronic Fabrication* (Oxford University Press, 1996).
- [102] J.I. Goldstein, D.E. Newbury, P. Echlin, D.C. Joy, C. Fiori, E. Lifshin, *Scanning Electron Microscopy and X-ray Microanalysis* (Plenum Press, 1981).
- [103] Peter W. Hawkes, *Microscopy, Spectroscopy, Holography and Crystallography with Electrons* Vol. 123. (Academic Press, 2002).
- [104] A. N. Broers, W. W. Molzen, J. J. Cuomo and N. D. Wittels, "Electron Beam Fabrication of 80Å Metal Structures," *Appl. Phys. Lett.* **29**, 596-598 (1976).
- [105] A. Gonzales, "Recent Results in the Application of Electron Beam Direct Write Lithography," *Electron-Beam, X-ray, and Ion-Beam Submicrometer Lithographies*, p.374 (1989).
- [106] K.A. Valiev, A.N. Kirillov, B.N. Kovtun, T.M. Makhviladze and M.M. Mkrtchyan. "Simulation of Latent Image Formation in Electron Lithography." *Proceedings of the Institute of General Physics Academy of the Sciences of the USSR. Vol 8. Lithography in Microelectronics.* Nova Science Publishers. 1989.
- [107] MicroChem Corporation, "PMMA data sheet," <http://www.microchem.com>.
- [108] Henry I. Smith. *A Review of Submicron Lithography. Superlattices and Microstructures*, Vol. 2, No 2, 1986
- [109] W. Kern, "Chemical Etching of Dielectrics," in *Etching for Pattern Definition*, Electrochem. Soc., Princeton, NJ, 1976.
- [110] S. M. Hu and D. R. Kerf, "Observation of Etching of n-type Silicon in Aqueous HF Solutions," *J. Electrochem. Soc.* **114**, 414 (1967).
- [111] Milton Ohring, *Materials Science of Thin Films: Deposition and Structure* (Academic Press, 2002).
- [112] S. J. Pearton, "Wet and Dry Etching of Compound Semiconductors," *Handbook of Compound Semiconductors*, Noyes Publications, 1995.
- [113] J. W. Lee, B. Pathangey, M. R. Davidson, P. H. Holloway, E. S. Lambers, A. Davydov, T. J. Anderson and S. J. Pearton, "Electron Cyclotron Resonance Plasma Etching of Oxides and SrS and ZnS-Based Electroluminescent Materials for Flat Panel Displays," *J. Vac. Sci. Technol. A* **16**(3), 1944-1948 (May/June 1998).
- [114] G. S. Oehrlein, "Dry Etching Damage of Silicon: A Review," *Mat. Sci. Eng. B* **4**, 441 (1989).

- [115] Ross McCluney, *Introduction to Radiometry and Photometry*, (Boston: Artech House, 1994).
- [116] G. Härkönen, M. Leppänen, E. Soininen, R. Törnqvist and J. Viljanen, "Multicolour Thin Film Electroluminescent Displays: a New Application of Rare Earth Metals," *Journal of Alloys and Compounds*, **225**(1-2), 552-554 (1995).
- [117] K. Bhattacharyya, S.M. Goodnick and J.F. Wager, "Monte Carlo Simulation of Electron Transport in Alternating-Current Thin-Film Electroluminescent Devices," *J. Appl. Phys.* **73**(7), 3390-3395 (1993).
- [118] Y.A. Ono, H. Kawakami, M. Fuyama and K. Onisawa, "Transferred Charge in the Active Layer and EL Device Characteristics of TFEL Cells," *Jpn. J. Appl. Phys* **26**(1), 1482-1492 (1987).
- [119] M. Leskelä and M. Ritala, "Atomic Layer Deposition (ALD): from Precursors to Thin Film Structures," *Thin Solid Films* **409**, 138–146 (2002).
- [120] Veeco Corporation, "Veeco Probe Tip," [https://www.veecoprobes.com/probe\\_detail.asp?ClassID=100](https://www.veecoprobes.com/probe_detail.asp?ClassID=100).
- [121] Newbury, D.E., D.C. Joy, P. Cechlin, C. Fiori and J.I. Goldstein, *Advanced Scanning Electron Microscopy and X-ray Microanalysis*, 1986, New York: Plenum Press.
- [122] A. Benninghoven, *Secondary ion mass spectrometry: basic concepts, instrumental aspects, applications, and trends* (J. Wiley, 1987).
- [123] Brundle, C.R., J.C.A. Evans and S. Wilson, *Encyclopedia of Materials Characterization*, Materials Characterization Series, ed. J.C.A. Evans, 1992, Boston: Butterworth-Heinemann.
- [124] T. I. Karu, L. V. Pyatibrat, S. F. Kolyakov and N. I. Afanasyeva, "Absorption Measurements of a Cell Monolayer Relevant to Phototherapy: Reduction of Cytochrome *c* Oxidase under near IR Radiation," *Journal of Photochemistry and Photobiology B: Biology* **81**(2), 98-106 (2005).
- [125] "Holloway, Paul H. (Gainesville, FL, US), McGuire, Gary (Chapel Hill, NC, US), Shenderova, Olga A. (Raleigh, NC, US), Reynolds, John (Gainesville, FL, US), Schanze, Kirk S. (Gainesville, FL, US), Boncella, James (Los Alamos, NM, US)", "Phototherapy bandage", patent: 7304201, December 2007.
- [126] K.L. Chopra, S. Major and D.K. Pandya, "Transparent Conductors—A Status Review," *Thin Solid Films* **102**, 1-46 (1983).
- [127] Khadijeh Bayat, Sujeet K. Chaudhuri and Saffiedin Safavi-naeini, "Polarization and Thickness Dependent Guiding in the Photonic Crystal Slab Waveguide," *Optics Express* **15**(13), (2007).

- [128] I. Schnitzer, E. Yablonovitch, C. Caneau, T.J. Gmitter, A. Scherer, “30% External Quantum Efficiency from Surface Textured, Thin-Film Light-Emitting Diodes,” *Appl. Phys. Lett.* **63**(16), 2174-2176 1993.
- [129] Scott Prahl, “Mie Scattering Calculator,” [http://omlc.ogi.edu/calc/mie\\_calc.html](http://omlc.ogi.edu/calc/mie_calc.html).
- [130] N. M. Bradman, “Design and Fabrication of Diffractive Lenses for Visible and Near Infrared Wavelengths.” Ph.D. dissertation, 2007, University of Florida: Gainesville.

## BIOGRAPHICAL SKETCH

Evan Stanley Law was born in Arcadia, California to Reed Gwillim Law Jr. and Janice Black Law on November 6, 1979. He lived in California until 1988 when he moved to Chapel Hill, North Carolina where he graduated from East Chapel Hill High School in 1998. He attended Asbury College from 1998 until 2001 when he transferred to North Carolina State University where he graduated in 2003 with a Bachelor of Science degree in Materials Science and Engineering. While an undergrad he worked as an X-ray Photoelectron Spectroscopy operator at the Analytical Instrumentation Facility at NCSU. He was admitted for graduate studies to the University of Florida Department of Materials Science and Engineering in August 2004 under the direction of Dr. Paul Holloway. In Dr. Holloway's research group he worked on the development of incorporating a photonic crystal structure for near-infrared enhancement into alternating current thin film electroluminescent devices. While at the University of Florida he was involved with Chi Alpha Christian Fellowship to which he is most endeared. He was active in intramural activities participating in basketball, tennis, flag football and softball achieving many victories. He received his Ph.D. from the Department of Materials Science and Engineering at the University of Florida under the advisement of Dr. Paul H. Holloway in August 2009.